HIGH-RESOLUTION INFRARED SPECTROSCOPY IN PURSUIT OF C_{60} AND OTHER ASTROCHEMICAL TARGETS

BY

BRADLEY MICHAEL GIBSON

DISSERTATION

Submitted in partial fulfillment of the requirements
for the degree of Doctor of Philosophy in Chemistry
in the Graduate College of the
University of Illinois at Urbana-Champaign, 2015

Urbana, Illinois

Doctoral Committee:

Professor Benjamin J. McCall, Chair
Professor Alexander Scheeline
Professor J. Gary Eden
Assistant Professor Josh Vura-Weis

Abstract

This work is primarily concerned with the development of a mid-infrared cavity ringdown spectrometer with the intent of observing rotationally-resolved vibrational spectra of C_{60} and other astronomically relevant molecules, including the polyoxymethylene 1,3,5-trioxane. C_{60} was first discovered during experiments intended to simulate the conditions found in carbon stars, and has since been observed via emission spectroscopy in several planetary nebulae as well as the inerstellar medium. Due to its low ionization potential, much of the C_{60} in interstellar space is expected to be ionized to C_{60}^{+}, which has long been suspected as one of the carriers of the diffuse interstellar bands; recent work supports this assignment, further increasing interest in the astrochemistry of C_{60}. While these observations through emission spectroscopy have had a significant impact, emission spectroscopy is not an effective approach in cold regions of space with low ultraviolet flux - as such, obtaining a high-resolution absorption spectrum remains an important goal.

This is an extension of previous development work and attempts to observe the spectrum of C_{60} - as the principle shortfall of those previous attempts was the the inability to vibrationally cool C_{60} produced via thermal vaporization, much of this following will focus on the development and validation of an alternative vaporization method involving the expansion of supercritical fluids containing the target molecules. This should allow vapor to be produced at much lower temperatures, allowing more C_{60} to reach the ground state in spite of inefficient supersonic cooling. The first generation source has been constructed and tested, with the results informing the design of a second-generation source that has been constructed and is currently being evaluated.

In addition to the development of an improved source for cold C_{60}, we have also implemented a new external-cavity quantum cascade laser as the light source in our instrument. This new laser has significantly improved spectral coverage when compared to the previous light source, in addition to considerably easier and more reliable frequency tuning. However, the addition of a vibration-sensitive grating as a wavelength selective element introduced an unacceptable jitter in the lasing frequency. To address this, we developed a novel laser locking system based on side-of-fringe locking to a solid germanium etalon; in order to maintain continuous wavelength tuning, the free spectral range of the etalon is tuned by stepping its angle with respect

to the incident laser. This has allowed us to stabilize the laser to acceptable levels while maintaining the ability to tune its lasing frequency very precisely.

Finally, we recorded, simulated, and assigned the rotationally-resolved absorption spectrum of the ν_{16} vibrational band of 1,3,5-trioxane. In addition to the importance of trioxane to understanding formaldehyde chemistry in comets, trioxane was chosen as a means of testing the various improvements made to the spectrometer. The spectrum described in this work was obtained using the new external-cavity quantum cascade laser and locking system; efforts to evaluate the second-generation supercritical fluid expansion source will use trioxane spectroscopy to estimate the efficiency of rotational and vibrational cooling.

Acknowledgments

First, I would like to thank my fellow researchers in the McCall Group for their help and support throughout my time in Urbana. In particular, Brian Brumfield and Jacob Stewart served as mentors during my early years and were responsible for much of the instrument development and spectroscopy that this work is built on. I would also like to thank Nicole Koeppen, who joined me in working on this experiment and provided invaluable help in keeping everything running, as well as contributing to data collection and assignment in the trioxane work and the assembly and characterization of the second-generation supercritical fluid source. Peter Kiamanesh was likewise very helpful in building the first-generation source and keeping everything working while I worked on the programming and electronics behind the locking system.

I would also like to thank Claire Gmachl and Gerard Wysocki for their generosity in providing the quantum cascade laser gain chips used in this work, as well as their help with laser design. I am pleased to say that we haven't had a single chip fail during my graduate studies, which is both rather amazing and greatly appreciated.

Next, I wish to extend my thanks to my committee members, Alexander Scheeline, Gary Eden and Josh Vura-Weis for their time and support. I am particularly thankful to Dr. Scheeline for everything I learned during his spectroscopy course, which has been sorely missed since his retirement from the university.

Finally, and perhaps most importantly, I wish to thank my advisor, Ben McCall. He has been an outstanding scientific mentor, as well as an excellent person to work for. I really couldn't be happier with the next step in my career, and there is no one else who has done so much in getting me there.

Table of Contents

List of Tables

List of Figures

Chapter 1

Introduction

1.1 C_{60}: Discovery and Astronomical Relevance

C_{60}, also known as buckminsterfullerene, was first discovered in 1985 by Kroto and coworkers [1] during experiments intended to replicate the conditions present in carbon star outflows. Briefly, a carbon plasma was generated using a pulsed laser and rapidly cooled in a helium carrier gas. The resulting product mixture was then photoionized and analyzed via time-of-flight mass spectrometry. Among other complex carbonaceous products, a series of large, even-numbered carbon clusters were observed, with the most abundant of these corresponding to C_{60} and C_{70}. It was suggested that the C_{60} cluster might have an icosahedral structure, similar to designs of the architect Buckminster Fuller - this structure was later confirmed by X-ray crystallography [2], becoming the first member of the class of molecules now referred to as fullerenes.

Because the Kroto experiments were successful in producing many carbonaceous compounds that had already been observed in the circumstellar regions of carbon stars [1], it appeared reasonable that C_{60} and other fullerenes might be present in similar astronomical environments. Furthermore, C_{60} is a remarkably stable structure with regards to photoionization, and as such it seemed likely that it might also be incorporated into dense and diffuse clouds in the interstellar medium [3]. Searches for astronomical C_{60} were initially limited by the lack of efficient terrestrial synthesis techniques and laboratory spectra, but work by Kratchsmer and coworkers [2, 4] provided both an effective electric arc synthesis method and laboratory spectra in the ultraviolet-visible and infrared regions.

Despite the availability of laboratory spectra, C_{60} evaded astronomical detection until 2010, when Cami and coworkers [5] observed features attributed to three vibrational modes of C_{60} in the emission spectrum of the planetary nebula Tc1; additional features were observed that could be attributed to C_{70}, as shown in Fig. 1. Tc1 was believed to be a hydrogen-poor region, supporting earlier assumptions that fullerenes would form primarily where a lack of hydrogen made the formation of polycyclic aromatic hydrocarbons less favorable. Shortly after the detection by Cami, however, additional detections were made by Garcia-Hernandez and coworkers that indicated the presence of C_{60} in four additional planetary nebulae which were

not considered hydrogen-poor [6]. In addition to these detections in planetary nebulae, which are believed to be from solid-phase C_{60} on dust grains, emission features attributed to UV-excited C_{60} have been observed in reflection nebulae, confirming the presence of C_{60} in the interstellar medium [7].

In addition to being of interest in describing the chemistry of carbon stars, C_{60} is also notable as a potential carrier for the diffuse interstellar bands (DIBs). These bands constitute a collection of absorption features in the interstellar medium spanning the ultraviolet, visible, and near-infrared spectral regions which have not yet been attributed to any known molecular carriers, and remain one of the greatest unsolved mysteries in interstellar chemistry [8]. Although neutral C_{60} does not correspond to any of the DIB features, its low ionization potential suggests that most interstellar C_{60} should be ionized to C_{60}^+, which could explain some observed DIB absorptions [9]. Recent work has provided even stronger evidence for the attribution of some DIB features to C_{60}^+ [10].

Although the existing laboratory and astronomical work centered on C_{60} is extensive and includes a number of astounding accomplishments, laboratory absorption spectroscopy of gaseous C_{60} remains an unsolved challenge. Existing emission spectra allow astronomical searches in many environments, but do not allow for detections in regions where C_{60} cannot be adequately excited - notably, cold environments with low UV flux. Additionally, quantification of C_{60} via emission spectroscopy relies upon accurate values for UV flux and the UV absorption cross-section of C_{60}, making absorption spectroscopy preferable in many cases. Because absorption spectroscopy would be such a powerful complement to existing emission work, our group has committed significant time and resources to the acquisition of a laboratory spectrum - although efforts are ongoing, the significant challenges posed by C_{60} as a spectroscopic target have thus far prevented the acquisition of a rotationally-resolved infrared absorption spectrum.

1.2 C_{60}: Spectroscopic Challenges and Early Laboratory Work

The principle challenge for gas-phase absorption spectroscopy of C_{60} is its very low volatility. The traditional approach to producing vibrationally-cold vapor of non-volatile molecules is to simply heat the condensed sample until it has significant vapor pressure, then use a supersonic expansion to cool the resulting gas enough to produce a significant population in the vibrational ground state. In the case of C_{60}, this requires that the solid sample be heated to temperatures of approximately 950 K (see Fig. 2). Although designing an oven and supersonic expansion to operate at such temperatures presented a number of challenges, this is the approach initially attempted by our group. The approach used was validated with a number of intermediate molecules, including methylene bromide and pyrene [11, 12], but ultimately proved to be unsuccessful in

producing an infrared absorption spectrum [13].

Based on the amount of C_{60} vapor produced and the sensitivity of our spectrometer, as determined by the earlier pyrene work, the strongest features of the C_{60} absorption spectrum should have been observed at signal-to-noise ratios in excess of 100. That no such features were observed appears to be the result of inefficient cooling of C_{60} in our supersonic expansion. Effective vibrational cooling in a supersonic expansion depends upon the transfer of vibrational energy from the target molecule to the carrier gas through collisions, and is most effective when an abundance of vibrational states allows the target molecule to go from its initial excited state to the ground state in a number of small steps. In cases where few vibrational states are available, the cooling process can become bottlenecked and produce a non-thermal distribution of vibrational states that leaves the ground state less populated than would otherwise be expected. This is likely the case for C_{60} - there are few vibrational states available below 500 K, as shown in Fig. 3, making vibrational cooling below this temperature far more difficult. The problem is exacerbated by C_{60}'s size - the many available vibrational degrees of freedom lead to a partition function that grows very rapidly with increasing temperature, as shown in Fig. 4. At a vibrational temperature of 300 K, Q_{vib} is already over 2,000.

Because of the difficulty of cooling C_{60} from the temperatures required for traditional thermal vaporization, it seems clear that an alternative vaporization technique with lower operating temperatures will be necessary to obtain an infrared absorption spectrum. The bulk of this work is focused on the development and validation of such a technique, as well as other instrumental improvements intended to address its shortcomings.

1.3 Instrumental Improvements: Locking and Supercritical Fluid Expansion Source

We are aware of three possible approaches to producing lower-temperature C_{60} vapor. The first of these is is laser desorption followed by supersonic expansion. This technique has been successfully employed in resonant two-photon ionization experiments involving C_{60} [14, 15], but the vibrational temperature of the vapor produced was not directly measured and cannot be readily calculated using available data - the temperature of laser-desorbed molecules vary depending upon the target molecule, substrate, and laser used. The second option considered was a gas-phase aggregation cluster source [16]; in this technique, C_{60} would be entrained in a flow of noble gas and cooled via collisions with the walls of the source, which would be cryogenically cooled. Again, this type of source has been used successfully in resonant two-photon ionization spectroscopy of C_{60}; the primary disadvantage would be cost and a significant increase in experimental

complexity.

The third option, which was ultimately chosen for the next iteration of our C_{60} experiment, is supercritical fluid expansion. In this technique, C_{60} is dissolved in a supercritical fluid composed of CO_2 and a co-solvent, which is depressurized through a pinhole before being entrained in a secondary expansion of argon. This type of molecular source has been demonstrated by Goates and coworkers [17]; the temperatures achieved depend largely upon the solvent system chosen, as this determines the temperature required to pass the critical point. For C_{60}, it has been shown that a 7:3 mixture of CO_2:toluene is effective for supercritical fluid extractions [18, 19], which would have a critical temperature of approximately 450 K. This represents a vast improvement over the previous high temperature oven source in terms of initial vibrational temperature, but is also expected to produce number densities approximately two orders of magnitude lower. This will likely require additional improvements to our spectrometer to increase its sensitivity, but nonetheless seems to provide a feasible path towards a ro-vibrational absorption spectrum of C_{60}.

We have successfully built a first-generation supercritical fluid source and integrated it into our existing spectrometer for evaluation. Testing with D_2O showed promising cooling performance, but a number of performance issues with this first iteration were identified - most importantly, the heating system used was unable to reach the necessary temperature for our desired solvent system. In response, we have designed an improved second-generation source to address these shortcomings. This new source has been constructed and integrated into our spectrometer, and evaluation is currently ongoing.

In addition to the integration of a new molecule source, we have made significant improvements to the light source of our spectrometer. Earlier work used a Fabry-Pérot quantum cascade laser provided by the Gmachl research group at Princeton. The laser performed well, but had limited tuning range and numerous coverage gaps, as shown in Fig. 5; additionally, attempting to tune the laser to specific wavelengths within its range could be quite challenging. Because of this, we have integrated a new external-cavity quantum cascade laser, seen in Fig. 6, based on designs from Gerard Wysocki and using a gain chip provided by his lab at Princeton. The tuning ranges are compared in Fig. 5; notably, the tuning range for the new external cavity laser is completely continuous and any desired wavelength can be reliably and easily selected due to the addition of external cavity grating angle as a wavelength selective element. Additionally, the new laser is cooled thermoelectrically rather than cryogenically, making it considerably more convenient to maintain.

Although the new external-cavity quantum cascade laser is superior in terms of tuning range and ease of operation, we initially had some significant difficulties with stability of the lasing frequency. While nominally set at a single wavelength, the frequency, as measured by wavemeter, could vary by over 300 MHz over timeframes of a few seconds, as seen in Fig. 7. Such severe frequency jitter would not allow

us the resolution needed to clearly resolve rotational lines for many of the molecules we were interested in studying. As we considered it likely that mechanical vibrations being coupled into the external cavity grating angle were responsible for the instability, we attempted a number of passive approaches for improving the mechanical stability of the laser - the optical table was placed on vibration isolation legs, a pulse-damping reservoir was added to the laser's chilled water circulator, and the vacuum chamber was isolated from the optical table by using a hollow silica waveguide to couple light into the optical cavity. These approaches did improve the stability of the laser, but ultimately it proved necessary to include active frequency locking.

This was accomplished by developing a new locking technique: tilt-tuned side-of-fringe etalon locking. Essentially, the laser is side-of-fringe locked to a solid germanium etalon, with continuous frequency tuning accomplished by changing the angle of the etalon relative to the incoming laser beam. This approach allows for extremely fine control of the center frequency of the laser as well as vastly reduced frequency jitter - the implementation of this system allowed us to reduce the standard deviation of our lasing frequency from over 130 MHz to approximately 1 MHz over a one-second integration time. Although further improvements could have been made to the frequency stability of the laser, this proved to be sufficient for the target molecules this work is concerned with.

1.4 1,3,5-Trioxane: Astronomical Relevance and Instrument Validation

Following the improvements to our spectrometer, we sought to validate its performance using a target of intermediate difficulty before moving on to our work with C_{60}. Ultimately, we chose 1,3,5-trioxane for this work. Trioxane is convenient from a spectroscopic standpoint - it is a readily available commodity chemical and a very strong absorber, which are important considerations if we are to use it in the evaluation of our supercritical fluid expansion source. Although sensitivity improvements for the spectrometer are planned before the next attempt to observe C_{60}, these have not yet been implemented, and a strong absorber like trioxane will be necessary to evaluate the source since it produces relatively low number densities.

In addition to its convenience for instrument validation, trioxane is astronomically important in its own right. Trioxane is one of the simplest members of the polyoxymethylene (POM) class of molecules, which have been proposed as the source of extended formaldehyde production in cometary comae [20, 21], making them important molecules in studies of prebiotic chemistry. Trioxane is of particular interest since it is a photodegradation product of larger POM molecules, potentially making it disproportionately abundant in comae. Although trioxane and other POMs have been present in laboratory simulations of cometary

conditions for some time [20], they have not yet been detected with certainty. Recent mass spectrometry results from the Rosetta mission strongly suggest the presence of POM [22], data collection and analysis are ongoing.

For the purposes of this work, we have successfully recorded, simulated and assigned the ro-vibrational spectrum of the ν_{17} band of 1,3,5-trioxane. Although numerous microwave spectra [23, 24, 25, 26, 27, 28] and the ro-vibrational spectrum of the ν_{16} band [29] have been observed, this work is the first rotationally-resolved observation of the ν_{17} band. Going forward, our intention is to repeat these observations using the second-generation supercritical fluid source in order to estimate the efficiency of rotational and vibrational cooling; this will allow us to evaluate the feasibility of C_{60} spectroscopy using this approach prior to making any necessary changes to improve our spectrometer's sensitivity.

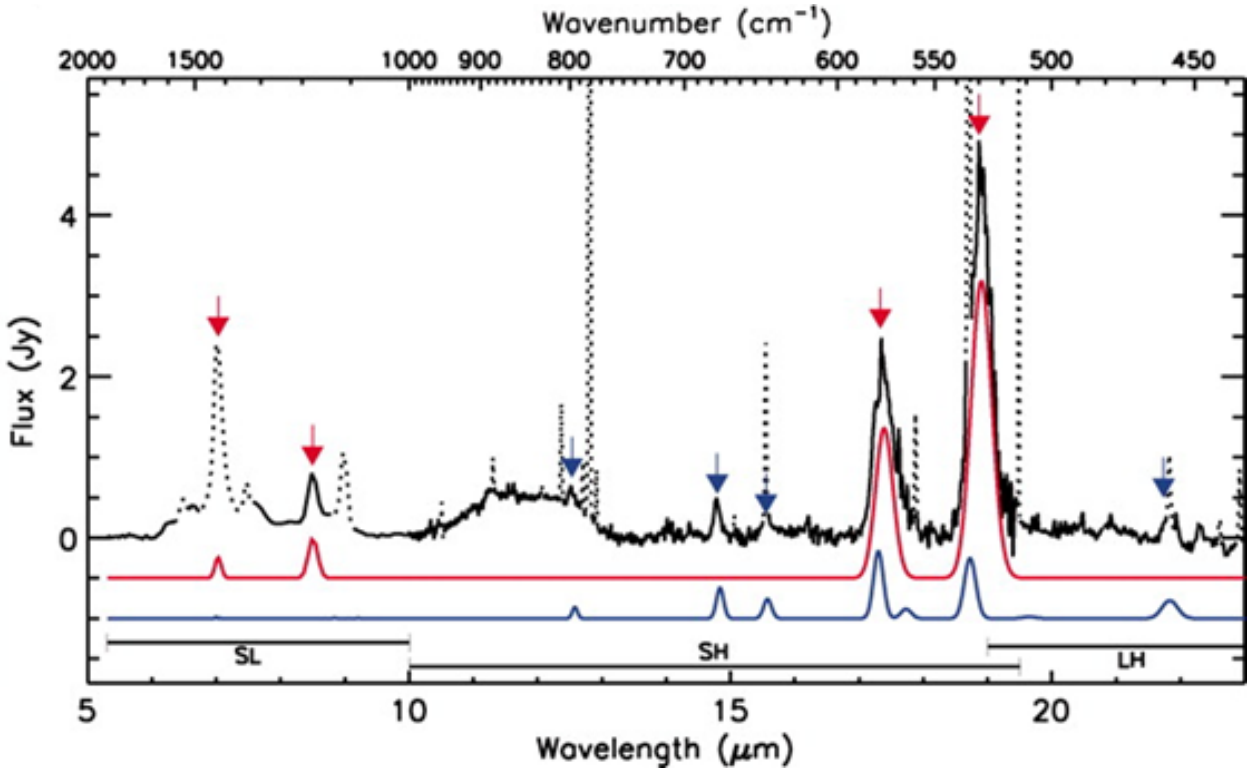

Figure 1.1: Emission features of C_{60} and C_{70} in Tc1. The black trace shows experimental data from the Spitzer Space Telexcope, while the red and blue traces show simulated emission spectra from C_{60} at 330 K and C_{70} at 180 K, respectively. Dashed features are known atomic transitions, and the Spitzer module used for each region is indicated below the simulated traces. Figure taken from Cami *et al.* [5].

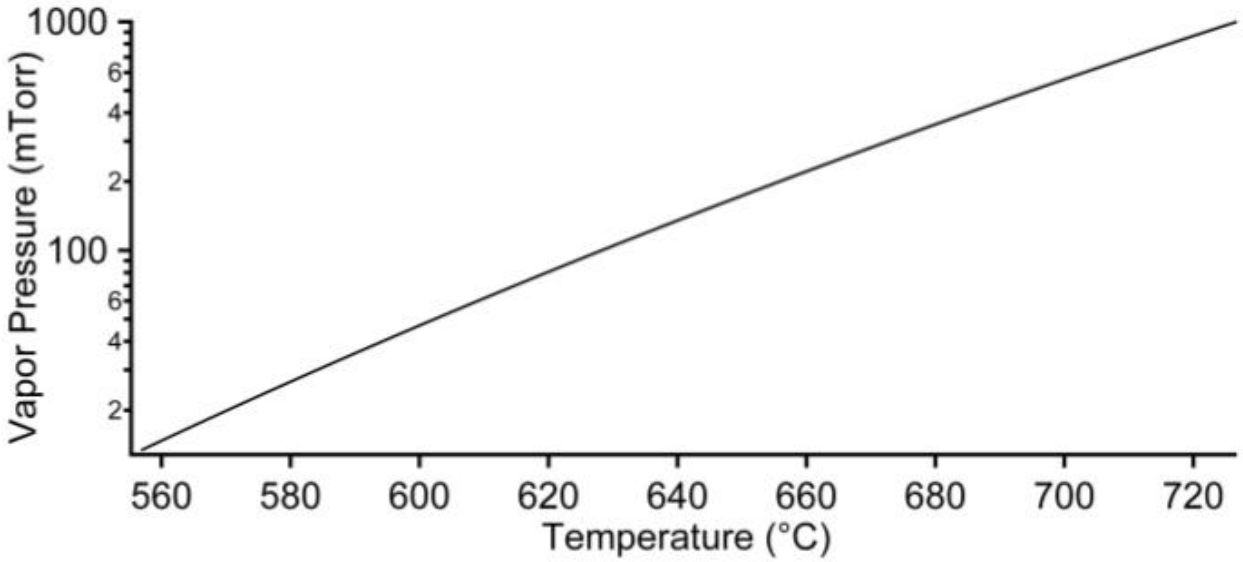

Figure 1.2: Vapor pressure of C_{60}. The black trace shows the vapor pressure of C_{60} as a function of temperature; for previous attempts to observe C_{60}, temperatures approaching 700 degrees Celsius were used. Figure taken from the doctoral thesis of Brian Brumfield [30].

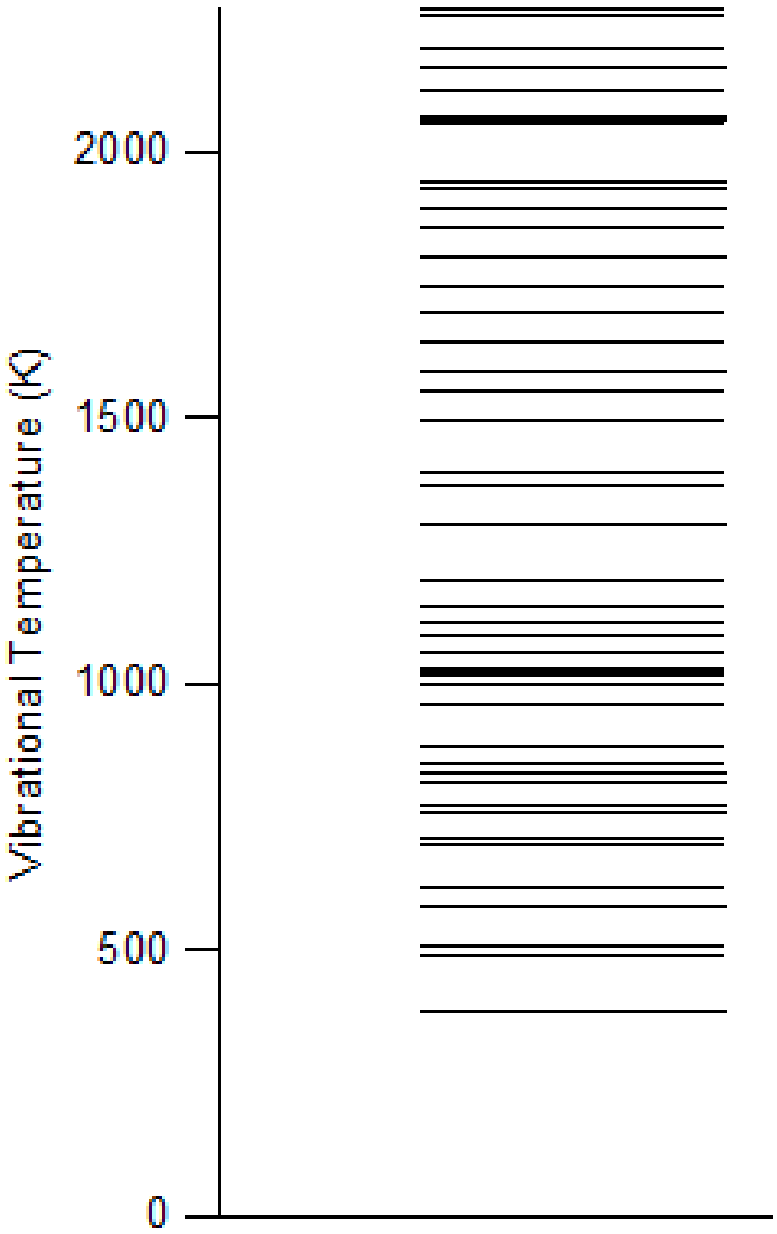

Figure 1.3: Distribution of vibrational states in C_{60}. The black lines represent the vibrational states of C_{60}, plotted against their respective vibrational temperatures on the y-axis. Notably, the density of states becomes very low below 500 K, making efficient vibrational cooling via supersonic expension extremely difficult.

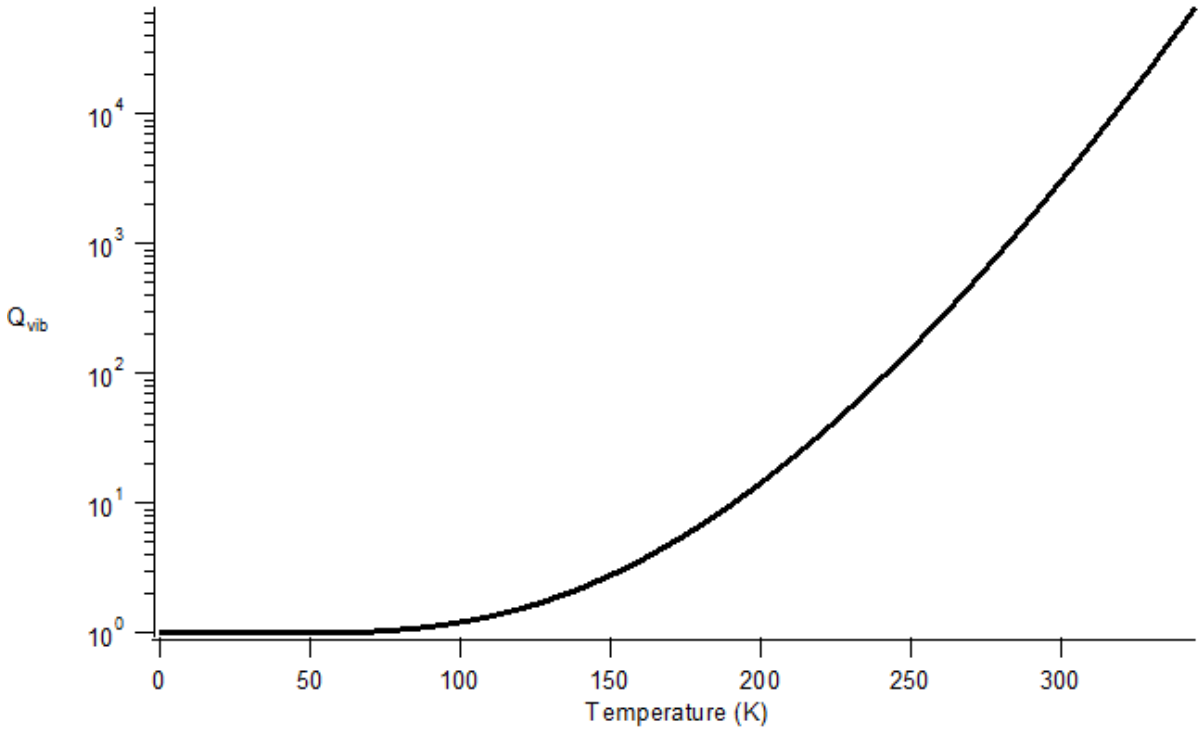

Figure 1.4: Vibrational partition function of C_{60}. The black trace shows the value of the vibrational partition function of C_{60} as a function of temperature. Because of the many vibrational degrees of freedom of C_{60}, the partition function grows very rapidly with increasing temperature, making effective vibrational cooling critically important in any attempt to observe an absorption spectrum in the laboratory. Figure taken from Stewart *et al.* [13].

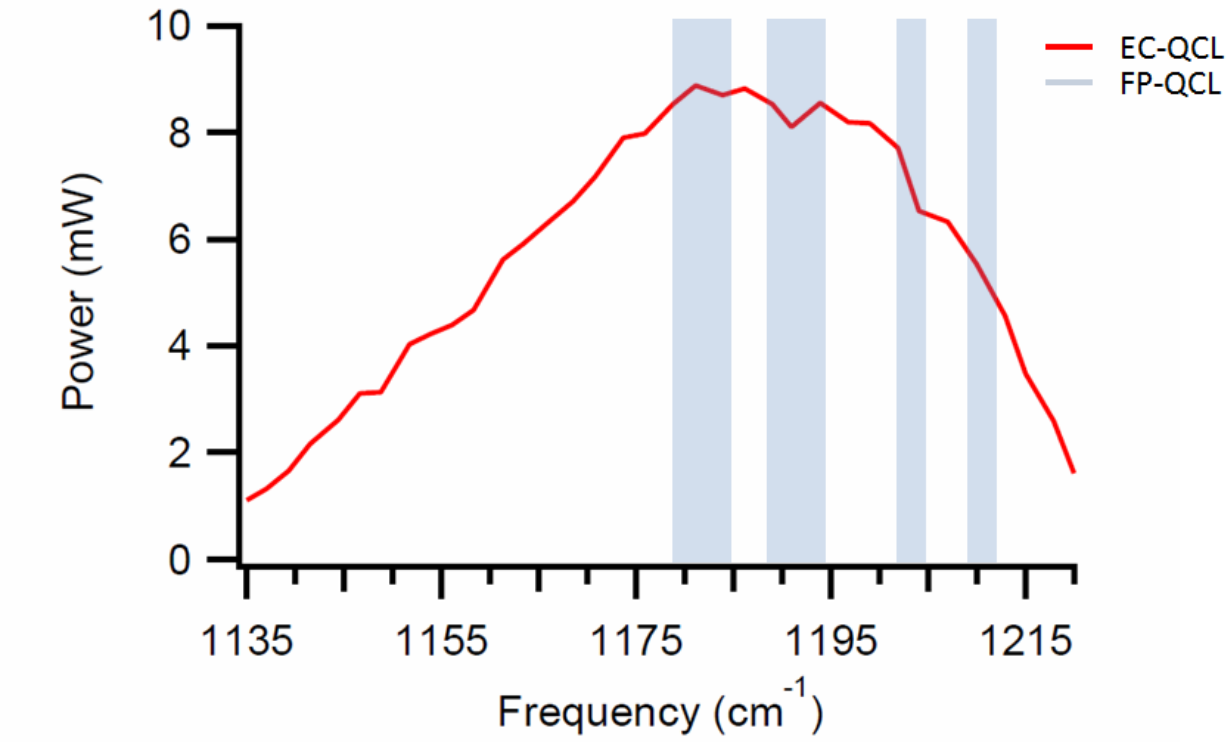

Figure 1.5: Tuning range comparison for Fabry-Pérot and external-cavity quantum cascade lasers. The red trace shows the useful tuning range of the external cavity quantum cascade laser, while the blue bars represent accessible ranges for the Fabry-Pérot laser. Note that while the Fabry-Pérot laser had sizeable coverage gaps, the external-cavity laser had continuous frequency coverage in this region. Figure adapted from Gibson *et al.* [31].

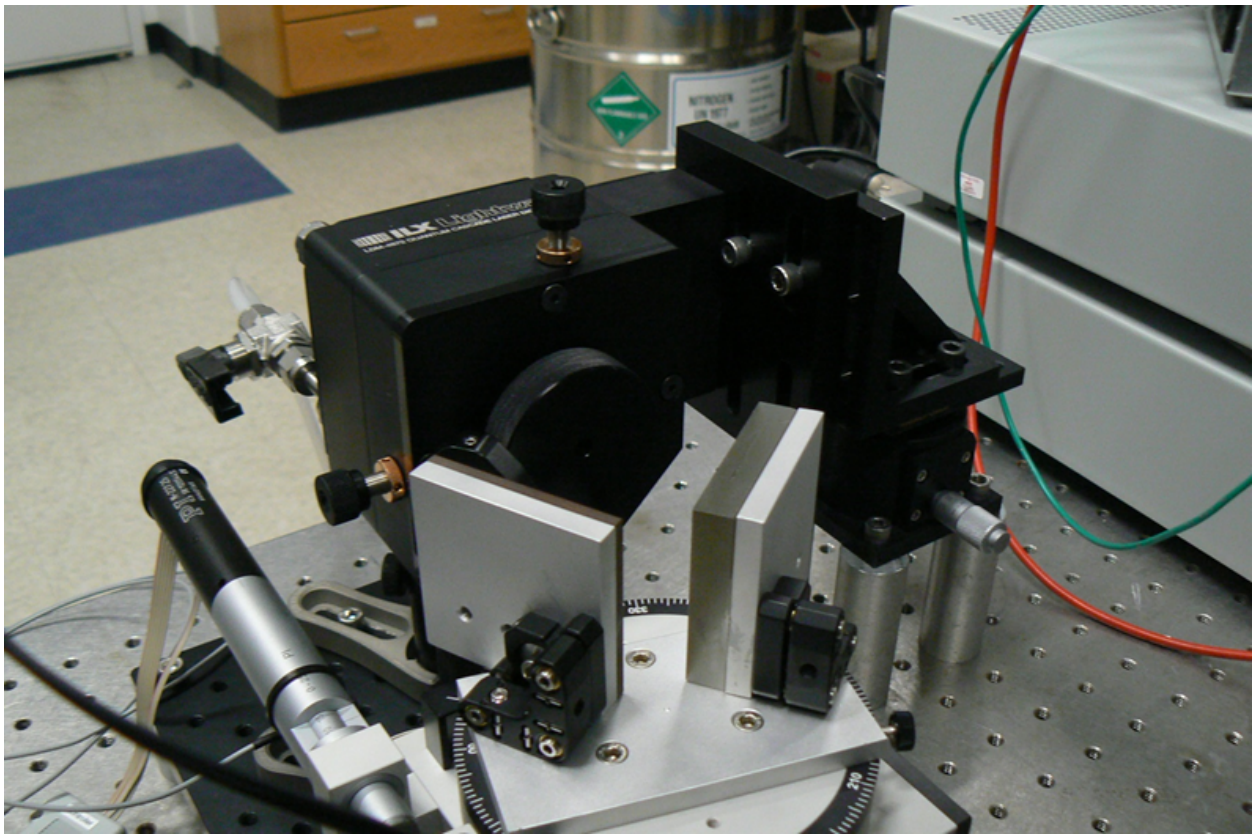

Figure 1.6: Photograph of the external-cavity quantum cascade laser. Shown are the laser housing from ILX Lightwave and the external cavity grating, mounted on rotation and translation stages from Physik Instrument. The current and temperature controllers were also provided by ILX Lightwave.

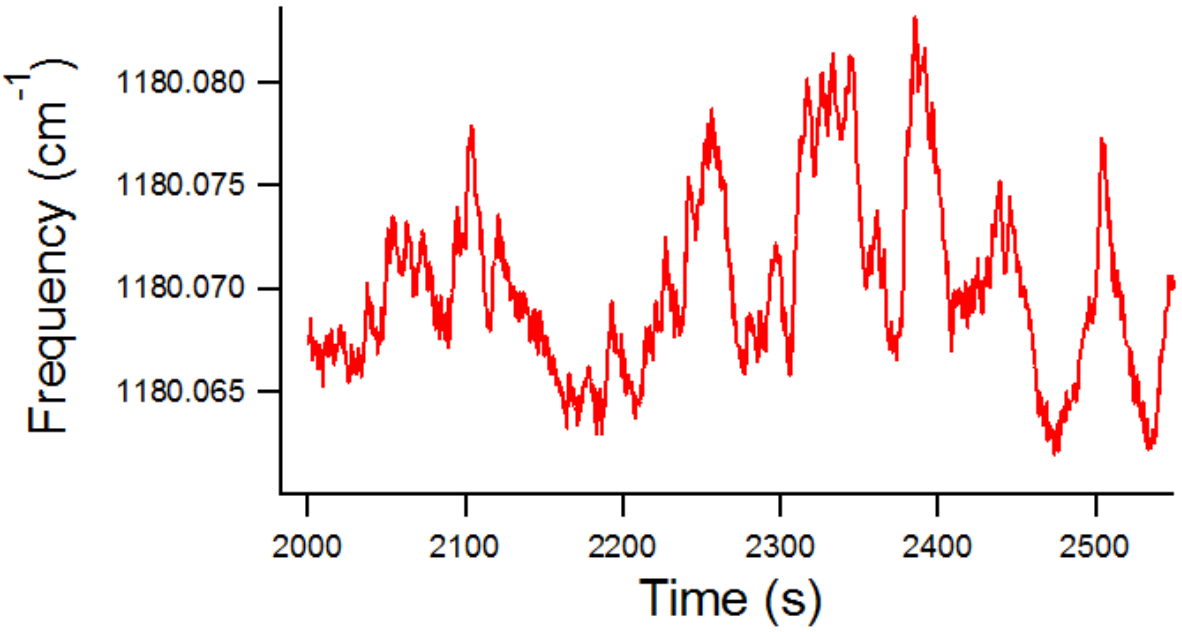

Figure 1.7: Frequency stability of the free-running external-cavity laser. The red trace shows the frequency of the external-cavity laser over time, as determined by wavemeter readings. Although the laser was meant to be held at a constant wavelength during these measurements, peak-to-peak fluctuations of over 300 MHz and a standard deviation of approximately 130 MHz are seen.

Chapter 2

Tilt-Tuned Side-of-Fringe Laser Locking

2.1 Introduction

Tilt-tuned etalons have been used as intra-cavity filters in lasers for decades [32] and continue to see use in modern laser designs [33]. Frequency-locking of lasers to etalons outside of the resonator cavity is also a well-established technique [34]. It is common to see lasers locked to etalons that are length- [34] or index-tuned [35], but to the best of our knowledge there are no reports in the literature of locking to a tilt-tuned etalon to stabilize a tunable laser. Although length- or index-tuning are effective approaches, tilt-tuning can provide stability and tuning characteristics suitable for applications in molecular spectroscopy at lower cost and experimental complexity.

Here, we present a tilt-tuned etalon locking system capable of maintaining MHz-level short-term stability over a single-scan tuning range of 0.4 cm^{-1} or more for an external-cavity quantum cascade laser (EC-QCL) centered near 1185 cm^{-1}. The system was constructed primarily from commercially-available components at a cost of less than $5,000 (USD), and could easily be adapted to work with tunable lasers of any wavelength for which suitable etalons and detectors are available. It is not our intent to demonstrate extremely high frequency stability in this work; rather, we wish to show that a tunable laser with poor frequency stability can be made suitable for routine spectroscopy easily and at low cost using this technique. For more demanding applications, the frequency stability of the system could easily be increased through a number of simple modifications (balanced detectors, active temperature control, lower thermo-optic coefficient etalon, use of a full PID servo [36], etc.).

This chapter is adapted with permission from B. M. Gibson and B. J. McCall, Optics Letters 40, 2696 (2015), Copyright 2015, Optical Society of America.

2.2 Experimental

In our technique the locked laser is tuned by changing the free spectral range (FSR) of the etalon, which is given by the familiar formula

$$\mathrm{FSR} = \frac{c}{2nd\cos(\theta)} \tag{2.1}$$

where c is the speed of light, n is the refractive index of the etalon, d is the etalon thickness, and θ is the angle of light propagation within the etalon relative to the etalon surface. The FSR can thus be tuned by altering n, d, or θ, with θ tuning providing a non-linear response (see Fig. 1). The non-linearity of angle tuning can be convenient from an experimental perspective. The device used to tilt the etalon may be limited in terms of tilt range or minimum step size; changing the initial value of θ allows the user to optimize for maximum scanning range or minimum step size of wavelength tuning. The maximum allowed angle of incidence is limited by walk-off losses and the clear aperture of the etalon.

Once a laser has been locked to a given etalon fringe, tuning the FSR results in a proportional change in the fringe and laser frequencies. This also means that noise in the FSR will be mapped onto the laser frequency. Temperature fluctuations, which alter both the etalon length and refractive index, can be prevented by placing the etalon in a temperature-controlled oven; alternatively, simply enclosing the etalon to prevent air flow can slow temperature tuning enough to be handled through simple fitting procedures. Changes to the angle of incidence can be lessened through vibrational isolation and can also be mitigated somewhat by using an etalon material with a high refractive index.

The laser we have stabilized in this work is an EC-QCL based on designs by Wysocki *et al.* [37]. In its free-running state, the laser has a mode-hop-free tuning range of approximately 0.7 cm^{-1} and a short-term frequency jitter of 150 MHz, measured as the maximum peak-to-peak wavelength change while recording wavelength readings on a Bristol 621B wavemeter. This level of frequency jitter significantly impaired the laser's performance in high-resolution spectroscopy applications (Fig. 2).

To stabilize the EC-QCL, a side-of-fringe locking servo was built around a 2" solid germanium etalon (Light Machinery) (Fig. 3). Light transmitted through the etalon was focused onto a PVM-10.6 MCZT detector (Boston Electronics), with the detector signal being passed to a home-built analog locking circuit. The difference between the detector level and a reference voltage was passed through an integral-only gain channel and applied to the three tuning elements of the EC-QCL (injection current and piezoelectric transducers controlling external cavity length and grating angle). The use of integral gain greatly simplifies lock maintenance during wavelength tuning; although the inclusion of proportional and differential gain would

have improved the high-frequency response of the circuit, this proved unnecessary for our application.

To allow tilt-tuning of the etalon and the locked laser, the etalon was mounted in an Agilis AG-M100L piezo-driven optic mount (Newport). The maximum angular tuning range and minimum step size of the mount were 4 degrees and 0.2 arcseconds, respectively. The etalon was set to an initial angle of approximately 8 degrees; during laser scanning, the etalon angle was decreased to approximately 5 degrees in steps of 0.003 degrees . This typically leads to a frequency slew of 0.4 cm^{-1} in steps averaging 12 MHz, but the tuning range can vary by $\pm$ 0.05 cm^{-1} depending upon slow etalon temperature drifts. Sub-MHz steps would be easily achievable with the minimum angular step size of the mount if needed. A simple cardboard enclosure was placed around the etalon to eliminate air currents and ensure that temperature drifts were slow relative to the angle tuning. It should be noted that using stepped angle tuning rather than a constant slew necessitates a slight delay (<0.1 s) between stepping the etalon and recording data while the lock stabilizes.

Lock acquisition and tuning were automated using a Beaglebone Black development board and a custom Python script. To acquire a lock, the etalon angle is first swept over two fringes as detector voltages are recorded by an analog-to-digital converter. The median voltage is then selected as the setpoint for the lock and the etalon is returned to its starting position. A small offset voltage is applied to the EC-QCL tuning elements before the integral gain channel is enabled; this procedure allows the laser to consistently lock to the side of the nearest fringe without user intervention. The etalon angle is then stepped whenever the scanning software sends a signal to slew the laser. Should the laser come unlocked during the scan, the lock will typically be reacquired immediately on a nearby fringe; the scan can then be continued without user intervention, although some additional work will be required during calibration to account for the frequency jump.

2.3 Results and Discussion

To characterize the locking performance, frequency readings were taken with a Bristol 621B wavemeter and voltage readings were taken at the integral gain input with a Bitscope10 USB oscilloscope. Thirty-minute data sets at a constant etalon angle were taken for the unlocked laser, the locked laser without an enclosure and the locked laser with an enclosure. To demonstrate locked tuning, data was also obtained for the locked, enclosed laser as the etalon angle was stepped from 8 degrees to 5 degrees.

A comparison of wavelength stability between the locked and free-running laser shows a significant improvement in short-term stability, but a drastic increase in long-term drift (Figs. 4, 5A). This long term drift appears to be a result of thermal tuning of the germanium etalon. This could be addressed through

active temperature control of the etalon or by using a material with a lower thermo-optic coefficient, such as zinc selenide. However, enclosing the etalon to limit airflow appears to slow the thermal drift enough to allow effective fitting of the frequency tuning profile.

Limitations to the precision of our wavelength readings prevent adequate characterization of our short-term wavelength stability. To address this, voltage readings at the integral gain input were obtained and converted to frequency offsets from our lock point (Fig. 5B). At short timescales we see an improvement of more than an order of magnitude over the free-running laser, with Allan deviations on the order of 1 MHz for one-second integration times. As these measurements do not account for drifting of the lockpoint (e.g. through temperature tuning of the etalon), they do underestimate the long-term frequency jitter of the locked laser.

Wavelength readings were also taken during a 3 degree scan of the etalon, which generally equates to a frequency tuning range of approximately 0.4 cm^{-1}, over 20 minutes; in this case, the temperature drift of the etalon decreased the tuning range slightly (Fig. 1). As can be seen in Fig. 1, the tuning profile varies somewhat from the expected 1 / cos(θ) curve; this is partially the result of temperature drift and partially due to slight changes in alignment as the etalon angle was scanned. The scan can still be effectively calibrated through a simple polynomial fitting procedure.

2.4 Conclusion

In summary, we have developed a simple, low-cost frequency stabilization system for tunable lasers based on locking to a tilt-tuned etalon. The locking system improved the stability of our laser during scanning by more than an order of magnitude to approximately 1 MHz deviation over a one-second integration. A typical scan can cover 0.4 cm^{-1} with a 12 MHz step size, but both longer scanning ranges and smaller steps are easily achievable by altering the initial angle of the etalon. Likewise, for more demanding applications the stability of the locked laser could easily be improved through active temperature stabilization, balanced detection, and optimized locking electronics. The same approach can be easily adapted to other laser types and wavelength regions.

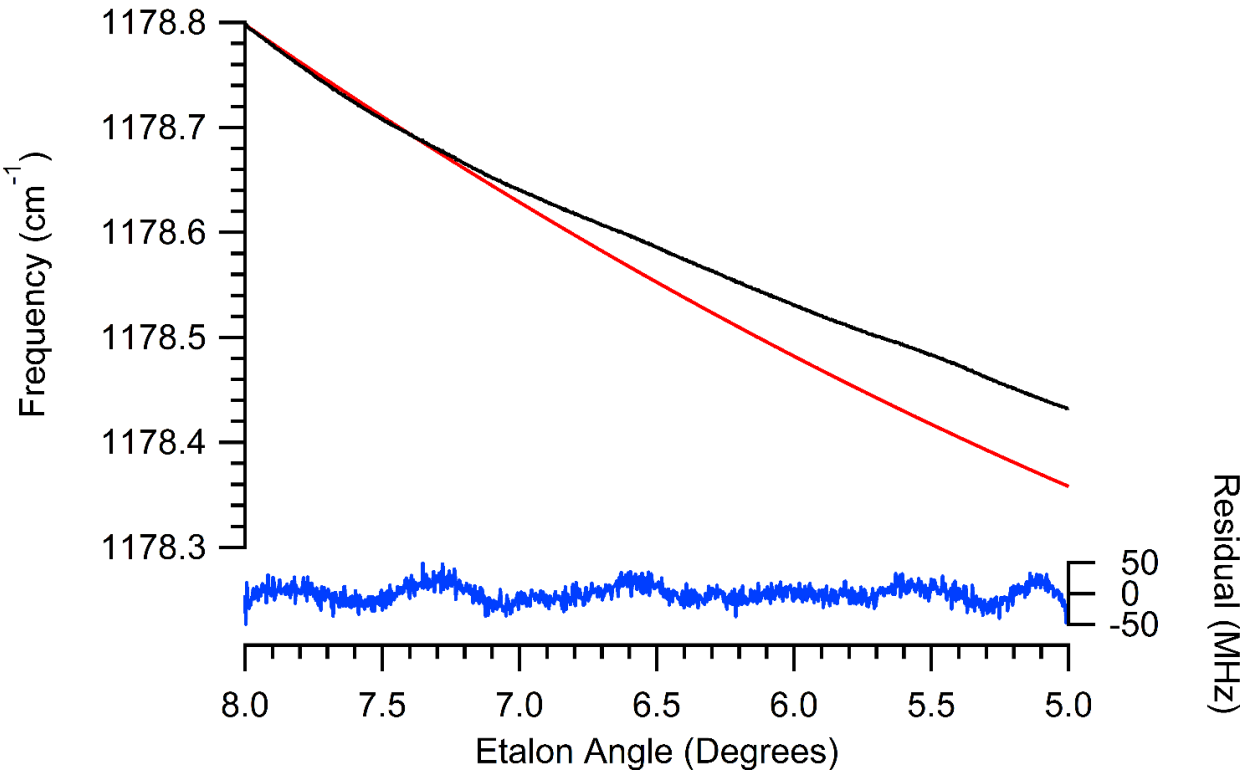

Figure 2.1: Simulated and experimental tilt-tuning curves. The black top trace shows frequency readings for a typical locked laser scan over an estimated 3 degree etalon slew. The red middle trace shows the simulated frequency shift of a given etalon fringe over the same angular tuning range. The blue bottom trace shows residuals of a polynomial fit of the experimental data.

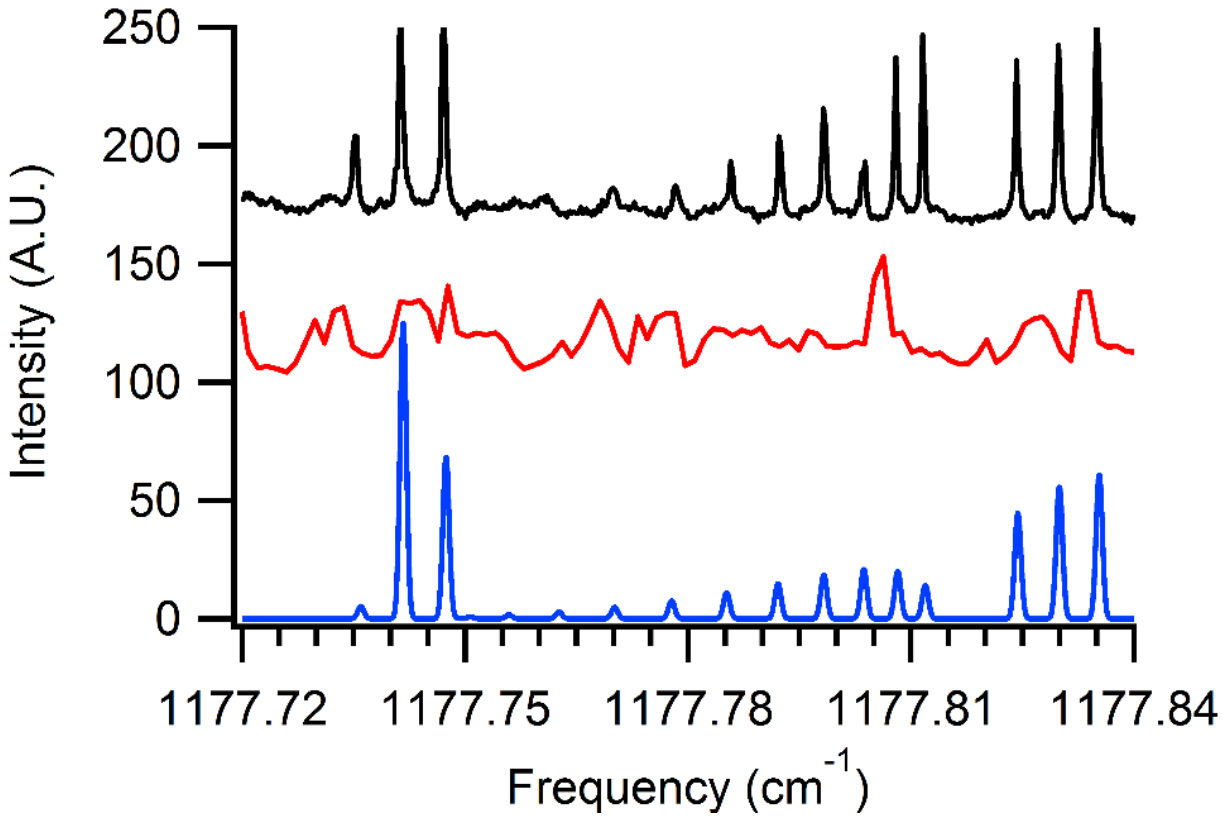

Figure 2.2: Comparison of spectroscopic performance for the locked and unlocked laser. The spectra above show a Q-branch and several R-branch lines from the ν_{16} band of 1,3,5-trioxane. The black top trace was obtained with the locked laser, the red middle trace was obtained with the free-running laser and the blue bottom trace shows a simulated spectrum produced with PGOPHER [38]. The locked spectrum clearly shows spectral structure that cannot be resolved in the free-running spectrum. A full discussion of the 1,3,5-trioxane spectrum is available elsewhere [31].

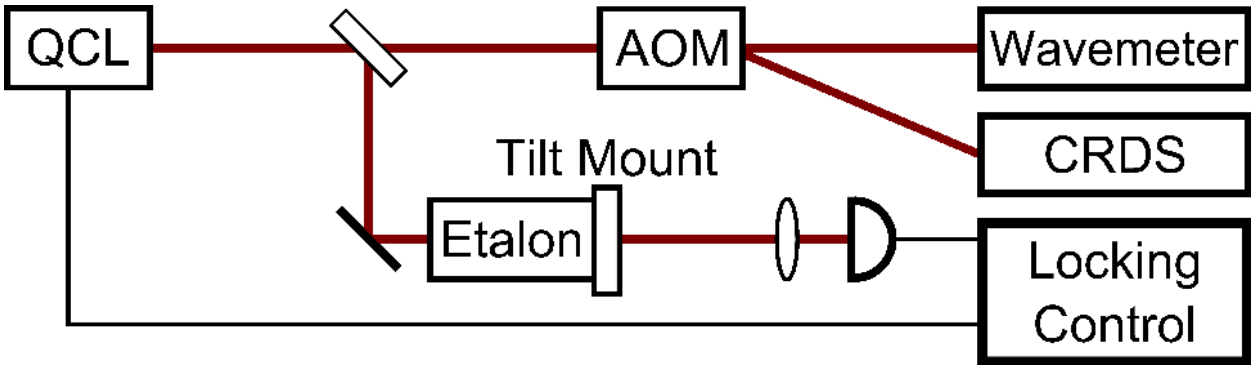

Figure 2.3: Experimental layout for side-of-fringe locking. The tilt-tuned etalon locking system was integrated into our existing cavity ringdown spectrometer. A beamsplitter was placed before the acousto-optic modulator to direct a portion of the beam through a 2" germanium etalon mounted in an AG-M100L piezo-driven optic tilt mount. Light transmitted through the etalon was focused onto a PVM-10.6 detector. The detector signal was fed into the locking electronics, which control the tuning mechanisms of the laser. Full details of the spectrometer are available elsewhere [31].

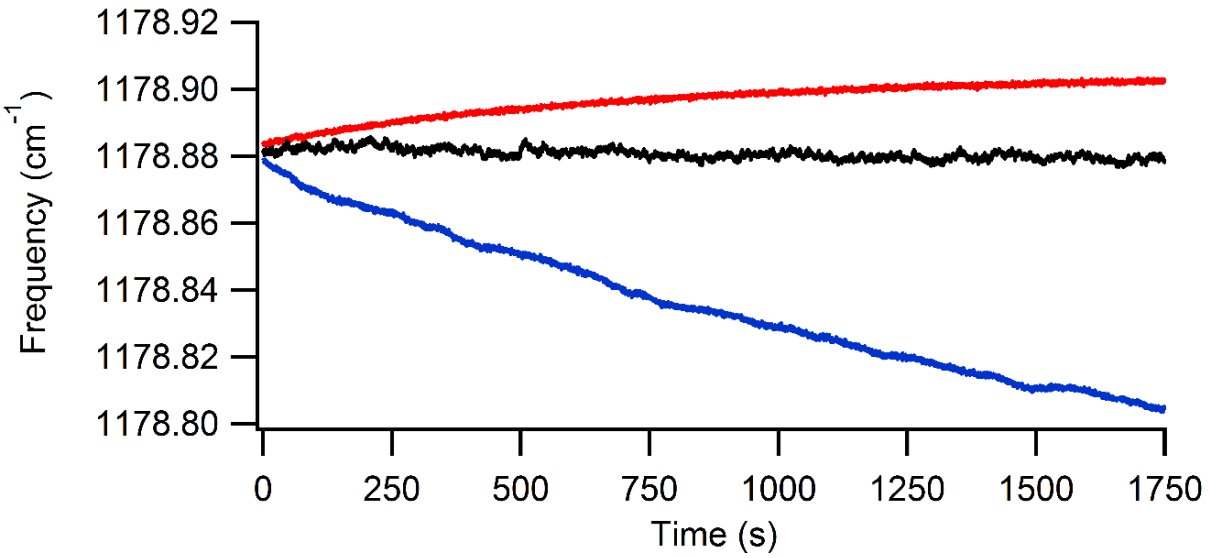

Figure 2.4: Frequency stability comparison for side-of-fringe locking. The black middle trace shows the frequency stability of the free-running laser. The blue bottom trace shows the laser locked to an unenclosed etalon; although the short-term stability is clearly improved, significant long-term drift is introduced due to thermal drift in the etalon. The red top trace shows the laser locked to an enclosed etalon. By limiting airflow, thermal drift in the etalon is signficantly decreased.

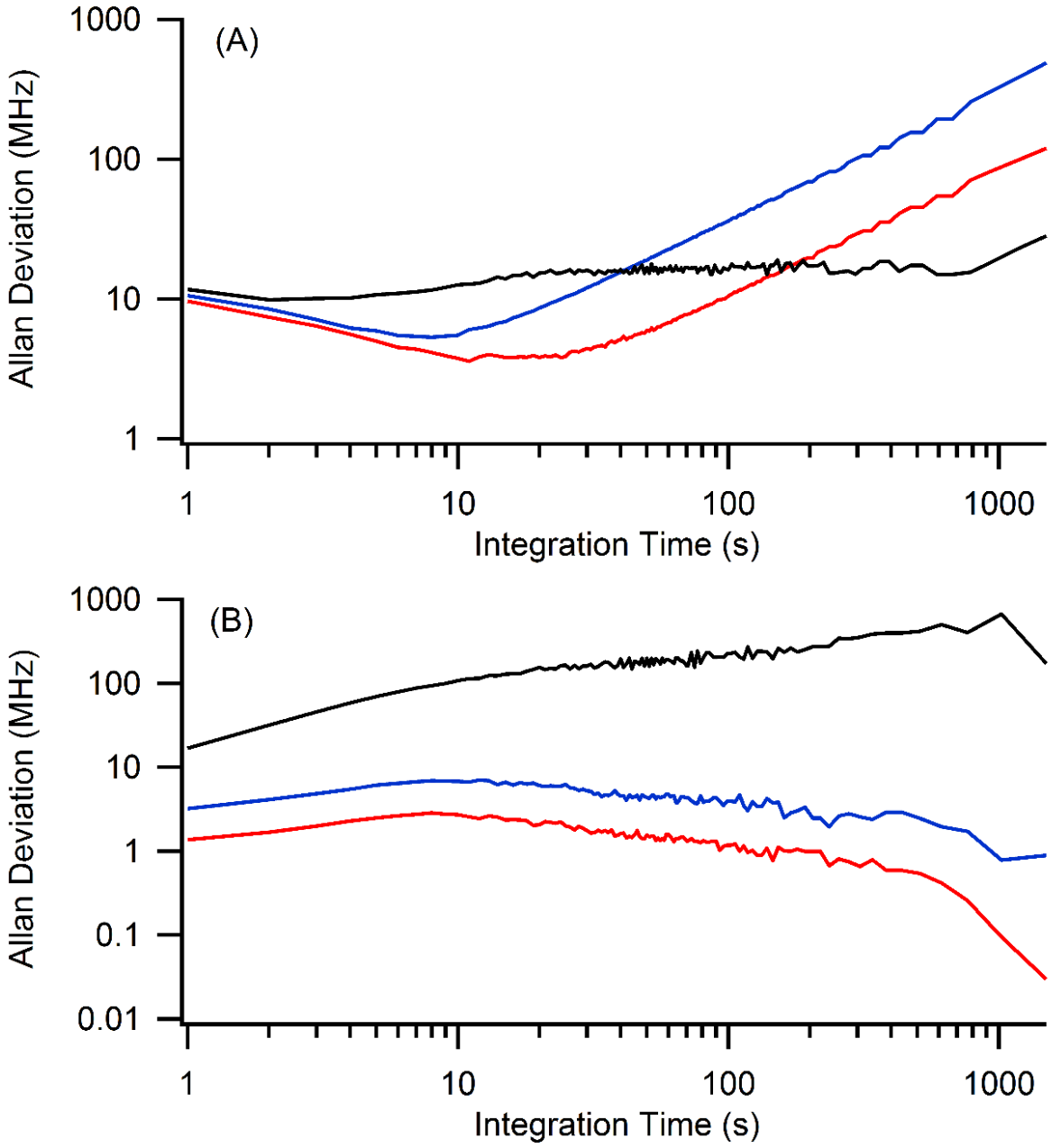

Figure 2.5: Allan-Werle plots for the free-running and etalon-locked laser. The black top traces show the free-running laser, the blue middle traces show the laser locked to an unenclosed etalon and the red bottom traces show the laser locked to an enclosed etalon. (A) Frequency readings were obtained using a Bristol 621B wavemeter, showing a clear increase in the long-term drift for the etalon-locked traces; the precision of the frequency readings limits comparisons at shorter timescales. (B) Error signal voltages from the locking circuit were converted to frequency offsets to provide more accurate stability data for short timescales. As these do not account for drift in the lock point, they are less reliable at long timescales.

Chapter 3

Rotationally-Resolved Spectroscopy of 1,3,5-Trioxane

3.1 Introduction

1,3,5-trioxane is a three-unit cyclic polymer of formaldehyde, making it one of the smallest members of the polyoxymethylene (POM) class of molecules. For many years various forms of POM have been proposed as extended sources of formaldehyde in cometary comae, which would make them highly relevant to studies of prebiotic chemistry [20, 21]. Although various forms of POM, including trioxane, have been observed in laboratory simulations of cometary conditions [20], to date there have been no conclusive astronomical detections. Since trioxane is both a relatively volatile example of POM and a photodegradation product of larger polymers, it could serve as a useful tracer for POM in general in future work.

Trioxane is a symmetric top of the C_{3v} point group. Its ground state microwave spectrum was observed in 1963 by Oka *et al.* [23], and the rotational spectra of a number of excited states have been observed since [24, 25, 26, 27, 28]. The ν_{17} ro-vibrational band was observed by Henninot *et al.* in 1992 [29]; prior to the present work, this was the only portion of trioxane's vibrational spectrum observed with rotational resolution.

In this work, we present a rotationally-resolved absorption spectrum of the ν_{16} band of trioxane, centered near 1177 cm^{-1}, observed through cavity ringdown spectroscopy with a continuous-wave external-cavity quantum cascade laser (EC-QCL). The availability of an atmospheric window in this region makes this band well suited for astronomical observations, as it would allow the use of ground- or stratosphere-based telescopes. A successful detection of cometary trioxane could provide a greater understanding of the formation of formaldehyde and other important organic compounds.

This chapter is adapted with permission from B. M. Gibson, N. C. Koeppen, and B. J. McCall, Journal of Molecular Spectroscopy 317, 47 (2015), Copyright 2015, Elsevier Inc.

3.2 Experimental

The spectrometer used in this work (Fig. 1) is a modified version of the QCL-based cavity ringdown spectrometer we have described previously [39, 40]. Briefly, continuous-wave laser light is coupled into a high-finesse optical cavity around a continuous supersonic expansion containing the molecule of interest. A germanium acousto-optic modulator (AOM) (ISOMET) is used as a fast shutter, triggered when the light transmitted by the cavity passes a user-defined threshold to initiate a ringdown event. Using the non-diffracted beam, relative frequency calibration is obtained using a Bristol 621B wavemeter; absolute frequency calibration is obtained from the diffracted beam using a triple-pass direct absorption SO_2 reference cell. Rather than locking the laser to the ringdown cavity, the cavity length is dithered by >1 free spectral range at a rate of approximately 250 Hz using a piezo-electric modulator, ensuring that the laser will be on-resonance with the cavity twice per cycle. Back reflection isolation is achieved using a linear polarizer and a Fresnel rhomb.

The primary difference between the current spectrometer and its past incarnations is the incorporation of an EC-QCL in place of the Fabry-Pérot QCL (FP-QCL) used previously. Our EC-QCL uses a Littrow configuration based on designs by Wysocki *et al.* [37] and utilizes a gain chip provided by the Wysocki lab. In comparison to the FP-QCL, our new EC-QCL features significantly improved tuning range (Fig. 2) and thermo-electric rather than cryogenic cooling at similar output power. The tuning range could also be easily shifted by swapping gain chips without otherwise altering the laser. These features significantly increase the breadth of spectroscopic targets available to our instrument.

However, the addition of wavelength-selective elements that are highly sensitive to mechanical vibrations and acoustic noise caused significant issues with the stability of the lasing frequency. Immediately after completion, the EC-QCL frequency had a peak-to-peak frequency jitter of over 450 MHz at short ($\sim$ 1 s) timescales. Floating the optical table on vibrational isolation legs and detaching the table from our vacuum chamber decreased this jitter to 150 MHz, but made it difficult to maintain consistent alignment of the ringdown cavity, which is attached to the vacuum chamber. To keep alignment consistent, the gap between the optical table and the ringdown cavity was bridged with a hollow silica waveguide (Opto-Knowledge). This solved the alignment issues while maintaining vibrational isolation.

To further improve the frequency stability of the EC-QCL, a tilt-tuned germanium etalon locking system was implemented. This system, which is described in detail elsewhere [41], improved the frequency stability to $\sim$ 1 MHz over a one-second integration time. The laser is adjusted by applying corrections to the injection current, the external cavity length, and the grating angle at fixed ratios that were determined experimentally. The lock point, and thus the laser frequency, is tuned by tilting the germanium etalon relative to the incident

laser. In the current configuration, this allows a single-scan, mode-hop-free tuning range of ~ 0.4 cm^{-1} and an average step size of ~ 12 MHz; either could be easily adjusted by changing the parameters of the locking system. At present, the locking system is the limiting factor for the mode-hop-free tuning range; for the free-running laser, the range was limited by the cavity length travel to approximately 0.7 cm^{-1}.

To obtain relative calibration, ringdown data collection is paused once per 100 data points to collect a wavemeter reading. Because the germanium etalon used for locking is temperature sensitive, it is possible for significant thermal drift to occur between wavemeter readings; the spacing between these readings therefore entails a tradeoff between accurate calibration and scanning speed. Laser power limitations prevent us from using an experimental layout that would allow for constant wavemeter readings. The readings we do obtain are fit to a fifth-degree polynomial to produce a frequency scale, which is in turn offset by matching the SO_2 reference cell data to HITRAN08 [42]. This corrects for the Bragg shift of the AOM and any systematic offset in the wavemeter readings.

A supersonic expansion of argon produced by a 12.7 mm $\times$ 150 μm slit at 2 atm backing pressure was used for this work. The argon flow was split between two paths before being recombined prior to the slit; the first path consisted of unobstructed tubing, while the second passed through a bed of solid trioxane before encountering a needle valve. The ratio of argon flow through each arm could be controlled by adjusting the needle valve, allowing an adjustable amount of trioxane in the expansion. Furthermore, in order to limit the effect of high temperature gas outside of the expansion, tubes were extended between the ringdown mirrors and the expansion nozzle. A flow of nitrogen through these tubes limited the amount of high-temperature trioxane in the beam path.

3.3 Results and Discussion

Ro-vibrational spectra were obtained for trioxane between 1175.93 and 1179.28 cm^{-1} (Figs. 3,4), with an average step size of 12 MHz. This range included several Q-branches and portions of both the P and R branches. Fitting was performed using PGOPHER [38]; 219 transitions were assigned with an average fitting residual of 26.02 MHz. The rotational parameters obtained are presented in Table 1. Ground state parameters were fixed at the values obtained by Gadhi *et al.* [28] where available, and excited-state values for D_J and the sextic centrifugal distortion constants have been fixed at the ground-state values. C$''$ has not yet been determined experimentally, but was fixed at an estimated value of 2950 MHz for this work [28, 43]. We note that ν_0, ζ, and C$'$ are dependent upon the value of C$''$; expressions independent of the value of C$''$ have been provided instead.

The relatively large uncertainty in the fit can be attributed to the uncertainty of our relative frequency calibration. Approximately two minutes pass between wavemeter readings; during this time, the laser's frequency can drift from the expected tuning curve. We estimate that, between fitting errors and uncertainty in the wavemeter readings, our frequency calibration is accurate to approximately $\pm$ 32.7 MHz. This could be remedied by obtaining continuous wavelength measurements, though present laser power limitations prevent us from doing so via wavemeter.

Additionally, we note that relative intensities are inconsistent between experimental and simulated spectra. This appears to be due to undersampling of the absorption peaks in the experimental spectrum. Scans with smaller step sizes matched simulated intensities well, but the slower scan rate exaggerated the effects of etalon drift on the frequency calibration. As we are more concerned with frequency accuracy than intensities in this work, the faster scans were used.

3.4 Conclusion

The increased tuning range afforded by our new EC-QCL light source has allowed us to record the ν_{16} band of 1,3,5-trioxane, which has not previously been observed at rotational resolution. We have been able to assign 219 transitions in this band and obtain excited-state rotational constants. In addition to demonstrating the capabilities of our improved spectrometer, these data could be suitable for astronomical observations of trioxane, which is a potential tracer for the prebiotically-important polyoxymethylene class of molecules.

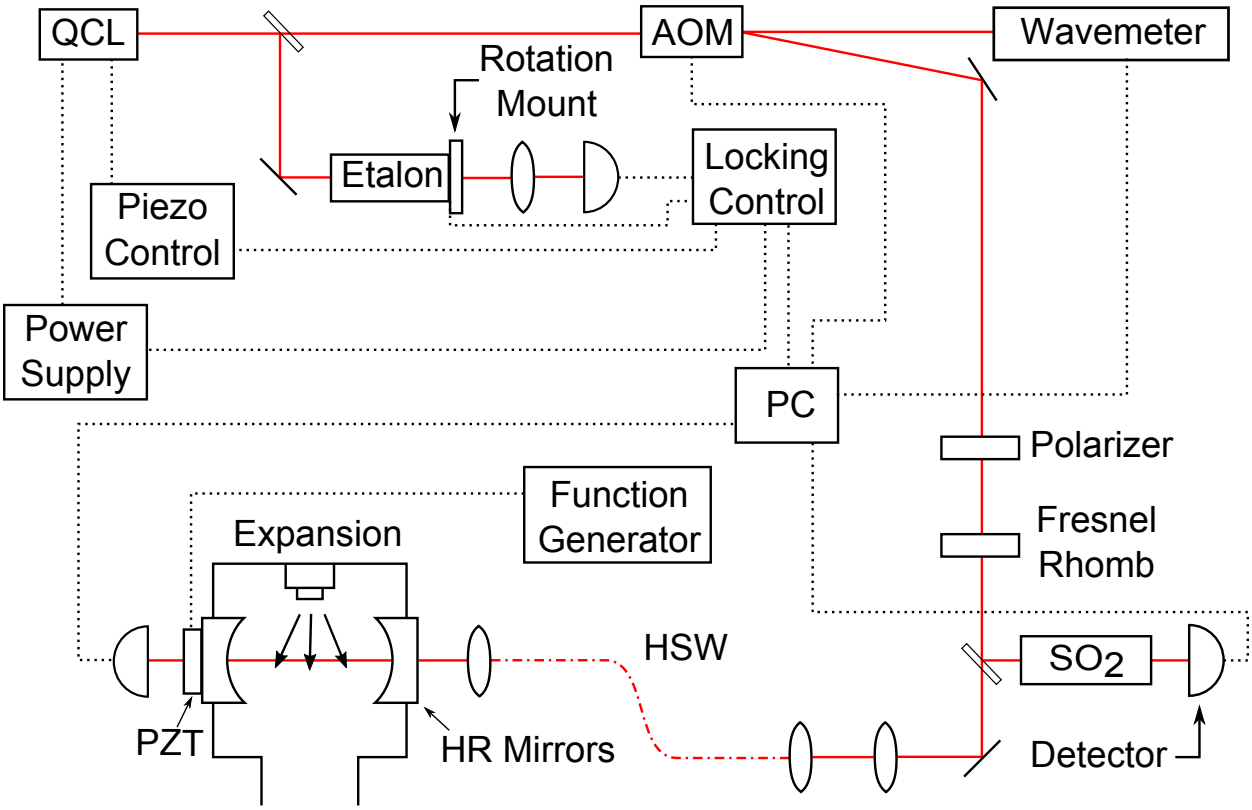

Figure 3.1: Experimental layout for trioxane spectroscopy. Solid red traces indicate the path of the laser in free space; the red dot-dash trace shows the path through the hollow silica waveguide (HSW). Black dotted traces indicate electronic conections.

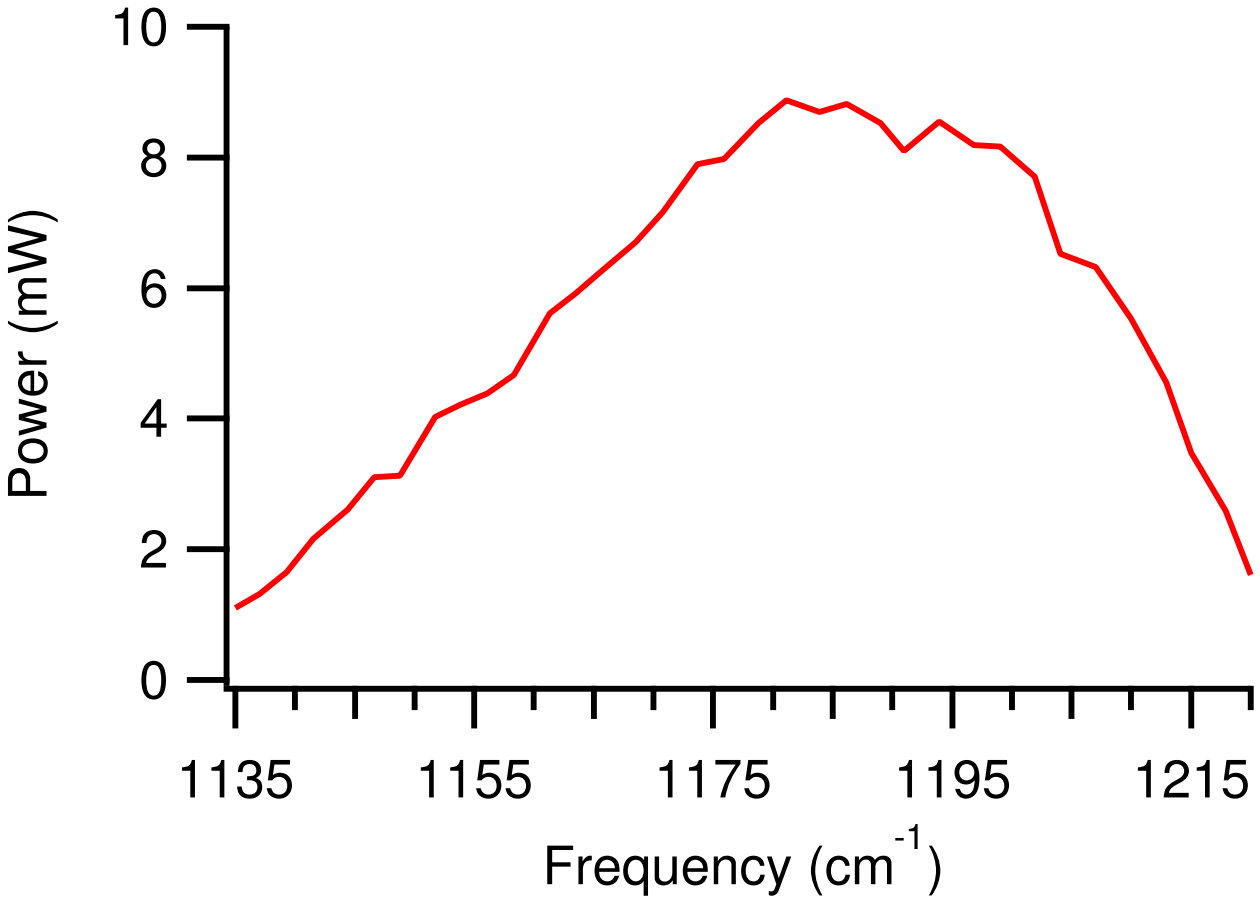

Figure 3.2: EC-QCL output power versus frequency. The inclusion of an EC-QCL in our spectrometer has expanded our useful tuning range from 1180-1200 cm^{-1} to 1135-1220 cm^{-1} in comparison to the FP-QCL used previously [39, 40].

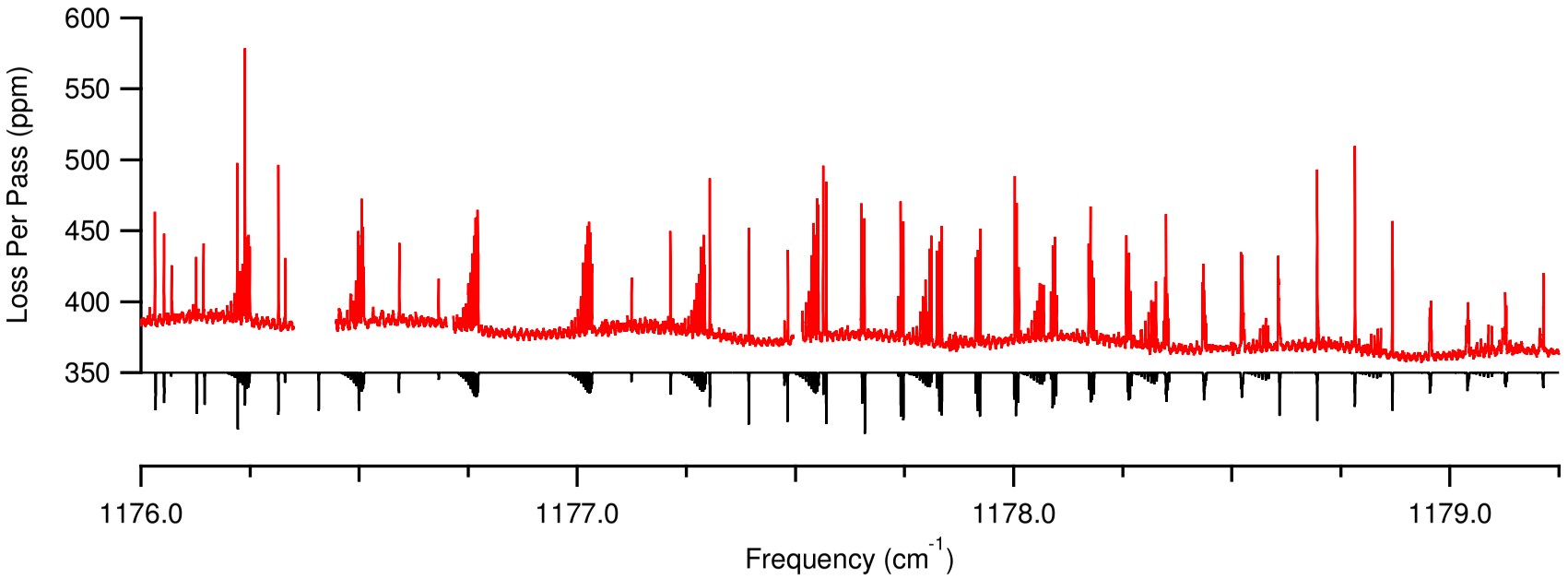

Figure 3.3: Experimental and simulated spectra of the ν_{16} band of 1,3,5-trioxane. The red top trace shows the experimental spectrum; the blank regions were not scanned or included in fitting. The slow baseline drift results from changes in mirror reflectivity, and the sinusoidal modulation is an effect of the etalon formed by the front and back faces of the mirrors. The lower black trace shows a simulated spectrum produced using PGOPHER[38].

Table 3.1: Listing of spectroscopic constants for 1,3,5-trioxane. The band origin is given in cm^{-1}. Quartic centrifugal distortion constants and the J(J+1) dependence of the Coriolis constant (η_J) are given in kHz; sextic centrifugal distortion constants are given in Hz. All other constants are given in MHz. Note that C″ is fixed at an estimated value of 2950 MHz. D'_J and the excited-state sextic centrifugal distortion constants were fixed to their ground state values.

	$v_{16} = 1$	v = 0 [28, 43]
$\nu_0 + (C' - B' - 2C'\zeta)$ (cm^{-1})	1176.77314(11)	-
B (MHz)	5262.624(51)	5273.25767(20)
$C'' - C'$ (MHz)	5.93(12)	-
D_J (kHz)	1.34622	1.34622(34)
D_{JK} (kHz)	-1.97(80)	-2.0243(15)
H_J (Hz)	0.00118	0.00118(10)
H_{JK} (Hz)	-0.00430	-0.00430(40)
H_{KJ} (Hz)	0.0031	0.0031(10)
$C' - B' - C'\zeta$	-3905.81(53)	-
η_J (kHz)	66(11)	-
q^+ (MHz)	2.40(20)	-

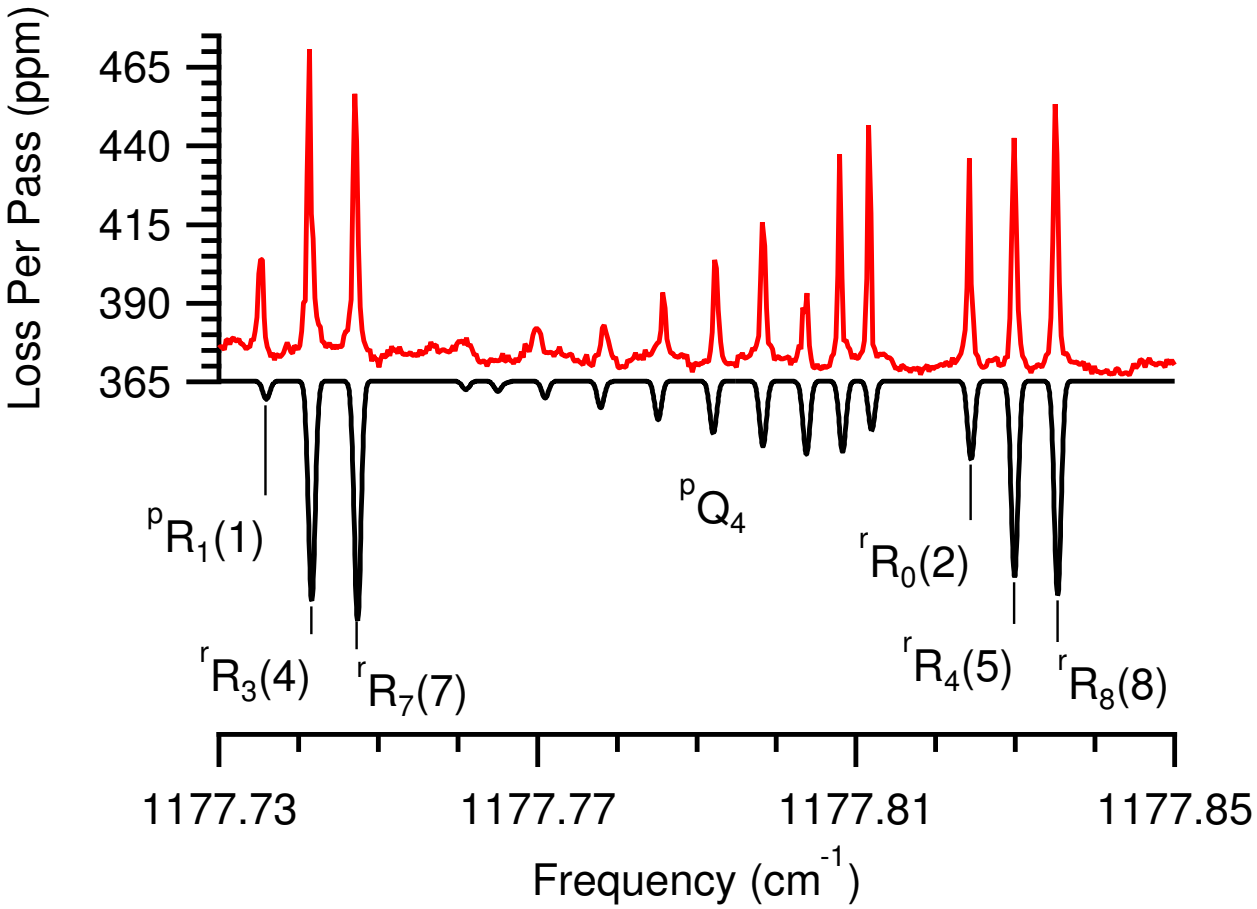

Figure 3.4: Expanded view of experimental and simulated spectra for 1,3,5-trioxane. The red top trace shows the experimental spectrum; the lower black trace shows the simulated spectrum. Differences in relative intensities are due to undersampling of peaks in the experimental spectrum.

Chapter 4

Supercritical Fluid Expansion Source

4.1 Introduction

Although thermal vaporization followed by cooling through supersonic expansion provides is a convenient method for many spectroscopic systems, it can be insufficient in cases where the required temperatures render the sample unusable. This can be the case with thermally labile molecules or in those for which supersonic expansion does not provide sufficient cooling from the vaporization temperature. The latter is the case with C_{60}; to achieve reasonable vapor pressures the sample must be heated to temperatures in excess of 900 K, and the poor density of vibrational states at low energies prevents effective vibrational cooling [13]. Because of this and the rapid growth of C_{60}'s partition function with increasing vibrational temperature, observation of the ground-state vibrational absorption spectrum through usual methods has proven impractical.

Bearing this in mind, we have considered a number of alternative methods for obtaining vibrationally-cold C_{60} vapor in sufficient quantity for absorption spectroscopy. One possible approach is laser ablation. However, the applicability of this method for C_{60} cannot be readily evaluated using available data - the amount of thermal energy imparted through laser ablation and the distribution of that energy between vibrational, rotational and translational degrees of freedom vary from molecule to molecule and substrate to substrate. It would be difficult or impossible to estimate the performance of such a source without first building it, which would be both expensive and time consuming.

An alternative method involves the expansion of a supercritical fluid containing C_{60}. A supercritical fluid expansion source has been previously described by Goates and coworkers [17] and used for spectroscopy of large polycyclic aromatic hydrocarbons. Essentially, the molecule of interest is dissolved in an appropriate supercritical fluid (typically composed of CO_2 and some co-solvent), which is then depressurized through a pinhole inside of the nozzle of a secondary supersonic expansion source. The initial temperature of the sample depends upon the temperature of the solvent system chosen as well as the temperature of the secondary expansion nozzle - this typically must be elevated to prevent the formation of aerosols. The

degree of cooling provided by this secondary expansion should then be similar to that of the simpler system described previously, with the added complication of expansion velocity matching - the primary expansion of supercritical fluid must closely match the velocity of the secondary argon expansion to ensure maximal cooling [17].

The effectiveness of a supercritical fluid expansion source for spectroscopy of C_{60}, or any other spectroscopic target, is therefore largely dependent upon the existance and properties of an appropriate supercritical solvent system. In the case of C_{60}, supercritical fluid extraction studies have shown that fullerenes have appreciable solubility in supercritical fluids composed of CO_2 and toluene [18, 19]. The minimum temperature of the fluid is dependent upon the CO_2:toluene mole fraction; for a ratio of 7:3, the critical temperature is approximately 450 K. As previous experiments provide only an upper limit to the efficiency of C_{60}'s vibrational cooling in a supersonic expansion we cannot accurately predict the final vibrational temperature of vapor produced through this method, but unlike the case of laser ablation we can confidently state that the pre-expansion temperature would be lower than that for thermal vaporization.

Although we expect the vibrational temperature of vapor produced through the supercritical fluid expansion to be lower, it is likely that the mass flow of C_{60} using a 7:3 solvent mixture will be considerably lower than that measured for thermal vaporization [13]. The data obtained through supercritical fluid extraction measurements [18, 19] do not correspond exactly to the conditions of our supercritical fluid expansion, but we estimate the total mass flow to be a factor of 10-20 lower than that of our thermal vaporization source. Depending on the efficiency of supersonic cooling, it is likely this will require some modifications to our existing spectrometer to obtain increased sensitivity. The practicality of obtaining sufficient sensitivity can be evaluated once experimental data are available to assess the mass flow and cooling efficiency of the supercritical fluid expansion source.

To that end, we have constructed a first-generation supercritical fluid expansion source and evaluated its performance prior to constructing a second-generation source correcting design flaws identified in the first. Results from the first-generation source were promising - spectroscopic observations of jet-cooled D_2O were made, and we confirmed the solubility of C_{60} in our selected solvent system. Evaluation of the second generation source is currently underway, using the previously-studied 1,3,5-Trioxane molecule [31] as a better measure of cooling efficiency; once this work has been completed, mass flow measurements will be made for C_{60} to estimate the required sensitivity improvements and evaluate the practicality of C_{60} spectroscopy through this approach.

4.2 First-Generation Source Design and Testing

A block diagram of the first-generation source is shown in Fig. 1. The design is centered around the heated extraction chamber (Fig. 2), a high-pressure 1" steel NPT T-pipe. The T-pipe is wrapped in heating tape and insulation, along with a thermocouple for temperature monitoring. The top fitting contains a safety relief valve calibrated to 4000-psi - this fitting can be removed to load the sample and any co-solvent to be added to the CO_2. Once the sample has been loaded and the safety valve replaced, the extraction chamber and pump are flooded with liquid CO_2. The chamber is then brought to the desired operating temperature using the heating tape and a custom-built temperature controller. Once the system is at the desired temperature it can be brought to pressure using the ISCO uL-500 high-pressure syringe pump, shown in Fig. 3. Typically, the syringe pump will need to be run until the piston runs out of travel, shut off from the extraction chamber via the outlet valve, refilled from the liquid CO_2 cylinder, then cycled again to reach the desired pressure of 200 bar.

Once the system is at the desired temperature and pressure, the valve connecting the extraction chamber to the heated nozzle is opened. The supercritical fluid first encounters a 10 micron pinhole (Lenox Laser). The depressurized fluid expands into the custom-made nozzle, seen in Fig. 4, where it is entrained in a secondary expansion of argon through a 150 micron by 12 mm slit nozzle. The entire nozzle assembly is maintained at a constant temperature using a cartridge heater and thermocouple connected to the custom temperature controller.

The first-generation source was tested under a variety of operating conditions. The extraction chamber was only able to reach temperatures of approximately 370 K, limiting the usable toluene fraction considerably. No conditions were found that allowed spectroscopic observations of methylene bromide or pyrene - since solubility data for these molecules in supercritical fluids were limited, it is unclear whether such observations were feasible. However, jet-cooled signals were observed using a D_2O sample, as seen in Fig. 5. These signals persisted for nozzle temperatures ranging from 400 - 500 K and argon backing pressures ranging from 1 - 60 psig. Generally, the observed D_2O signals exceeded the dynamic range of our spectrometer and prevented comparisons between different expansion conditions.

Although the first-generation source showed promise, there were a number of design flaws we sought to address in the design of the second-generation source. Most importantly, the extraction chamber could not be heated sufficiently to allow our desired toluene fraction in the supercritical fluid. Additionally, the use of general-purpose fittings rather than fittings specifically designed for high-pressure applications caused a number of issues. General-purpose Swagelok fittings performed well initially, but began to leak over time. The teflon tape used for NPT fittings appeared to work initially, but in retrospect we believe the

fittings had to be over-tightened to the point of forming an interference fit before they would hold pressure. Additionally, the teflon tape tended to degrade over time when exposed to supercritical CO_2 and may have contributed to the various clogs experienced while operating the source. Finally, the design of the source allowed temperature gradients to form and thus may have allowed the formation of multiple phases. The lack of any sort of viewing window made it difficult to monitor this.

4.3 Second-Generation Source Design and Testing

A second-generation source was later designed to address these shortcomings; a block diagram of this source is shown in Fig. 6. Unlike the previous source, this iteration included a custom-made extraction chamber, as seen in Fig. 7. The chamber was machined from a 2" by 2" by 5" piece of stainless steel; a 1" diameter bore through the center of the device serves as the supercritical fluid reservoir. The ends of the bore terminate in 1" NPT-F fittings, one of which is used for a high-pressure sight glass used to monitor the fluid and ensure that a single phase is present. The flat surfaces of the chamber also allow better thermal contact with the two 500 W heating strips used, and as a result the chamber can easily reach temperatures in excess of 500 K. In addition, the extraction chamber was placed inside the vacuum chamber to allow better temperature control and decrease the distance between the extraction chamber and the nozzle, both of which serve to limit the formation of temperature gradients. Additional 1/4" NPT-F fittings were included for connections to other parts of the source. Unlike the previous iteration, a thermocouple is inserted into the supercritical fluid to monitor its temperature directly. Additionally, a USB webcam was included in the initial design to monitor the sight glass, but the device failed to function properly under vacuum. The sight glass can still be easily monitored by eye.

In addition to the redesigned extraction chamber, the pipe and tube fittings were changed to types specifically designed for work at high pressures. Swagelok fittings were replaced by taper seal fittings (High Pressure Equipment Company), which are rated to 15,000 PSI and can be reassembled indefinitely without losing seal integrity. Most NPT parts were also replaced with high-pressure variants, and Loctite 5770 high-temperature thread sealant was used in place of teflon tape. The thread sealant does gradually degrade during operation of the source, but appears to last for weeks before needing replacement and does not seem to cause clogging as did the teflon tape.

The same syringe pump, safety valve, and nozzle assembly were re-used for this iteration of the source. The safety valve is located outside of the vacuum chamber to avoid stressing the vacuum pump if it should be triggered. The nozzle assembly is now connected to a high-pressure right angle valve (High Pressure

Equipment Company); while the valve itself is inside the vacuum chamber, the handle has been extended to reach outside the chamber to allow the valve to be easily actuated. At present the nozzle assembly does not have independent heating or temperature monitoring as did the previous source, but these could easily be added back if needed. Likewise, the heating of the extraction chamber is currently controlled by variac rather than a temperature controller for simplicity.

This second-generation source has been successfully assembled and brought to operating temperatures and pressures, and is currently being tested for spectroscopic performance. 1,3,5-trioxane is being used as the sample to allow evaluation of vibrational and rotational cooling performance. Once the cooling performance of the second-generation source under various operating conditions has been established, the mass flow of C_{60} will be evaluated by replacing the slit of the nozzle assembly with CF flange blank and measuring the accumulation of C_{60} after a set run time. These data should allow a decision to be made regarding the feasibility of a C_{60} detection prior to efforts to improve the sensitivity of the spectrometer.

4.4 Results and Discussion

Although spectroscopic observations were attempted using pyrene and methylene bromide for the first-generation source, only D_2O produced an observable signal. It is unclear whether the failure to detect pyrene and methylene bromide resulted from poor solubility in the solvent systems chosen or from some other issue with the operation of the first-generation source. However, the D_2O observations do allow some statements to be made regarding the performance of the source.

The D_2O transition observed was the $1_{11} \leftarrow 0_{00}$ transition of the $010 \leftarrow 000$ vibrational band. A low-intensity, broad peak was observed when the argon backing gas was turned off, indicating high-temperature gas was present outside of the expansion; with the argon backing gas turned on, the signal was consistent with a more intense, narrow jet-cooled signal superimposed over the background gas signal, as shown in Fig. 5. The narrower linewidth is indicative of translational cooling, while the increased intensity is indicative of rotational or vibrational cooling. Because the jet-cooled signal was so intense as to exceed the dynamic range of our spectrometer, it was not possible to evaluate the effects of different operating conditions for the supercritical fluid source. In addition to the observations of the $1_{11} \leftarrow 0_{00}$, other ro-vibrational transitions were investigated. Most notably, we were able to observe the $1_{10} \leftarrow 1_{01}$ transition but not the $2_{21} \leftarrow 3_{12}$ transition. This is indicative of rotational cooling within the expansion. If we assume that the $2_{21} \leftarrow 3_{12}$ signal was present at the level of our noise equivalent absorption at the time, we can estimate a rotational temperature within the expansion of 16 K; in reality the temperature is likely lower, but this provides a

useful upper bound and is a promising indicator of the source's performance.

The modifications made during the design of the second-generation source significantly improved the range of operating conditions available and the reliability of the source. Most importantly, the extraction chamber can now be heated to temperatures well in excess of those needed for a 7:3 CO_2:toluene fluid composition - we have measured fluid temperatures in excess of 500 K. This measurement was obtained well below the maximum power of the 500 W heaters, but the heating was stopped due to the presence of smoke in the chamber. It is believed that this smoke came from the thread sealant used; although the sealant should be stable at 500 K, it is likely that the body of the source was significantly hotter than the supercritical fluid at the time due to slow thermal diffusion. In addition to the superior heating performance, the high pressure fittings used have significantly reduced the occurrence of leaks in the system. We note, however, that the taper fittings used are more prone to cross-threading and cold-welding than the usual Swagelok fittings. It has proven difficult to find a suitable thread sealant for the NPT fittings; the Loctite sealant used performs well initially, but slow leaks tend to develop within a few weeks of exposing the seals to the supercritical fluid. The longevity of these seals is not ideal, but it is sufficient to allow use of the source. The high pressure sight glass has proven effective for monitoring the transition from liquid to supercritical fluid.

Evaluation of the spectroscopic performance of the second-generation source is ongoing. We have been attempting to observe the Q branches of the ν_{16} band of 1,3,5-trioxane in order to evaluate the rotational and vibrational cooling performance of the source. Thus far, we have successfully observed jet-cooled R branch lines, as seen in Fig. 8, but these observations have been inconsistent. No Q branch lines have been observed, despite their greater expected intensity. We suspect that the lack of successful observations result from some intermittent issue with the source, but we have not yet been able to identify the problem. The R branch lines observed have widths similar to those observed with a more traditional supersonic expansion with a rotational temperature of approximately 15 K, but because they are not well resolved we are unable to perform a Boltzmann analysis. A more thorough evaluation of the cooling performance of the source will need to be completed once well-resolved Q or R branch lines can be observed.

A measurement of C_{60} mass flow rate has not yet been performed. There should be no significant obstacles to obtaining this measurement, but thus far we have focused our efforts on spectroscopic observations.

4.5 Conclusion

Although the second-generation source is not yet performing consistently, the results obtained so far from both sources are promising. In each case, we have been able to observe ro-vibrational transitions that indicate rotational cooling to temperatures of 16 K or lower. These temperatures are comparable to those achieved through traditional supersonic expansions for the D_2O and 1,3,5-trioxane molecules.

Given the difficulty of cooling C_{60} in a supersonic expansion, the possibility of producing C_{60} vapor at a lower initial temperature while maintaining similar cooling efficiency should result in significantly more ground-state C_60 available for spectroscopic interrogation. Although we have not yet quantified the solubility of C_{60} in our solvent systems or its mass flow from our supercritical fluid source, its solubility in supercritical fluids has been studied (reference) and we have been able to confirm that C_{60} reaches the secondary argon expansion of our source when using a CO_2 / toluene solvent system.

These results suggest that the observation of C_{60} via supercritical fluid expansion remains a valid approach. Given some additional refinement and improvements to instrumental sensitivity, the first observation of C_{60} via infrared absorption spectroscopy may be possible, and the approach should also be valid for other thermally sensitive samples.

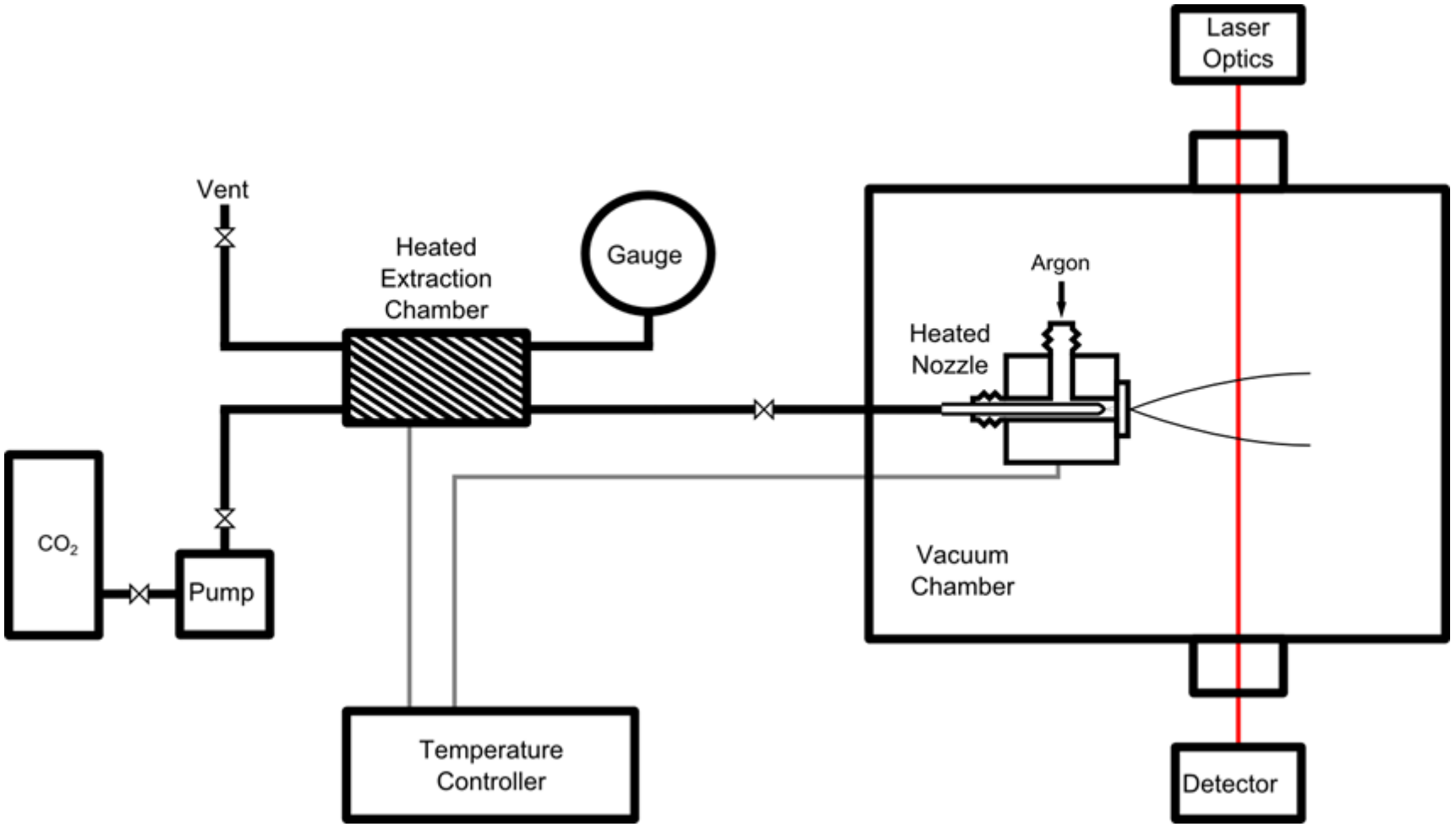

Figure 4.1: Block diagram of the first-generation supercritical fluid expansion source. The sample and any co-solvent are loaded into the heated extraction chamber, which is then flooded with liquid CO_2. The chamber is then heated to the critical temperature using heating tape and pressurized via syringe pump. Once the supercritical fluid is produced, the valve to the heated nozzle is opened and the fluid depressurizes through a ten micron pinhole before being entrained in a secondary argon expansion for spectroscopic interrogation.

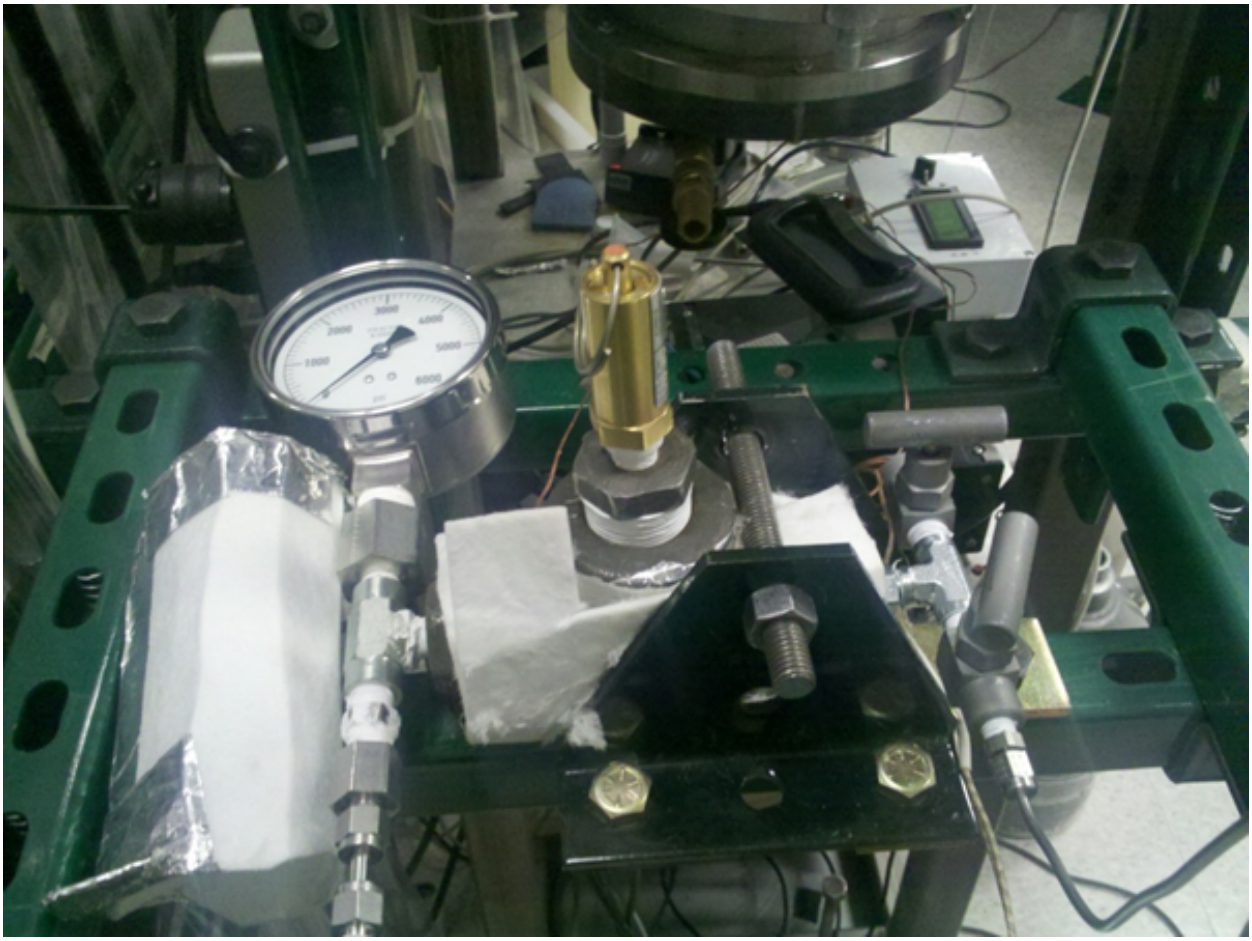

Figure 4.2: First-generation extraction chamber. The body of the chamber is a 1" NPT steel tee, wrapped in heating tape and insulation. When in use, the brass safety relief valve was also covered with insulation.

Figure 4.3: High-pressure syringe pump. Both the first- and second-generation sources used the same ISCO uL500 high-pressure syringe pump. The pump is capable of reaching pressures well in excess of those used in the source.

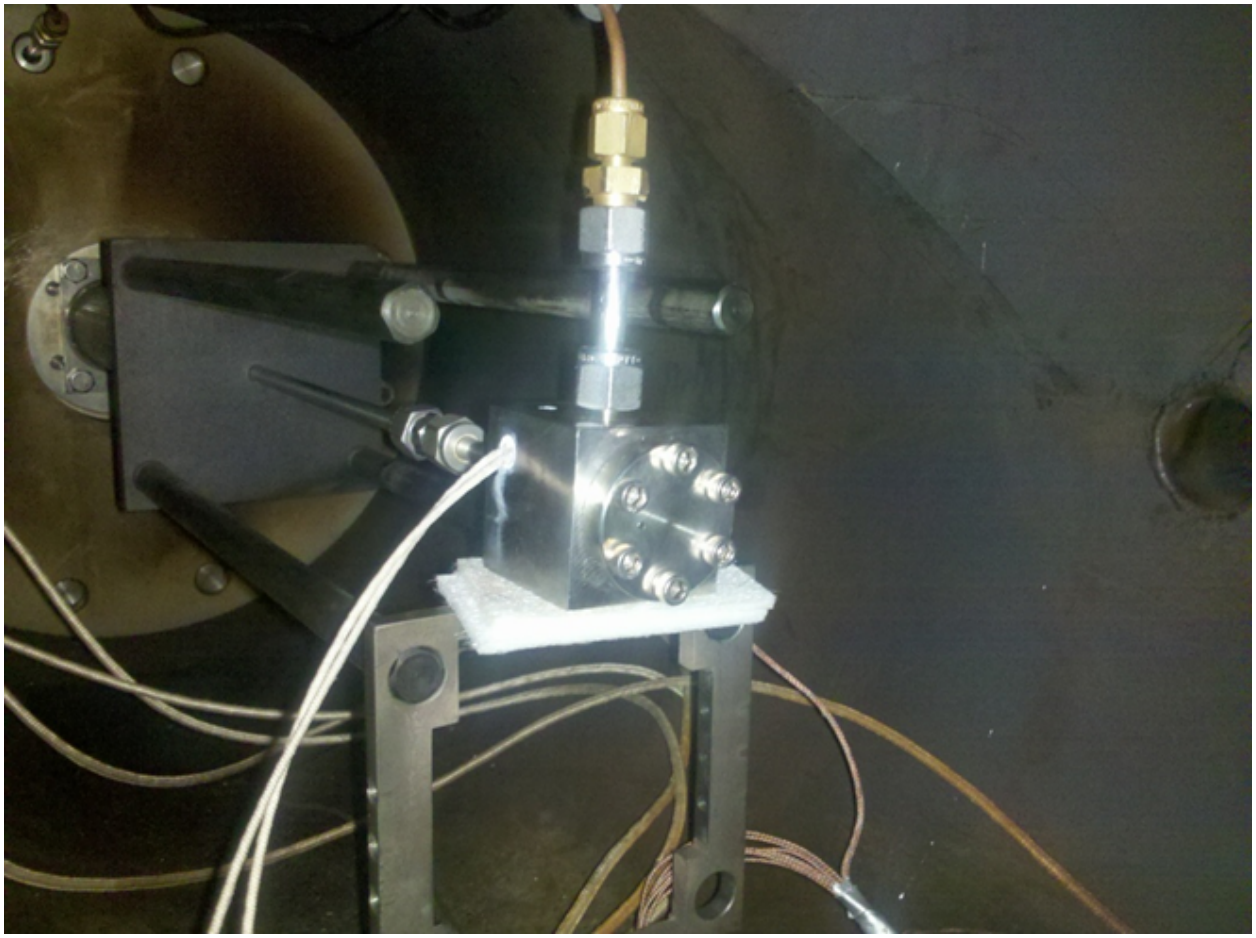

Figure 4.4: Supercritical fluid expansion nozzle. Both the first- and second-generation sources used the same custom expansion nozzle, although the cartridge heater and thermocouple used for independent temperature control in the first-generation source are not present in the second. Not clearly visible is the interior ten micron pinhole used to depressurize the sueprcritical fluid prior to its entrainment in the argon expansion.

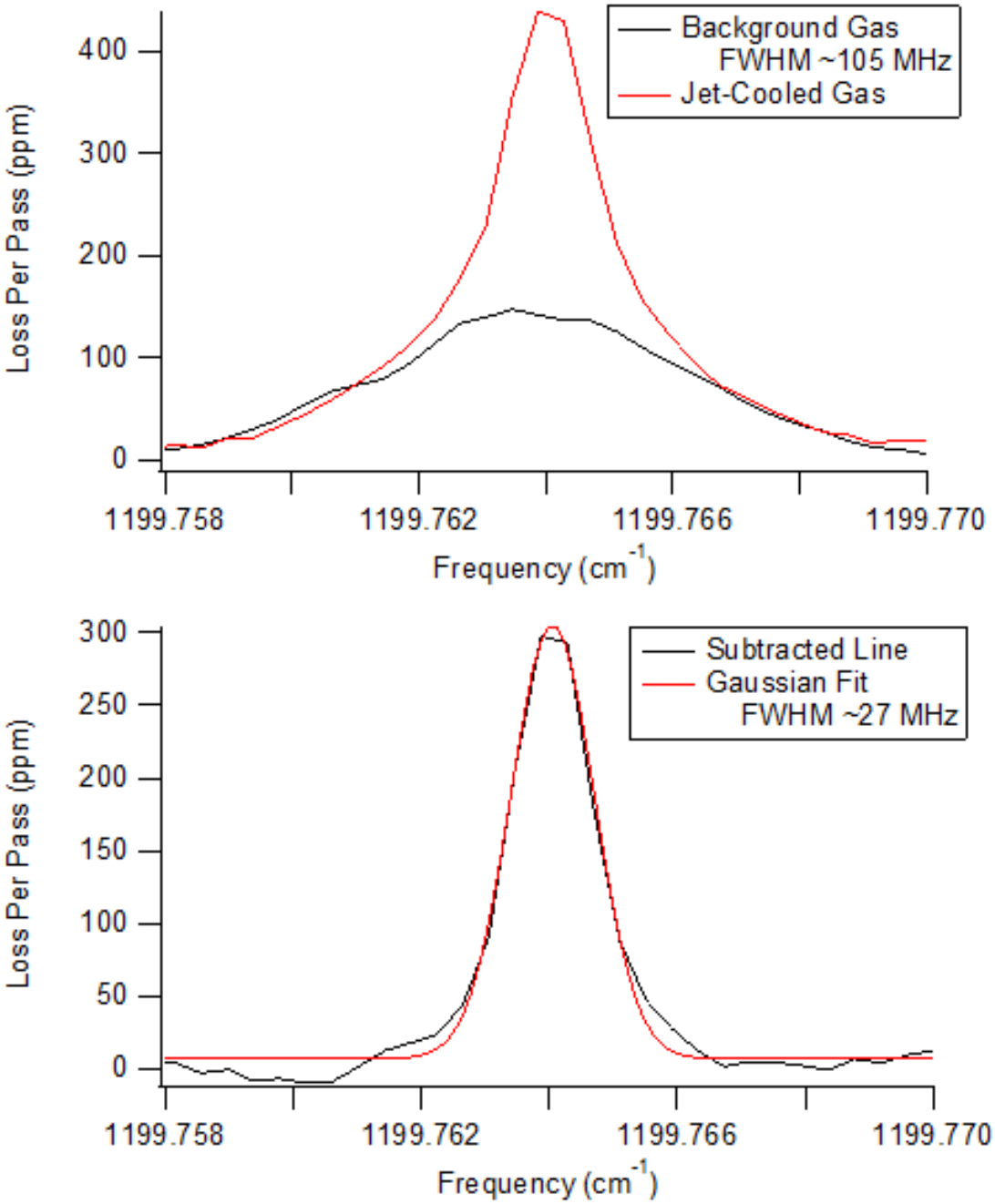

Figure 4.5: D_2O observations using the first-generation supercritical fluid expansion source. In the top plot, the black trace shows the $1_{11} \leftarrow 0_{00}$ transition of the $010 \leftarrow 000$ of D_2O while the argon backing gas is turned off; this is indicative of room-temperature background gas in the chamber. The red trace shows the same transition with the argon backing gas on, showing a narrower jet-cooled feature superimposed over the broad room-temperature signal. The lower plot shows the subtraction of the room-temperature signal from the jet-cooled signal - this shows a gaussian jet-cooled component with a full-width half-max of 27 MHz.

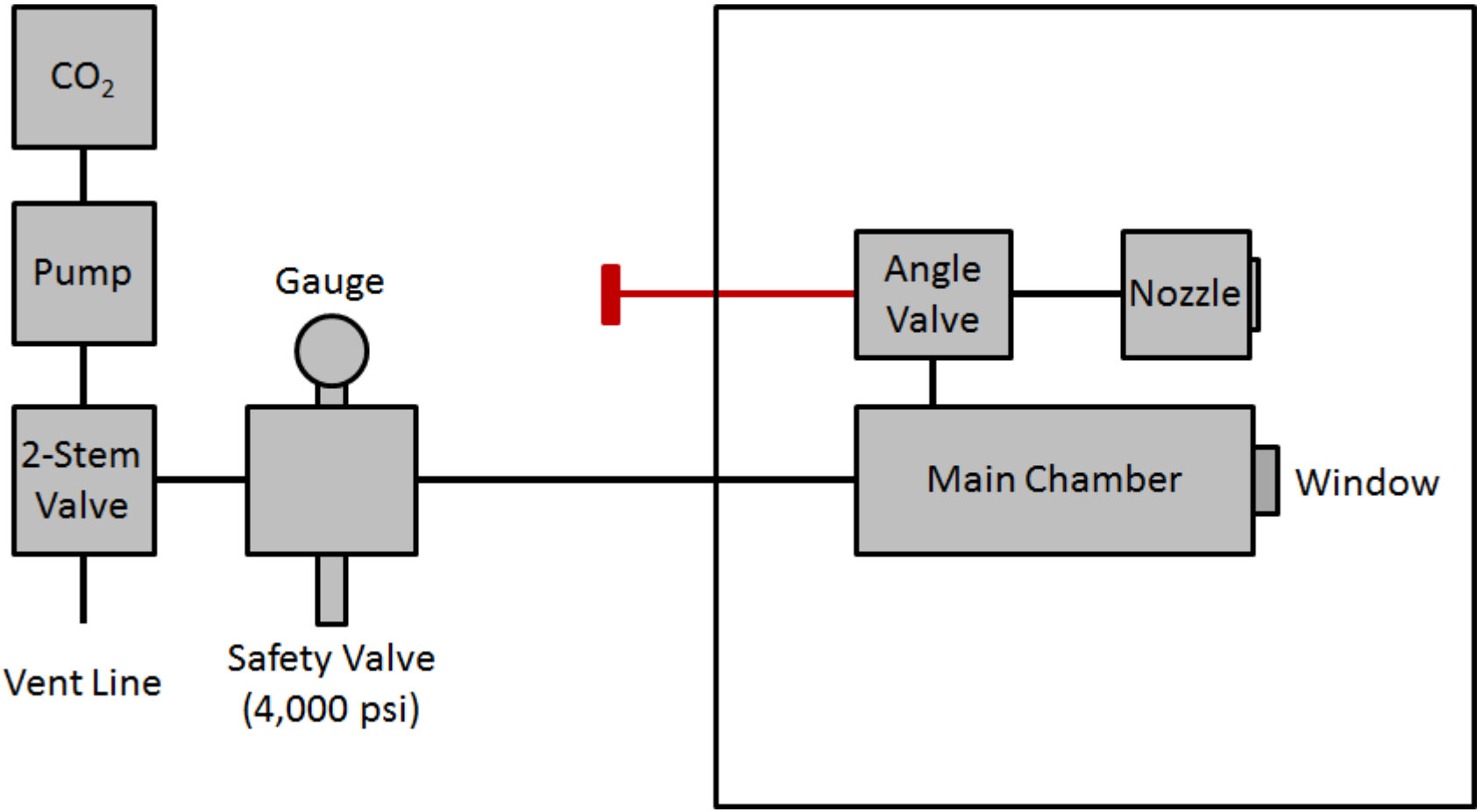

Figure 4.6: Block diagram of the second-generation supercritical fluid source. The most notable difference is that the re-designed custom extraction chamber has been moved into the vacuum chamber - this reduces the need for insulation, and the proximity to the nozzle limits the formation of thermal gradients. The valve between the extraction chamber and nozzle is operated by an elongated stem extending outside of the vacuum chamber to allow easy operation. Additionally, a high-pressure window has been added to the main chamber to allow monitoring of phase changes.

Figure 4.7: Second-generation extraction chamber. It includes new 500 W heating strips to ensure the necessary temperatures for a toluene-containing fluid can be reached. Aslo visible are the new sight glass and a steel-jacketed thermocouple extending into the body of the chamber to allow direct monitoring of the supercritical fluid temperature.

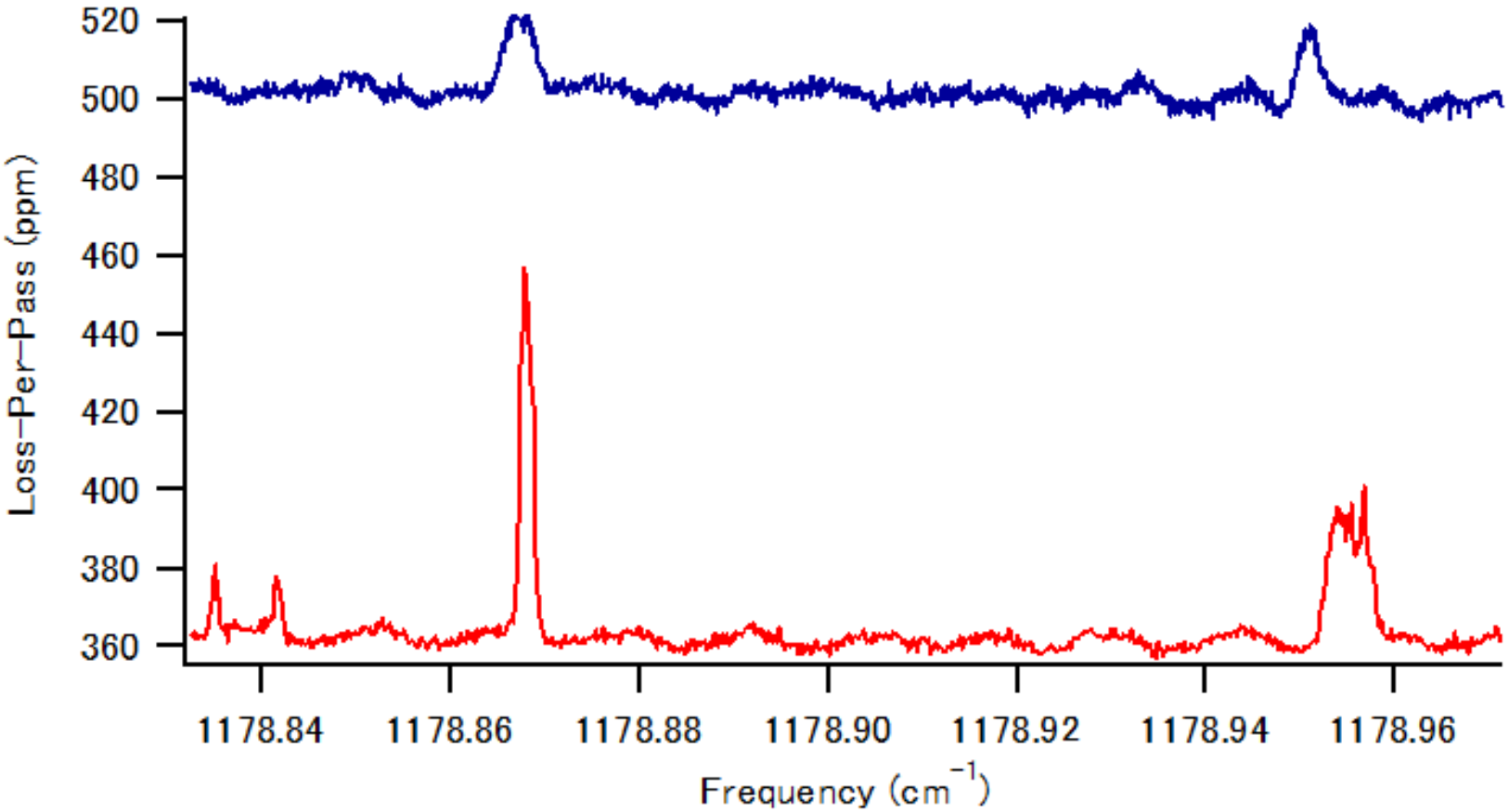

Figure 4.8: Early trioxane observations in the second-generation source. The red trace shows a number of overlapping R branch lines observed during earlier spectroscopy of 1,3,5-trioxane using a traditional supersonic expansion of initially room-temperature gas [31]; the blue trace shows the same region of the trioxane spectrum as seen from the second-generation supercritical fluid expansion source. The observation of these lines without large numbers of additional lines from room-temperature trioxane is indicative of vibrational cooling, but the vibrational temperature cannot readily be estimated from this spectrum.

Chapter 5

Mirrored-Piezo Phase Modulation in the RF

5.1 Introduction

Although the use of a supercritical fluid expansion source re-opens the possibility of obtaining an infrared absorption spectrum of C_{60}, the reduced mass flow relative to the traditional thermal vaporization method may prove problematic. Experimental measurements for the supercritical fluid source are not yet available, but we have estimated that the amount of C_{60} vapor produced will be a factor of twenty lower than the previous oven source [13]. While the lower vibrational temperature expected should more than compensate for this difference in vapor production, improvements to the sensitivity of our instrument will likely be necessary.

The cavity ringdown technique currently utilized is one of the most sensitive techniques available for absorption spectroscopy; the only approach that has been shown to be more sensitive is the noise immune cavity enhanced optical heterodyne spectroscopy (NICE-OHMS) technique developed by Ye and coworkers [44]. Therefore, our only viable approaches are to implement an improved cavity ringdown approach or to build a NICE-OHMS spectrometer. Improving our cavity ringdown spectrometer would require either increasing the signal-to-noise ratio of our recorded ringdown transients or increasing the number of transients recorded within a given time period. The latter approach is likely impractical - detectors and cavity mirrors superior to those currently in use are not commercially available in our spectral region, and these are the limiting factors for the signal-to-noise ratio of a single transient in our instrument. Increasing the number of transients per second is a much more reasonable approach. At present, we simply dither the ringdown cavity by more than one free spectral range using a piezoelectric transducer, ensuring the cavity will be on resonance twice per cycle. In practice, the TEM_{00} mode of the cavity does not build up sufficient power to record a ringdown transient with every pass. A slower sweep of the piezoelectric transducer increases the likelihood of building up enough power, so the ideal sweep rate to maximize the number of ringdown events per second must be optimized from day to day based upon laser power and laboratory conditions. A typical value for our instrument is 100 ringdown events per second. A more efficient approach referred to as high repetition rate

ringdown involves locking the laser to the ringdown cavity to ensure it is always on resonance; instruments utilizing this approach can collect as many as 10,000 ringdown transients per second [45]. This is typically achieved through the Pound-Drever-Hall locking technique [46], which requires the addition of sidebands to the carrier laser frequency through frequency modulation. This approach would allow us to improve the sensitivity of our instrument by approximately an order of magnitude to $10^{-10}\text{cm}^{-1}\text{Hz}^{-1/2}$. The alternative approach of implementing NICE-OHMS detection has been done successfully with a quantum cascade laser in a similar wavelength region [47]; although NICE-OHMS has been shown to have a sensitivity as low as $10^{-14}\text{cm}^{-1}\text{Hz}^{-1/2}$ in some wavelength regions, previous attempts with mid-infrared quantum cascade lasers have only demonstrated sensitivies of $10^{-10}\text{cm}^{-1}\text{Hz}^{-1/2}$ [44, 47]. Because the NICE-OHMS approach would be significantly more complicated and expensive, it seems likely that high repetition rate ringdown is the more practical approach.

Regardless of which approach is chosen, the production of sidebands through frequency modulation will be a key step. In most wavelength regions, this is done using an electro-optic modulator. In the thermal infrared, however, commercial modulators are not available. Custom modulators have been built [48], but the depth of modulation is relatively low at high modulation frequencies and the materials used are quite expensive. Another possible approach is to use multiple acousto-optic modulators - this approach should be effective with commercially available devices, but purchasing multiple modulators and drivers would also be costly. The quantum cascade laser NICE-OHMS implementation [47] mentioned previously used injection current modulation of the laser to add sidebands - again, this approach should be practical, but would require careful design to keep the high-frequency modulation from interfering with other electronics in the instrument. Additionally, injection current modulation of quantum cascade lasers can cause significant amplitude modulation in addition to frequency modulation, which is undesirable for both spectroscopic approaches under consideration [49].

Another possible method for adding sidebands is to phase modulate the laser by directly altering the laser's path length at high frequencies using piezoelectric transducers. The simplest method for doing so is to place a mirror on one face of the transducer and reflect the laser from this mirror either at a small angle or in a retroreflector configuration, as shown in Fig. 1. The position of the mirror changes over the course of the sweep of the piezoelectric transducer, changing the distance traveled by the laser and inducing phase modulation at the sweep frequency of the transducer. This approach has been successfully implemented in the past at frequencies of up to 125 kHz [50]. The transducer was used was a commercially available PZT stack; the device was operated at mechanical resonance frequencies, and because of the low mechanical quality factor of the transducer and the weight of the mirror operation at higher resonances did

not provide a useful displacement of the mirror. The modulation frequency achieved in this study would likely be insufficient for Pound-Drever-Hall locking, and is orders of magnitude slower than would be needed for NICE-OHMS.

In principle, there is no reason a piezoelectric modulator capable of operation at higher frequencies could not be designed. Quartz resonators operating at frequencies of hundreds of MHz are commonly used as clocks in modern electronics; these devices typically use a crystal orientation that produces a shear motion, but the X-cut crystal orientation can be used to produce linear motion in the direction of the voltage gradient. Using a single high-quality crystal rather than a stack of PZT transducers would increase the mechanical quality factor, and thus the displacement for a given voltage, by several orders of magnitude. Furthermore, by simply using a high-quality gold coating as the front electrode it is possible to reflect a laser directly off of the surface of the transducer rather than adding a much heavier mirror and slowing the achievable modulation frequency. We have designed a mirrored piezoelectric phase modulator based upon these principles, and at the time of writing we are finishing the final steps of its fabrication in preparation for characterizing its performance. Should the device perform up to our expectations, it would provide an inexpensive and wavelength-independent technique for phase modulation of any type of laser and enable significant improvements to our ringdown spectrometer.

5.2 Modulator Design

The basic design of the modulator is shown in Fig. 2. The device is built around a 1 mm by 1 mm by 0.5 mm X-cut quartz crystal, with the piezoelectric axis perpendicular to the large facets (i.e., through the gold electrode). The top facet of the crystal was coated with a 10 nm adhesion layer of chromium followed by a 100 nm layer of gold to act as the top electrode and the mirrored surface. The bottom facet of the crystal is attached to a 1 inch by 0.5 inch copper mounting slide using indium solder; in addition to providing support, the copper slide acts as the back electrode. Two additional copper pads are attached to the backing slide with thin double-sided tape - these are connected to the gold top electrode of the crystal with gold wiring and act as electrical contacts for the top electrode.

Quartz was selected primarily due to its extremely large mechanical quality factor, Q. The displacement for an X-cut quartz piezoelectric transducer operated off resonance is given by the simple formula

$$\text{Displacement} = d_{33}V \tag{5.1}$$

where d_{33} is the piezoelectric charge constant along the relevant axis in units of C/N and V is the voltage

applied along that axis. When operated on resonance, the displacement is given by

$$\text{Displacement} = \frac{Qd_{33}V}{(n\pi)^2} \tag{5.2}$$

where n is the resonance number (first resonance, second harmonic, etc). For an X-cut quartz crystal, Q is typically on the order of 200,000 while d_{33} is $\times 10^{-12}$C/N. The resonance frequency of a piezoelectric transducer is given by

$$\text{Displacement} = \frac{N_T}{l} \tag{5.3}$$

where N_T is the thickness mode frequency constant and l is the thickness of the device. X-cut quartz has a frequency constant of 2,865 m/s; for a device with a thickness of 0.5 mm, this yields a resonance frequency of 5.73 MHz. This is, of course, only an estimate of the resonance frequency of the finished device - the addition of electrodes and mounting hardware will have a significant effect on the resonance frequency that cannot be easily calculated. As such, this number is used for calculations moving forward but the actual resonance frequency will need to be determined empirically for the finished device.

The other considerations in selecting the piezoelectric material were fracture strength and power dissipation. For quartz, fracture strength is approximately 145 MPa [51]; because there is significant variation in this value from sample to sample, a typical safe design stress is approximately 20 MPa. Displacements, stresses and strains were calculated for our device and are given in Table 1, assuming a peak-to-peak modulation voltage of 50 V. This voltage would allow safe operation at the ninth harmonic, which would provide a modulation index of slightly below 0.1 at a modulation frequency on the order of 60 MHz, assuming an 8.5 micron carrier wavelength for the laser. Obviously, the voltage could be adjusted to allow safe operation at other harmonics. Assuming a 50 V peak-to-peak voltage, however, we can estimate that our device will dissipate approximately 4 mW of power - this should be quite safe to operate. The remaining concern is the integrity of the indium solder while the device is in operation - while indium is known to bond reasonably well to quartz, this joint seems to be the most likely mode of failure for these devices.

At the time of writing, fabrication of these devices is nearly complete - only the gold wiring connecting the gold electrode to the copper contact pads needs to be completed. The quartz modulators are shown in Fig. 3.

In addition to the modulators themselves, we have designed a custom mounting adapter to allow the modulators to be placed in standard kinematic mirror mounts. Electrical contact with the copper mounting slide and the copper pads is made using standard machine screws, to which ring terminals can easily be

attached. Given the relatively low voltage being used at this stage, no additional safeguards have been added to avoid accidental contact with the electrodes - if higher modulation voltages are used in the future, an alternate design may be necessary.

5.3 Device Characterization

Since the use of piezo-actuated mirrors for phase modulation has already been demonstrated at lower frequencies [50], we are primarily concerned with identifying the resonance frequency of our devices and showing that they can be operated at frequencies and voltages appropriate for Pound-Drever-Hall locking and potentially NICE-OHMS. Pound-Drever-Hall locking can be performed with modulation frequencies of a few MHz, whereas NICE-OHMS requires modulation at frequencies corresponding to the free spectral range of the optical cavity being used - for cavity lengths on the order of one meter, this requires modulation frequencies of over 100 MHz.

Resonance frequencies can be determined by observing the impedance of a circuit containing the piezoelectric transducer as a function of frequency. Points of minimum impedance correspond to electrical resonance frequencies, while points of maximum impedance correspond to electrical antiresonance frequencies. The maximum displacement of the transducer for a given voltage will be found between these two frequencies. In general additional resonances should be found at harmonics of the first resonance, but more than one resonance mode may be present; these may produce more complicated motions than the thickness mode resonance, but in principle may be useful if they produce a large enough modulation index at some desirable frequency.

Following the completion of device fabrication, these resonance frequencies will be determined by operating the devices at low voltages and monitoring the current with a Hall effect sensor. Once the resonance frequencies have been identified, we will attempt to operate the devices at voltages and frequencies appropriate to produce modulation indices of 0.1 at resonances near 10 and 100 MHz to determine whether or not they will encounter mechanical failures. We anticipate that the devices should function well at 10 MHz, but their performance at 100 MHz is uncertain.

5.4 Conclusion

Phase modulation via a mirrored piezoelectric transducer seems like a promising approach for the addition of sidebands to our laser. This technique is particularly useful in the thermal infrared since electro-optic modulators are not readily available, but it should be useful in other wavelength regions as well if sufficient

modulation bandwidth can be achieved - since the technique has already been demonstrated at low modulation frequencies, only the modulation bandwidth remains to be proven. The materials used are readily available and inexpensive, making it a cheaper alternative even if commercial modulators are available.

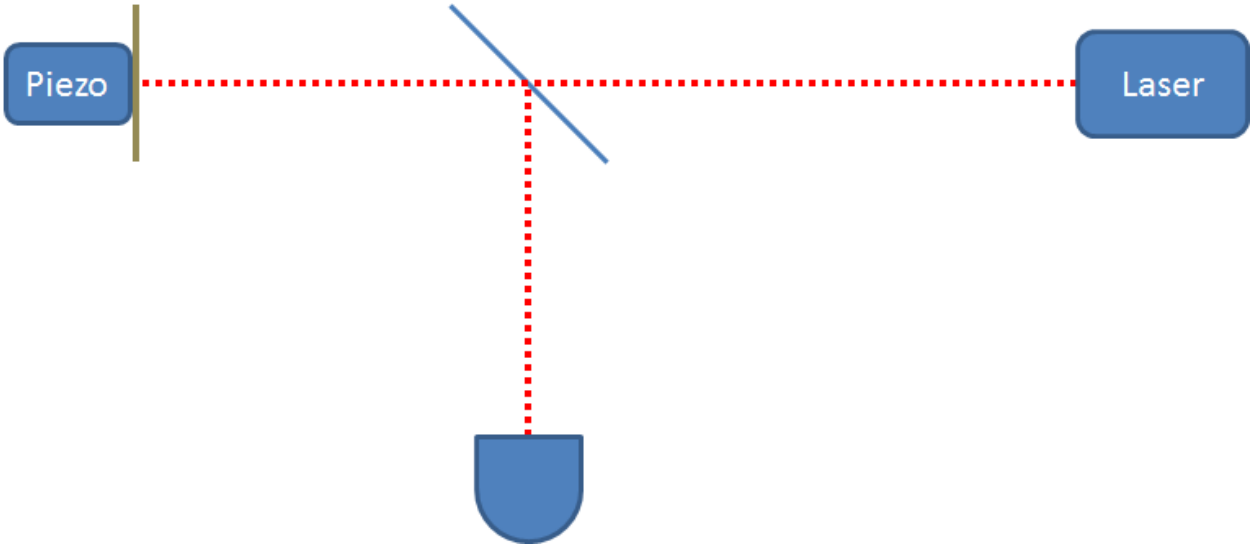

Figure 5.1: Retroreflector configuration for mirrored-piezo phase modulation. In this configuration, a mirror displacement of X will lead to a path length change for the laser of $2X$; if the mirror displacement is rapidly modulated, this will lead to phase modulation of the retroreflected beam.

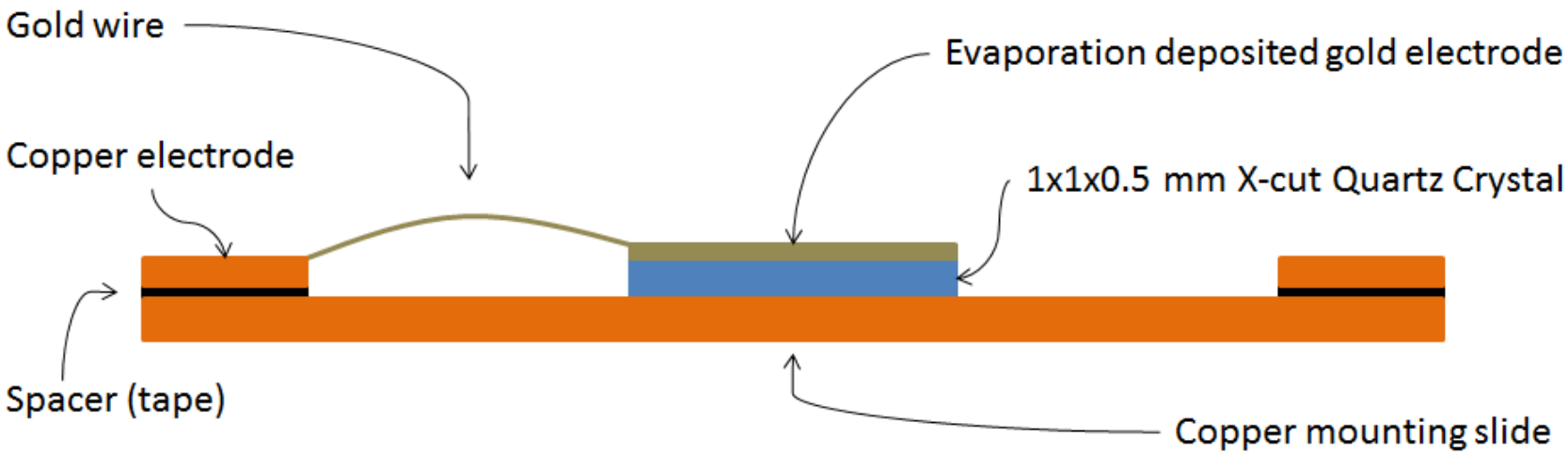

Figure 5.2: Mirrored-piezo modulator design. The modulator is built around a $1 \times 1 \times 0.5$ mm X-cut quartz crystal. The top facet of the crystal is coated with gold, which acts both as the top electrode and the mirrored surface. The quartz crystal is attached to a copper support and bottom electrode using an indium solder. The mirrored surface is attached to copper pads with gold wiring to allow easier contact with the driver without compromising the mirrored surface.

Table 5.1: Listing of mechanical characteristics for the quartz piezo at increasing resonances. The total displacement, strain and stress values are given for the $1 \times 1 \times 0.5$ x-cut quartz modulator at increasing resonance frequencies, assuming a drive voltage of 50 V p-p. The fracture strength for quartz is approximately 145 MPa, indicating that the device would likely fail at this voltage for lower resonances but perform well at higher resonances.

Resonance	Displacement (μm)	Strain (%)	Stress (MPa)
1	9.321	1.864	1864.310
3	1.036	0.207	207.146
5	0.373	0.0746	74.574
7	0.190	0.0380	38.047
9	0.115	0.0230	23.016
11	0.0770	0.0154	15.408
13	0.0552	0.0110	11.031
15	0.0414	0.00829	8.286
17	0.0323	0.00645	6.45
19	0.0258	0.00516	5.164
21	0.0211	0.00423	4.227
23	0.0176	0.00352	3.524
25	0.0149	0.00298	2.983
27	0.0128	0.00256	2.557
29	0.0111	0.00222	2.217
31	0.00970	0.00194	1.940

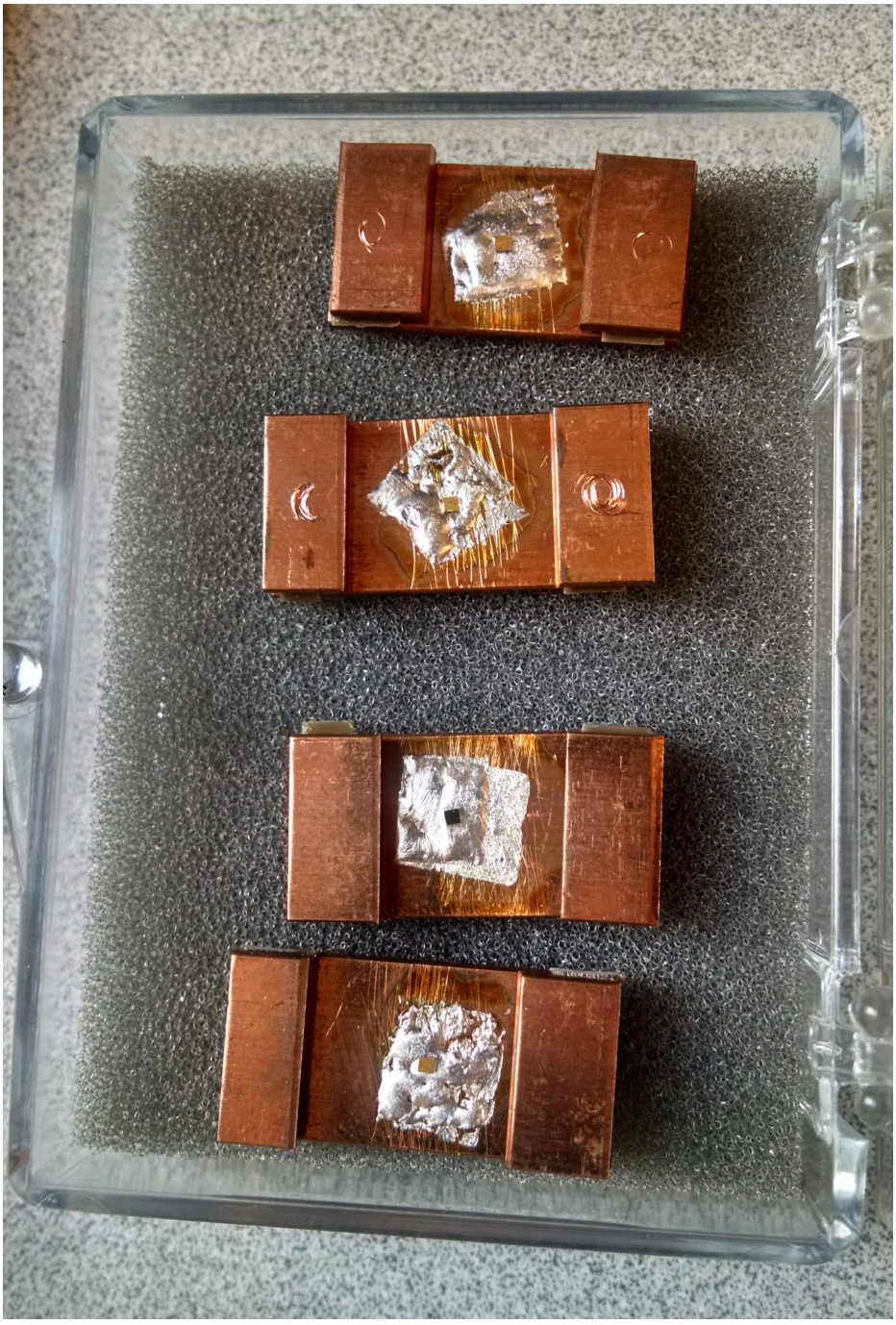

Figure 5.3: Prototype quartz modulators. The small gold surface in the middle of each modulator is the top electrode of the quartz piezoelectric modulator. Note that, at the time of writing, the gold wiring between the gold electrode and the copper pads is absent.

Appendix A

Spectral Simulations of C_{60} and Other Potential Targets

I. The Rigid-Rotor Approximation

The rotational energy of molecules can be approximated by treating them as rigid bodies. In the simplest case, consider the rotation of a diatomic molecule consisting of two atoms of mass m_1 and m_2 displaced from the center of mass by r_1 and r_2, aligned along the x-axis. Rotation about the x-axis carries no kinetic energy; rotations about the y- and z-axes are equivalent. If the particle is rotating at a frequency of ν_{rot}, then the velocities of the atoms are $v_1 = 2\pi r_1 \nu_{rot}$ and $v_2 = 2\pi r_2 \nu_{rot}$, giving a total kinetic energy of

$$K = \frac{1}{2} m_1 v_1^2 + \frac{1}{2} m_2 v_2^2 = \frac{1}{2} \left(m_1 r_1^2 + m_2 r_2^2 \right) \omega^2 = \frac{1}{2} I \, \omega^2 = \frac{L^2}{2\mathrm{I}} \quad ,$$

where L is the angular momentum and I is the moment of inertia. More generally,

$$E = \frac{L_x^2}{2\mathrm{I}_x} + \frac{L_y^2}{2\mathrm{I}_y} + \frac{L_z^2}{2\mathrm{I}_z} = \frac{L_A^2}{2\mathrm{I}_A} + \frac{L_B^2}{2\mathrm{I}_B} + \frac{L_C^2}{2\mathrm{I}_C} \quad ,$$

where by convention the moments of inertia are defined such that

$$I_A \le I_B \le I_C \quad .$$

The kinetic energy operator can also be written as

$$\hat{K} = \hat{H} = \frac{-\hbar^2}{(2\mu)} \nabla^2 \quad ,$$

where, for a constant r, ∇^2 is

$$\nabla^2 = \frac{1}{r^2} \frac{1}{\sin\theta} \left(\sin\theta \frac{\partial}{\partial \theta} \right) + \frac{1}{r^2} \frac{1}{\sin^2\theta} \frac{\partial^2}{\partial \phi^2} \quad .$$

The Hamiltonian can then be rewritten as

$$\hat{H} = \frac{-\hbar^2}{2\mathrm{I}} \left[\frac{1}{\sin\theta} \frac{\partial}{\partial \theta} \left(\sin\theta \frac{\partial}{\partial \theta} \right) + \frac{1}{\sin^2\theta} \left(\frac{\partial^2}{\partial \phi^2} \right) \right] \quad ,$$

and

$$\hat{L^2} = -\hbar^2[\frac{1}{\sin\theta}\frac{\partial}{\partial\theta}(\sin\theta\frac{\partial}{\partial\theta}) + \frac{1}{\sin^2\theta}(\frac{\partial^2}{\partial\phi^2})] \quad .$$

For the wave function $Y(\theta,\phi)$,

$$\hat{H}\,Y(\theta,\phi) = E\,Y(\theta,\phi) = \frac{-\hbar^2}{2\mathrm{I}}[\frac{1}{\sin\theta}\frac{\partial}{\partial\theta}(\sin\theta\frac{\partial}{\partial\theta}) + \frac{1}{\sin^2\theta}(\frac{\partial^2}{\partial\phi^2})]Y(\theta,\phi) \quad ,$$

which leads to

$$\sin\theta\frac{\partial}{\partial\theta}(\sin\theta\frac{\partial Y(\theta,\phi)}{\partial\theta}) + \frac{\partial^{2\mathrm{Y}}(\theta,\phi)}{\partial\phi^2} + (\frac{2\mathrm{IE}}{\hbar^2}\sin^2\theta)Y(\theta,\phi) = 0 \quad .$$

The solutions to this equation are the spherical harmonics, which impose the condition that

$$E = \frac{\hbar^2}{2\mathrm{I}}J(J+1) = B\,J(J+1)$$

for integer values of J [1], where B is the rotational constant.

The relations between I_A, I_B and I_C can be used to classify molecules, and lead to different approaches to finding their energy levels. Molecules with two identical moments of inertia are classified as symmetric tops. If $I_\mathrm{B} = I_\mathrm{C}$, the molecule is a prolate top; if $I_\mathrm{A} = I_\mathrm{B}$, the molecule is an oblate top. Bearing in mind that

$$L^2 = L_x^2 + L_y^2 + L_z^2 \quad ,$$

the energy expressions become

$$E = \frac{L_A^2}{2\mathrm{I}_A} + \frac{(L_B^2 + L_C^2)}{2\mathrm{I}_B} = \frac{L^2}{2\mathrm{I}_B} + (\frac{1}{2\mathrm{I}_A} - \frac{1}{2\mathrm{I}_B})L_A^2 \quad \text{(prolate)}$$

and

$$E = \frac{L_C^2}{2\mathrm{I}_C} + \frac{(L_A^2 + L_B^2)}{2\mathrm{I}_A} = \frac{L^2}{2\mathrm{I}_A} + (\frac{1}{2\mathrm{I}_C} - \frac{1}{2\mathrm{I}_A})L_C^2 \quad \text{(oblate).}$$

The energy level expression is similar to that derived for a diatomic molecule, but with an additional quantum number K_A or K_C to address the L_A^2 and L_C^2 terms as well as additional rotational constants A

or *C*. The modified expressions are

$$E = B\,J(J+1) + (A-B)K_A^2 \quad \text{(prolate)}$$

and

$$E = B\,J(J+1) + (C-B)K_C^2 \quad \text{(oblate).}$$

Molecules for which $I_A = I_B = I_C$ are classified as spherical tops. In the rigid-rotor approximation, the energy expression is simply

$$E = \frac{L_A^2}{2I_B} + \frac{L_B^2}{2I_B} + \frac{L_C^2}{2I_B} = \frac{L^2}{2I_B} \quad ,$$

leading to

$$E = B\,J(J+1) \quad .$$

II. Additional Considerations

A. Centrifugal Distortion

In reality, rotating molecules are not totally rigid. During rotation, centrifugal forces alter the internuclear separations, and thus the moments of inertia, of the molecule. For spherical tops, this can be described most simply by the altered energy level equation

$$E = BJ(J+1) - D(J(J+1))^2 \quad ,$$

although higher order terms can be used for a more accurate treatment, as in the equation

$$E = BJ(J+1) - D(J(J+1))^2 + H(J(J+1))^3 + L(J(J+1))^4 + M(J(J+1))^5 + \cdots \quad .$$

For symmetric tops, the modified energy level equations are

$$E = BJ(J+1) - D_J(J(J+1))^2 + (A-B)K^2 - D_K K^4 - D_{JK} J(J+1) K^2 \quad \text{(prolate)}$$

and

$$E = BJ(J+1) - D_J(J(J+1))^2 + (C-B)K^2 - D_K K^4 - D_{JK} J(J+1) K^2 \quad \text{(oblate) [2].}$$

B. Coriolis Coupling

An additional complication arises when dealing with ro-vibrational transitions. In a rotating molecule, it is possible for vibrations to produce angular momentum, thus coupling rotations and vibrations. The effect on the rotational energy levels of spherical tops is described by the equations

$$E = BJ(J+1) + 2\mathrm{B}\zeta(J+1) \quad ,$$

$$E = BJ(J+1) - 2\mathrm{B}\zeta$$

and

$$E = BJ(J+1) - 2\mathrm{B}\zeta(J+1) \quad .$$

For symmetric tops, the equations are

$$E = BJ(J+1) + (A-B)K^2 \mp 2\mathrm{A}\zeta K \quad \text{(prolate)}$$

and

$$E = BJ(J+1) + (C-B)K^2 \mp 2\mathrm{A}\zeta K \quad \text{(oblate) [2].}$$

These corrections can be combined with the centrifugal distortion corrections presented above to give the equations

$$E = BJ(J+1) + 2\mathrm{B}\zeta(J+1) - D(J(J+1))^2 \quad ,$$

$$E = BJ(J+1) - 2\mathrm{B}\zeta - D(J(J+1))^2$$

and

$$E = BJ(J+1) - 2\mathrm{B}\zeta(J+1) - D(J(J+1))^2$$

for spherical top molecules as well as the equations

$$E = BJ(J+1) + (A-B)K^2 \mp 2\mathrm{A}\zeta K - D_J(J(J+1))^2 - D_K K^4 - D_{JK} J(J+1)K^2 \quad \text{(prolate)}$$

and

$$E = BJ(J+1) + (C-B)K^2 \mp 2\mathrm{A}\zeta K - D_J(J(J+1))^2 - D_K K^4 - D_{JK} J(J+1)K^2 \quad \text{(oblate)}$$

for symmetric tops.

C. Asymmetric Tops

Many molecules of potential interest fall under the classification of asymmetric tops, which are somewhat more difficult to address. Unlike symmetric molecules, there may be no obvious choice of axes when dealing with asymmetric tops – nonetheless, for any given molecule there exists some set of axes (referred to as the principal axes) such that ω and L are parallel and the inertia matrix is diagonal [2]. This also provides the principal moments of inertia, which correspond to rotational constants in the usual way. Asymmetric top energy levels must be determined numerically.

III. Simulated Spectra

A. $^{12}C_{60}$

$^{12}C_{60}$ is a spherical top of I_h symmetry consisting of 60 spin-0 bosons. In considering the F_{1u} band centered at 1184 cm^{-1}, the most distinctive features of the spectrum are the missing low-J rotational levels forbidden due to symmetry considerations (Figure 1). Because $^{12}C_{60}$ consists entirely of spin-0 bosons, any permutation of carbon atoms must be symmetric – since in the ground state Ψ_{el}, Ψ_{vib} and Ψ_{ns} are all of A_g symmetry, Ψ_{rot} is also restricted to A_g symmetry. The degeneracy of each rotational level can be determined by decomposing rotational states into the irreducible components of I_h, with the number of A_g components forming a repeating pattern dependent on J [3].

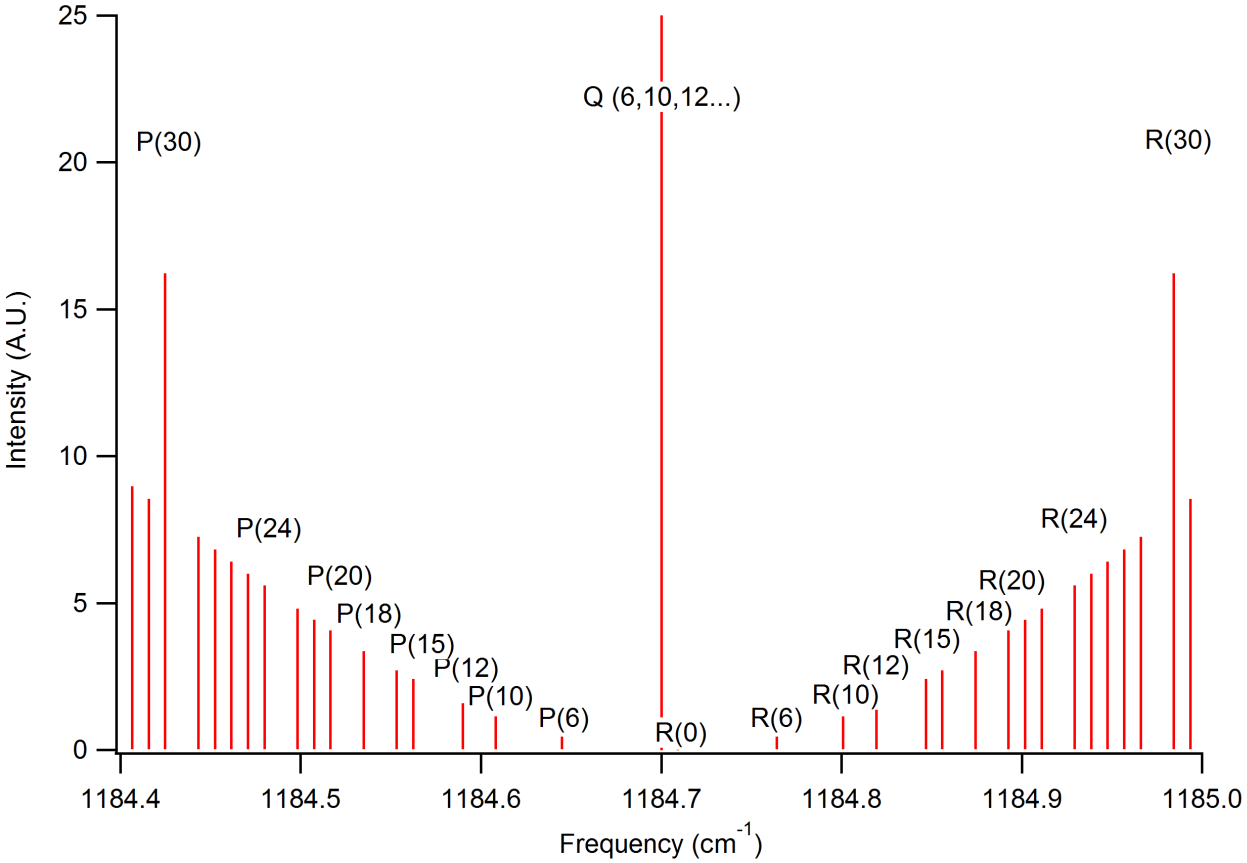

Figure A.1: Simulated stick spectrum for C_{60} showing the various missing rotational levels, assuming $\Delta B = 0$ for clarity. There are no missing levels beyond J = 30, although the rotational degeneracy follows a similar pattern throughout the spectrum.

A number of constants relevant to the ro-vibrational spectrum of C_{60} are currently unknown. In particular, the excited state rotational constant, the Coriolis constant and the integrated absorption strength of the band have not been experimentally determined. It is reasonable to expect a ΔB of 0.1% [4] and a Coriolis constant of $\zeta = -0.319$ [5] – the effects of varying these constants can be seen in Figures 2 and 3, respectively. In general, the change in rotational line spacing with increasing J varies inversely with ΔB, leading to the formation of a strong Q branch head when ΔB is small and an R branch head when ΔB is large. As the Coriolis constant increases, the line spacing for the P and R branches decreases while the Q line spacings are unchanged. Two values have been proposed for the integrated band strength – 27 km/mol from a theoretical DFT study [6] and 10.4 km/mol from an

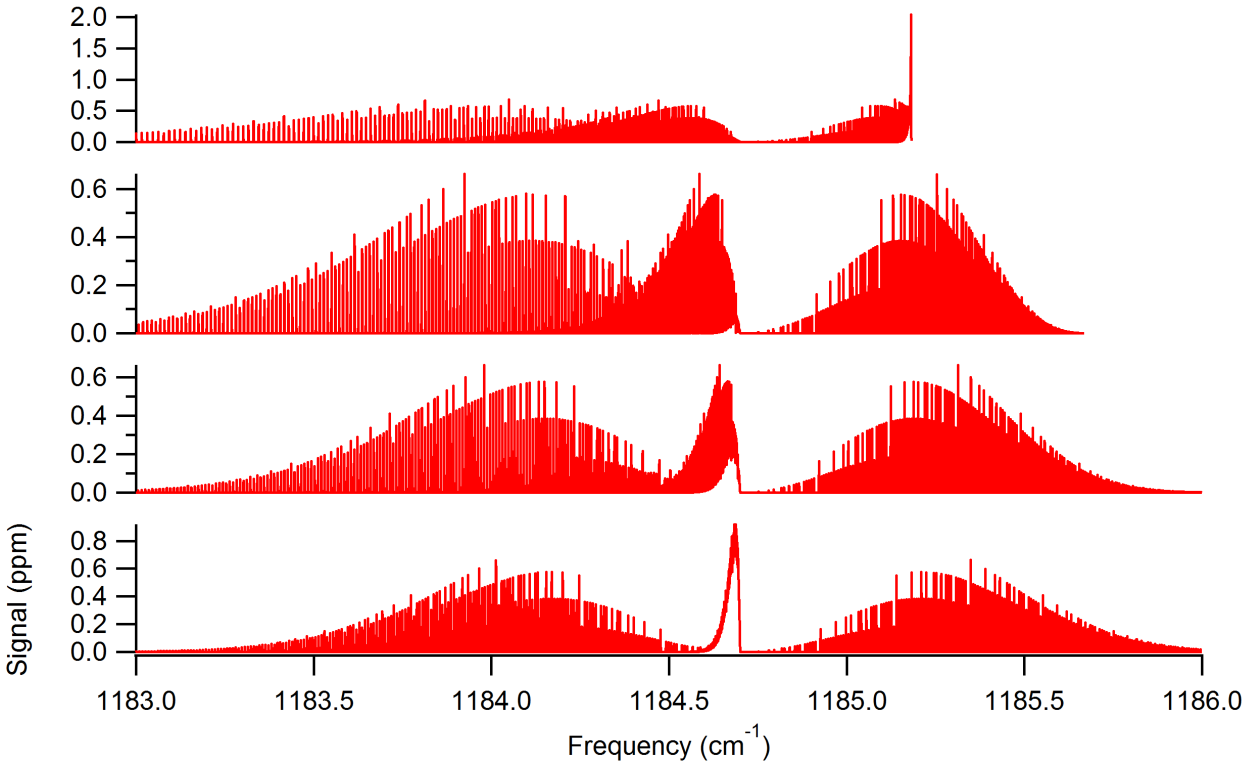

Figure A.2: Simulated spectra of C_{60} showing the effects of decreasing ΔB. From top to bottom, the values of ΔB are 1%, 0.5%, 0.25% and 0.1%. Very high values produce a strong R branch head, while lower values produce a strong Q branch head. The most intense single transitions are found at J = 90. Other parameters are $\Delta\nu = 0.0004$ cm^{-1}, T_{rot} = 20K, T_{vib} = 0K.

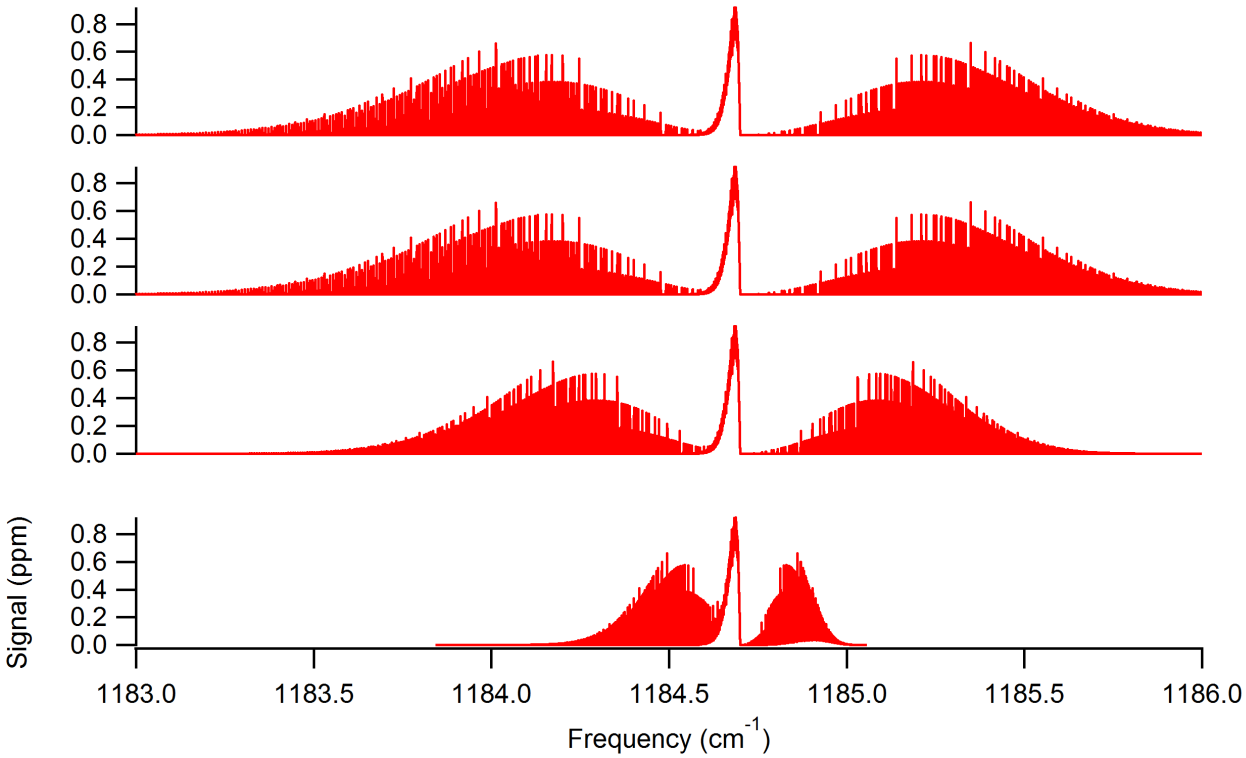

Figure A.3: Simulated spectra showing the effects of the value of the Coriolis constant. From top to bottom, the values are -0.319, -0.16, 0 and 0.319. As the value increases, the spacing between P and R transitions decreases; the Q branch position shifts, but the line spacings are unchanged. This is because each branch of the spectrum of C_{60} comes from a different portion of the degenerate level split by Corriolis coupling – the spacings of the level responsible for the Q branch do not depend upon ζ. Other parameters are $\Delta\nu = 0.0004$ cm^{-1}, $T_{rot} = 20$K, $T_{vib} = 0$K.

experimental KBr matrix study [7]. The latter value was chosen for these simulations to allow a more consistent comparison with $^{12}C_{70}$, which was also studied.

B. $^{12}C_{70}$

$^{12}C_{70}$ is the second most common fullerene, and its spectrum is also of interest. $^{12}C_{70}$ is a symmetric top of D_{5h} symmetry, and also consists entirely of spin-0 bosons. As with C_{60}, this restricts the allowed rotational levels in the ground vibrational state – in this case to levels with A_1 symmetry. This leads to a few missing transitions at $J = 1$ and 2, but the effects of nuclear spin statistics are less pronounced than in C_{60}; again, the degeneracy of each level can be determined by decomposing the rotational states into irreducible representations of D_{5h}.

Although the band strength of the A_2'' band at 1143 cm^{-1} of 9.1 km/mol [7] is comparable to that of the C_{60} band considered above, the strongest transition of C_{70} is weaker than the strongest C_{60} transition by a factor of ~60 (Figure 4). This is because the integrated band intensity of C_{70} is divided amongst significantly more distinct transitions. This comparison does assume that the two molecules are at identical vibrational temperatures (0 K for these simulations); C_{70} may cool more efficiently due to a slightly greater density of vibrational states at low temperatures [8].

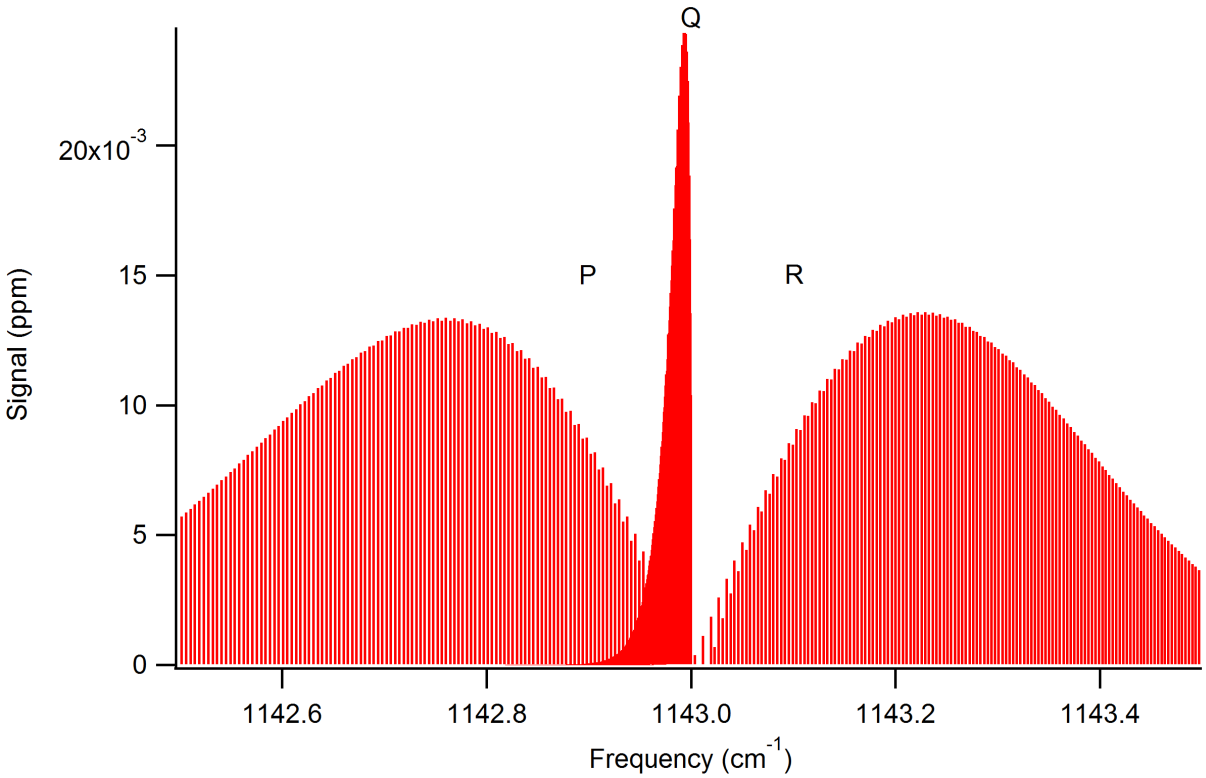

Figure A.4: Simulated stick spectrum of C_{70}. The few missing R transitions are visible, although the missing P transitions are obscured by the Q branch. This simulation assumes a ΔB of 0.1%, but does not account for Coriolis coupling. Other parameters are T_{rot} = 20K and T_{vib} = 0K.

C. Perylene

It may also be useful to consider the spectrum of the polycyclic aromatic hydrocarbon perylene. Perylene is an asymmetric top of D_{2h} symmetry. Unlike the fullerenes discussed above, perylene contains hydrogen atoms of spin ½. While spin statistics do affect the strengths of individual transitions in the usual way, there are no completely forbidden transitions as in the above molecules. The B_{3g} band at 1151 cm^{-1} has a band strength of 1.04 km/mol [9]; assuming a column density comparable to those used for the fullerene simulations, the strongest individual transition is approximately 600 times weaker than that of C_{60} (Figure 5). In practice, the column densities of C_{60} and C_{70} are limited by their solubilities; the achievable column density for perylene would be orders of magnitude greater, and it should also be considerably easier to cool vibrationally. Because of this, it is reasonable to expect that perylene would actually be easier to observe than either fullerene.

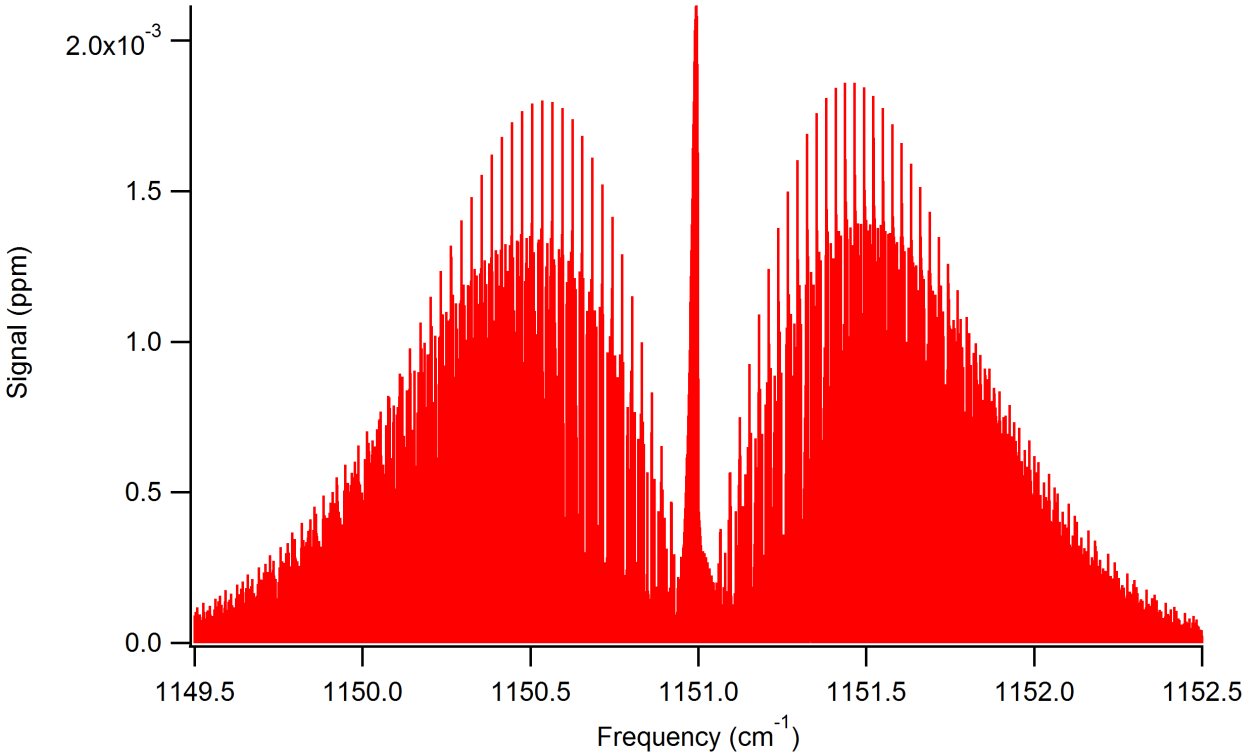

Figure A.5: Simulated stick spectrum of perylene. The spectrum has no missing levels, but the effects of spin statistics can be readily seen. The spectrum is considerably more complex than those of the fullerenes. This simulation assumes a ΔB of 0.1%, but does not account for Coriolis coupling. Other parameters are T_{rot} = 20K and T_{vib} = 0K.

References

[1] D.A. McQuarrie and J.D. Simon, Physical Chemistry: A Molecular Approach, University Science Books (1997).

[2] P.F. Bernath, Spectra of Atoms and Molecules (2nd Ed.), Oxford University Press (2005).

[3] R. Saito, G. Dresselhaus and M.S. Dresselhaus. *Phys. Rev. B* **50**, 15 (1994).

[4] B.E. Brumfield. Development of a Quantum Cascade Laser Based Spectrometer for High-Resolution Spectroscopy of Gas Phase C_{60}. UIUC, 2011.

[5] N. Sogoshi, Y. Katto, T. Wakabayashi, T. Momose, S. Tam, M.E. DeRose and M.E. Fajardo. *J. Phys. Chem. A* **104**, 3733 (2000).

[6] D.A. Dixon, B.E. Chase, G. Fitzgerald and N. Matsuzawa. *J. Phys. Chem.* **99**, 4486 (1995).

[7] S. Iglesias-Groth, F. Cataldo and A. Manchado. *Mon. Not. R. Astron. Soc.* **413**, 213 (2011).

[8] V. Schettino, M. Pagliai and G. Cardini. *J. Phys. Chem. A* **106**, 1815 (2002).

[9] D.M. Hudgins and S.A. Sandford. *J. Phys. Chem. A* **1998**, 344 (1998).

Appendix B

Inefficient Vibrational Cooling of C_{60} in a Supersonic Expansion

Hindawi Publishing Corporation
ISRN Physical Chemistry
Volume 2013, Article ID 675138, 10 pages
http://dx.doi.org/10.1155/2013/675138

Research Article

Inefficient Vibrational Cooling of C_{60} in a Supersonic Expansion

Jacob T. Stewart,[1,2] Brian E. Brumfield,[1,3] Bradley M. Gibson,[1] and Benjamin J. McCall[4]

[1] *Department of Chemistry, University of Illinois, Urbana, IL 61801, USA*
[2] *Department of Chemistry, Emory University, Atlanta, GA 30322, USA*
[3] *Department of Electrical Engineering, Princeton University, Princeton, NJ 08544, USA*
[4] *Departments of Chemistry and Astronomy, University of Illinois, Urbana, IL 61801, USA*

Correspondence should be addressed to Benjamin J. McCall; bjmccall@illinois.edu

Received 17 September 2013; Accepted 12 November 2013

Academic Editors: M. Sliwa, D. Strout, L. Vattuone, and A. Vergara

High-resolution gas-phase infrared spectroscopy of buckminsterfullerene (C_{60}) was attempted near 8.5 μm using cavity ring-down spectroscopy. Solid C_{60} was heated in a high-temperature (~950 K) oven and cooled using an argon supersonic expansion generated from a 12.7 mm × 150 μm slit. The expected *S/N* ratio is ~140 for vibrationally cold C_{60}, but no absorption signal has been observed, presumably due to a lack of vibrational cooling of C_{60} in the expansion. Measurements of D_2O at 875 K are presented as a test of instrument alignment at high temperature and show that efficient rotational cooling of D_2O occurs in the hot oven (T_{rot} = 20 K in the expansion), though vibrational cooling does not occur. The attempted C_{60} spectroscopy is compared to previous work which showed efficient vibrational cooling of polycyclic aromatic hydrocarbons (PAHs). Possible alternative experiments for observing a cold, gas-phase spectrum of C_{60} are also considered.

1. Introduction

Ever since its discovery in 1985 [1], buckminsterfullerene (C_{60}) has been the subject of an enormous body of research (the publication of its discovery has been cited more than 8100 times at the time of writing according to Web of Science). One particular area of interest is the astrochemistry of C_{60}. C_{60} was long believed to be present in the interstellar medium (ISM) and has recently been detected via emission spectroscopy in the mid-infrared (mid-IR) [2–7]. Though C_{60} has been detected in the ISM, the mechanism by which it is formed is still under debate [8]. Obtaining an astronomical absorption spectrum of C_{60} would yield additional information about the abundance and temperature of C_{60} in the ISM, which could provide useful information in determining the formation mechanism. Unfortunately, astronomical searches for absorption from cold gas-phase C_{60} are hampered by the lack of a high-resolution gas-phase laboratory spectrum of any of the four infrared active vibrational bands of C_{60}.

A rotationally resolved spectrum of C_{60} would also be of great fundamental interest. The acquisition of such a spectrum would be a significant milestone in the field of molecular spectroscopy, as C_{60} would be the largest and most symmetric molecule to be observed with rotational resolution. In addition, due to boson exchange symmetry restrictions on the overall symmetry of the molecular wave function there are many rotational levels in the ground and vibrationally excited state that are rigorously forbidden to exist [9, 10]. Such missing levels will manifest as "gaps" in the normal progression of rovibrational lines.

Despite great interest in a high-resolution spectrum of C_{60}, a rotationally resolved, gas-phase absorption spectrum of C_{60} has not yet been observed. There are several obstacles which must be overcome to record such a spectrum. First, it is difficult to generate a gas-phase sample of C_{60}. C_{60} has negligible vapor pressure at room temperature and must be heated to temperatures in excess of 875 K to reach a vapor pressure on the order of 10–100 mTorr [15]. Second, C_{60} has 174 vibrational modes, which leads to a large vibrational partition function at even modest temperatures (see Figure 1). Cooling the vibrational degrees of freedom will be critical for observing a fundamental vibrational band. Finally, it is necessary to have a sensitive, high-resolution spectrometer in the mid-IR to observe the relatively small amount of gas-phase sample.

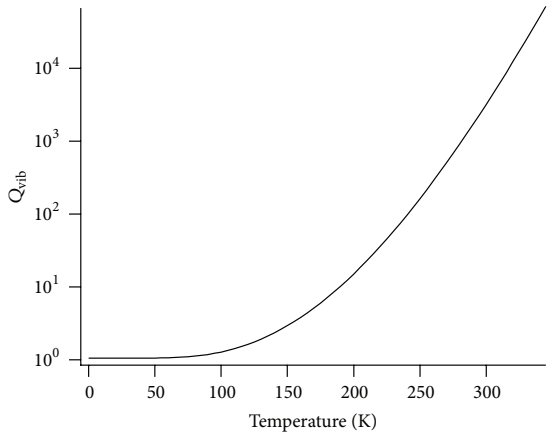

FIGURE 1: Plot of C_{60} vibrational partition function (on a logarithmic scale) versus temperature. The vibrational frequencies used in the calculation were obtained from [16].

We have developed an experiment which attempts to address these obstacles. We have built a high-temperature oven source which has been used to generate C_{60} vapor. To attempt to relax the vibrational degrees of freedom, the hot C_{60} vapor has been cooled using a supersonic expansion. The supersonic jet is then probed using continuous wave cavity ring-down spectroscopy (cw-CRDS) [18]. We have attempted to observe the 8.5 μm band due to the availability of quantum cascade laser (QCL) sources at this wavelength and also because this band coincides with an atmospheric window, permitting ground-based astronomical observations. The cavity ring-down spectrometer has already been tested by carrying out high-resolution spectroscopy of methylene bromide [19] and pyrene [13]. Despite multiple spectral searches under a variety of expansion source conditions, no absorption signals from C_{60} have yet been detected.

Previous work has shown effective vibrational cooling of large molecules, such as polycyclic aromatic hydrocarbons (PAHs), in supersonic expansions [13, 14, 20]. In contrast to this previous work, our lack of signal indicates that the vibrational degrees of freedom are not effectively cooled in C_{60}. We will discuss the details of our experiment and also briefly discuss measurements of D_2O made in the heated oven, which show good rotational cooling, but no vibrational cooling. We will also compare our current experiment to the previous work showing good vibrational cooling of other large molecules. Finally, we will present possible alternative experiments which may allow observation of a high-resolution absorption spectrum of C_{60}.

2. Materials and Methods

2.1. QCL-Based Cavity Ring-Down Spectrometer. Our high-resolution mid-IR spectrometer has been described in detail previously [18, 19], so here we present only a brief overview of the instrument. Mid-IR light near 8.5 μm is generated using a QCL supplied by collaborators in the Gmachl group at Princeton. The frequency of the emitted light can be tuned from ~1180 to 1200 cm^{-1} by changing the temperature of the laser and the current applied to the QCL. Light from the QCL is sent through an optical isolator to an optical cavity where we perform cw-CRDS to record the infrared absorption spectrum of our sample. To calibrate our spectra we utilize an absorption cell filled with SO_2 to provide absolute frequency calibration and a mid-IR wavemeter for relative frequency calibration.

2.2. Vaporization Source and Expansion Seeding. We have constructed a high-temperature oven which we used to produce gas-phase C_{60}. The oven is described in detail in our previous work on pyrene [13]. The oven is made from stainless steel with attached strip heaters to provide heating and is capable of operating under vacuum at temperatures up to 975 K for many hours. To produce gas-phase C_{60} for spectroscopy, solid C_{60} (MER Corporation, 99 + % purity) was loaded into the oven, which was then placed in a vacuum chamber and surrounded by an aluminum heat shield. The oven was heated by applying current to the strip heaters using variable transformers, which gave us coarse control over the temperature of the oven. The oven temperature was monitored using a thermocouple inserted into the interior of the oven. Once we had achieved the desired temperature (~ 950 K) a stream of Ar gas was passed through the oven and generated a continuous supersonic expansion of the Ar/C_{60} mixture through a 12.7 mm × 150 μm slit; the expansion was then probed with our spectrometer. Effective vaporization of C_{60} in the oven was verified by measuring the mass of C_{60} in the oven following a set of scans, and also by deposition of C_{60} on the walls of our vacuum chamber. The alignment between the supersonic expansion from the vaporization source and the optical cavity was verified in separate experiments through spectroscopy of D_2O. In these experiments, trace D_2O (Cambridge Isotope Laboratories, 99.9% D) was seeded into the Ar flow and was passed through the vaporization source as it was being operated at temperatures similar to those used when vaporizing solid C_{60}.

2.3. Signal-to-Noise Estimation for C_{60}. Knowledge of where to scan in frequency space to detect the first signal from the 8.5 μm vibrational band of C_{60} is critical. Restricting the search window allowed us to focus on varying experimental parameters instead of trying to cover a large spectral region. The only gas-phase measurements come from observations of infrared emission at ~1000 K [21, 22]. The estimated band center position was 1169.1 cm^{-1} [21], but this estimate is likely red-shifted due to the contribution from hot bands, whose emission frequencies are shifted due to vibrational anharmonicity. Low-temperature (15 K) measurements of C_{60} films assign the center position to 1183.7 cm^{-1} [23], while Ar matrix spectroscopy yields 1184.8 cm^{-1} [24]. Measurements in para-H_2 (p-H_2), considered the least perturbing matrix host, place the center position of the vibrational band at 1184.7 cm^{-1} [10]. Because the frequency shift between Ar and p-H_2 matrix hosts for a spectral feature is generally comparable to the frequency shift between gas-phase and p-H_2, we feel confident

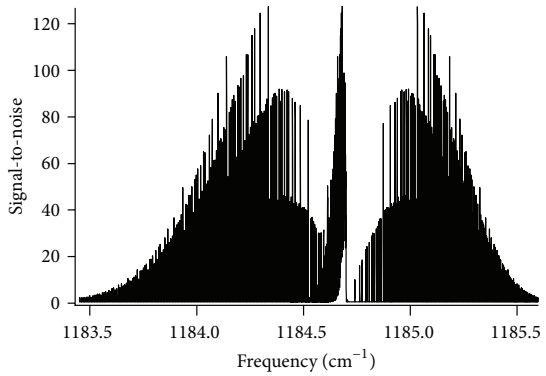

Figure 2: Plot of calculated S/N versus frequency. The S/N was calculated at T_{rot} = 20 K, T_{vib} = 0 K, B'' = 0.0028 cm^{-1}, B' = 0.002795 cm^{-1}, ζ = −0.0319, oven temperature of 955 K, and a mass loss of 2.0 g/hr, corresponding to a probed number density of $^{12}C_{60}$ in the expansion of 1.7×10^{12} cm^{-3}. The assumed noise level was 1.0 ppm and the linewidth for the transitions was set to 0.0004 cm^{-1}. The largest value of S/N for a single rovibrational transition is ~130. These parameters are similar to our experimental parameters for attempt 1 listed in Table 1. The value for ζ comes from [17].

that the peak of the 8.5 μm absorption band should be near the p-H_2 matrix value of 1184.7 cm^{-1}.

We have simulated the 8.5 μm C_{60} vibrational band at high resolution, following the approach of Sogoshi et al. [10]. As noted by Sogoshi et al., the appearance of the spectrum will be dependent on the change of the rotational constant from the ground to the excited vibrational state as well as the Coriolis coupling constant ζ. If the change in rotational constant is small, there will be a prominent Q-branch. If the change is large (on the order of 1%), there could be a prominent R-branch head. Because we do not know if either of these cases will happen in the actual experimental spectrum, we base our signal-to-noise (S/N) estimates on observing a single rovibrational transition. To estimate our expected signal, we use a theoretical value for the band strength of the 8.5 μm band [25] of 25 km/mol. Our estimates assume a vibrational temperature of 0 K. We will discuss the importance of vibrational excitation in Section 3.3.

Estimating the expected S/N for C_{60} absorption using our experimental apparatus parallels calculations that we carried out to estimate vibrational cooling of pyrene in a previous publication [13]. We begin with the following formula for estimating the S/N for a single rovibrational transition:

$$\frac{S}{N} = \frac{n_z f S' L_{jet}}{\Delta\tilde{\nu}(\sigma_{NEA})}. \quad (1)$$

In this equation, n_z is the number density of $^{12}C_{60}$ in units of cm^{-3} at a distance z from the slit, f is the ratio of the line intensity for a single transition (factoring in Boltzmann statistics) divided by the sum of all the line intensities, S' is the calculated band strength in cm/molecule, L_{jet} is the length of the expansion in cm, $\Delta\tilde{\nu}$ is the linewidth of the transition in cm^{-1}, and σ_{NEA} represents the noise equivalent fractional absorption of the spectrometer. By evaluating each of these parameters for our instrument and this band of C_{60}, we can calculate an expected S/N for our experiment.

To estimate the number density, we use the rate of mass loss from the oven per unit time, combined with the velocity of molecules in the expansion. We account for the fact that not all of the molecules in the expansion will overlap with the TEM_{00} mode of the cavity and be probed by our spectrometer and that only 51.5% of the sample is $^{12}C_{60}$. In our previous work with pyrene, we have measured that only ~20% of the molecules in the expansion overlap with the TEM_{00} mode of the ring-down cavity [13]. Because there is little expansion along the axis of the slit, we assume that L_{jet} equals the length of the slit (12.7 mm) and can find the number density of molecules probed by our spectrometer:

$$n_{probed} = \frac{0.20 \times 0.515 \times \dot{N}_{C_{60}}}{2\omega_0 \times L_{slit} \times v_{max}}, \quad (2)$$

where $\dot{N}_{C_{60}}$ is the rate of molecules lost from the oven per second, ω_0 is the beam waist of the TEM_{00} mode, L_{slit} is the length of the slit, and v_{max} is the flow velocity of molecules in the expansion (for further details on the derivation of this expression, we refer readers to the supporting information for [13]). We estimate $\dot{N}_{C_{60}}$ by measuring the amount of C_{60} before and after heating the sample and recording the length of time for which the expansion was on. ω_0 can be calculated from the radius of curvature of our ring-down mirrors, the length of the cavity, and the wavelength of light in the cavity [26]. For our setup, ω_0 is equal to 1.1 mm. v_{max} for the expansion can be found from the temperature and mass of carrier gas atoms in the expansion [27].

We can now use (1) to calculate our expected S/N for the slit expansion, using a 0.0004 cm^{-1} (12 MHz) linewidth, which we have observed in slit expansions of methylene bromide and pyrene [13, 19]. Figure 2 displays the estimated S/N for the entire vibrational band for the measured mass loss at 955 K (2 g/hr) with the slit 6 mm from the cavity axis. The largest estimated S/N for a single rovibrational transition is ~130 (for the $P(60)$, $Q(60)$, and $R(60)$ lines).

3. Results and Discussion

3.1. Search for the C_{60} Spectrum. Our attempts to observe C_{60} are summarized in Table 1. We also attempted 6 spectroscopic searches for C_{60} using a smaller oven with both a slit and pinhole expansion, which are discussed in detail in [28], but the work presented here represents our best attempts with a high calculated S/N and complete frequency coverage of where the band is expected to be. We decided to use a slit expansion because of the narrower linewidth of transitions and the greater vibrational cooling due to the larger number of collisions that occur in a slit expansion. Our attempts were performed at three different backing pressures and all three attempts covered the entire frequency region between 1184 and 1186 cm^{-1} where we expect to observe the C_{60} vibrational band. In all attempts a $S/N > 70$ was anticipated; however, we saw no evidence of absorption due to C_{60} in any of these

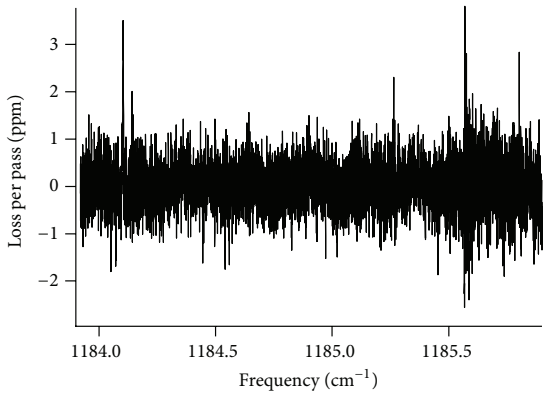

Figure 3: Representative absorption spectrum of the Ar/C_{60} expansion from 1184 to 1186 cm^{-1}. This plot is from attempt 3 listed in Table 1. Baseline drifts have been corrected by use of polynomial fitting and subtraction. Periodic fringing was removed by Fourier transforming the spectrum, eliminating the most intense frequency components, and then inverse Fourier transforming the result to retrieve the spectrum. Similar data processing was used for all attempts where periodic fringing was observed. The spikes near 1185.6 cm^{-1} are due to noise and were not reproducible. The line at 1184.1 cm^{-1} is due to absorption by water vapor in the vacuum chamber. The standard deviation of the spectrum is 0.6 ppm.

Table 1: Summary of attempted absorption spectroscopy of C_{60}. The measured mass loss rate for each attempt was used to calculate S/N. The mass loss rates were 2.0 g/hr for attempts 1 and 2 and 0.7 g/hr for attempt 3. For all attempts, the supersonic expansion was probed 6 mm downstream from the exit of the slit.

Attempt	T_0 (K)	P_0 (torr)	NEA (ppm)[a]	Estimated S/N[b]
1	955	150	1.0	130
2	955	500	0.9	140
3	965	1900	0.6	74

[a]NEA: noise equivalent absorption.

[b]These values represent the largest S/N value for a single rovibrational transition at T_{rot} = 20 K and T_{vib} = 0 K following the analysis presented in Section 2.3.

searches. An example of our spectra is presented in Figure 3, which comes from attempt 3 in Table 1.

As can be seen in Table 1, the mass loss rate for our attempts decreased from attempts 1 and 2 to attempt 3, even though all three attempts were performed at approximately the same oven temperature. The same sample was used for attempt 3 after it had been used for attempts 1 and 2, and the reduced mass loss rate for attempt 3 is indicative of sample decomposition. We also observed that after attempt 3, our sample was no longer soluble in toluene and had become conductive, even though pure C_{60} is an insulator. Further characterization by CHN analysis revealed that the recovered sample was ~89% carbon by weight, with the elemental composition of the remaining mass as yet unknown. This implies that the actual mass of C_{60} lost over the course of attempts 1, 2, and 3 was higher than reported, but without elemental analysis between attempts we cannot say when this C_{60} mass loss occurred. Because of the decomposition of our sample, the reported S/N ratios in Table 1 represent average values for the expected S/N over the course of a scan, as the mass loss rate was decreasing as we were scanning our spectrometer.

The observed reduction in the mass loss of C_{60} from the source is consistent with prior reports in the literature. In a previous study on the thermal decomposition of C_{60}, Sundar et al. observed that C_{60} held at 975 K for an extended period of time (24 h) decomposed to amorphous carbon [29]. Other publications have also observed a similar reduction in vapor pressure over time when measuring the vapor pressure of C_{60} at elevated temperatures [15, 30, 31]. This effect has been attributed to residual solvent impurities of benzene, toluene, or hexane resulting from the HPLC separation of the raw fullerene sample produced by the carbon arc method [32]. Heating the impure sample above 750 K then results in a chemical transformation of C_{60} to a different substance, such as amorphous carbon, with a reduced vapor pressure.

3.2. High Temperature Measurements of D_2O. Because of the high temperatures involved in producing gas-phase C_{60}, we were concerned that the alignment of our optical cavity with our oven might be affected by thermal expansion or other heating effects. To eliminate this possibility, we observed absorption spectra of D_2O in expansions from our oven at similar temperatures as our C_{60} searches. There are many lines of the bending mode as well as a hot band within the spectral coverage of our spectrometer, which also allowed us to monitor the rotational and vibrational temperature of D_2O molecules in the high temperature supersonic expansion.

We introduced a small amount of D_2O into an Ar slit expansion and observed low-lying states which were populated in the expansion. We observed the $1_{11} \leftarrow 0_{00}$ transition of the (010) ← (000) band of D_2O at 1199.79 cm^{-1} with the oven at 875 K to determine if alignment effects could be responsible for failure to observe C_{60}. We were easily able to observe the line in the expansion, and displacing the oven vertically only caused a slight change in the intensity of the line, consistent with the molecular distribution we measured with pyrene. This indicates that the extreme temperatures of our oven are not affecting the alignment of our ring-down cavity and preventing the observation of a C_{60} absorption signal.

Measuring several transitions of D_2O in the expansion from the hot oven permitted calculation of both the rotational and vibrational temperatures for D_2O. Table 2 presents a list of the transitions that we measured in the (010) ← (000) and (020) ← (010) vibrational bands of D_2O. Each line was measured 5 times and the average intensity for each line was used for all temperature calculations. Figure 4 shows a Boltzmann plot for both the fundamental and hot band transitions, showing that the rotational temperature of the D_2O molecules is ~20 K in both the ground and excited vibrational states. From this we see that even though the expansion originated in an oven at 875 K, the rotational degrees of freedom are cooled efficiently. On the other hand, the strength of the hot band lines is consistent with a vibrational temperature >1000 K. The hot vibrational temperature for D_2O is not surprising,

Table 2: List of observed D_2O transitions. Rotational levels are denoted in the usual way (J_{K_a,K_c}). The listed frequencies are from [11, 12].

Vibrational band	Transition	Frequency (cm^{-1})
(010) ← (000)	$1_{11} \leftarrow 0_{00}$	1199.793
	$2_{02} \leftarrow 1_{11}$	1194.038
	$2_{11} \leftarrow 2_{02}$	1193.255
	$3_{12} \leftarrow 3_{03}$	1198.536
(020) ← (010)	$1_{11} \leftarrow 0_{00}$	1181.311
	$3_{13} \leftarrow 2_{02}$	1199.154
	$2_{20} \leftarrow 2_{11}$	1192.497
	$2_{21} \leftarrow 2_{12}$	1199.690
	$4_{04} \leftarrow 3_{13}$	1198.379

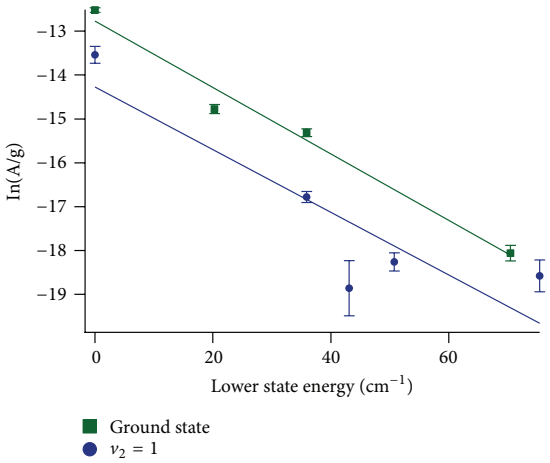

Figure 4: Boltzmann plot of D_2O rotational levels observed in the supersonic jet at 875 K. The error bars indicate 3σ deviations from the average for each data point. The calculated rotational temperatures from the linear fits are 19 ± 2 K for the ground vibrational state (green squares) and 20 ± 6 K for the $\nu_2 = 1$ vibrational state (blue circles). The uncertainties in the temperatures are 1σ values.

considering that the lowest energy vibration in the molecule lies at ~1178 cm^{-1}. Even at an oven temperature of 875 K, this is almost twice the value of k_BT (608 cm^{-1} at 875 K), and vibrational modes with energies significantly higher than k_BT do not effectively relax to the ground vibrational state in a supersonic expansion [33].

3.3. Vibrational Partition Function and Importance of Vibrational Cooling. From the material presented in Section 2.3 describing the method of calculating the experimental S/N, we can see that if the C_{60} molecules are cooled vibrationally in the supersonic expansion, we would anticipate observing an absorption signal even if there is not a strong R-branch head or Q-branch. Therefore, the most likely explanation for our lack of observed signal is that we are not achieving sufficient vibrational cooling of C_{60}. For us to observe absorption from the C_{60} molecules, they must be in the ground vibrational state. The fraction of molecules in the ground vibrational state (assuming a Boltzmann distribution) is given by the expression

$$f_0 = \frac{e^{-E_0/(k_B T_{\text{vib}})}}{Q_{\text{vib}}}, \tag{3}$$

where E_0 is the energy of the ground vibrational state, T_{vib} is the vibrational temperature, and Q_{vib} is the vibrational partition function. If we express the vibrational energies relative to $E_0 = 0$, (3) simply becomes the inverse of the partition function. Because C_{60} has 174 vibrational degrees of freedom, its vibrational partition function increases rapidly with increasing temperature (see Figure 1), meaning that very few molecules occupy the ground vibrational state at high temperatures. Even at a vibrational temperature as low as 190 K, only 1 in 10 C_{60} molecules will be in the ground vibrational state, leading to an order of magnitude decrease for an absorption signal. If we assume that the lack of vibrational cooling is the primary cause preventing us from observing C_{60}, we can calculate a lower limit for T_{vib} in the expansion using our expected S/N and (3). Our expected signal is proportional to f_0, so if our expected S/N is 140 (as in attempt 2 in Table 1), f_0 must be decreased by at least a factor of 140 for us not to observe the signal. This means that Q_{vib} must be at least 140, which would correspond to $T_{\text{vib}} \simeq 250$ K. It should be noted that this lower limit of 250 K assumes a Boltzmann distribution for the vibrational levels, which is likely not the case in a supersonic expansion.

Previous studies have shown that large molecules (specifically PAHs) can be effectively cooled in supersonic expansions [14]. Our own recent measurements of pyrene using the experimental setup described in this paper indicated that pyrene was cooled to $T_{\text{vib}} = 23$–111 K [13]. It is useful to compare these previous studies with our current attempted spectroscopy to ascertain why we were unable to observe C_{60} absorption in our expansion.

Vibrational cooling of large molecules seeded in a supersonic expansion of a monatomic carrier gas proceeds by transferring vibrational energy from the large molecule to translational energy in the expansion by collisions with the carrier gas (V-T transfer). Because of this, the number of collisions that a molecule experiences in the supersonic expansion will have a significant effect on the amount of vibrational cooling that is possible in the expansion. We have estimated the number of two-body hard sphere collisions which occur in our attempted C_{60} spectroscopy and previous work on PAHs by our group [13] and Amirav et al. [14]. The estimated number of collisions for our work and the work of Amirav et al. [14] is found in Table 3. The details of our calculations are outlined in the following paragraphs.

The first step in estimating the number of collisions in a supersonic expansion is to describe the temperature, density, and velocity of molecules in the expansion. These properties

Table 3: Estimated number of two body hard sphere collisions experienced by large molecules seeded in an argon supersonic expansion. The first three entries in the table are from the attempted C_{60} spectroscopy reported in this work. The pyrene entry is from our previous work observing pyrene in the same experimental setup which we used to attempt C_{60} spectroscopy [13]. The remaining entries are from laser induced fluorescence spectroscopy of the listed PAHs performed by Amirav et al. [14]. The listed pressures for the PAHs were sufficient to produce vibrationally cold molecules ($T_{vib} \lesssim 100$ K). The C_{60} and pyrene expansions used a 12.7 mm × 150 μm slit. For the work of Amirav et al. [14] all expansions used a 150 μm diameter pinhole. Further details on how the number of collisions was calculated can be found in the article text.

Molecule	T_0 (K)	P_0 (torr)	Nozzle type	Number of collisions
C_{60} (att. 1)	955	150	Slit	320
C_{60} (att. 2)	955	500	Slit	1100
C_{60} (att. 3)	965	1900	Slit	4000
Pyrene	430	150	Slit	560
Anthracene	410	270	Pinhole	600
Tetracene	485	175	Pinhole	360
Pentacene	550	250	Pinhole	500
Ovalene	630	300	Pinhole	620

Table 4: Hard sphere radii used to compute the mean free path of molecules in the supersonic expansion.

Species	Radius (Å)
Ar	1.88
C_{60}	5.0
Pyrene	4.0
Anthracene	3.8
Tetracene	4.2
Pentacene	4.6
Ovalene	5.1

are given by the following equations for the centerline of the expansion, which are reproduced from [34]

$$T(z) = T_0\left(1 + \frac{\gamma - 1}{2}M^2\right)^{-1},$$
$$n(z) = n_0\left(1 + \frac{\gamma - 1}{2}M^2\right)^{-1/(\gamma-1)}, \quad (4)$$
$$v(z) = M\sqrt{\frac{\gamma k_B T_0}{m}}\left(1 + \frac{\gamma - 1}{2}M^2\right)^{-1/2}.$$

In these equations, z represents the distance from the nozzle along the centerline of the expansion, T_0 and n_0 are the temperature and number density of the gas prior to the expansion, γ is the heat capacity ratio (which is 5/3 for the argon expansions we consider here), M is the Mach number of the expansion, and m is the mass of the gas. Because the large molecule is only a minor constituent of the gas being expanded, we assume that the properties of the expansion can be approximated as that of a pure argon expansion. To use these equations, we also need to know the value of M as a function of z; equations to do so for both slit and pinhole expansion sources are provided in [34].

The next step in calculating the number of collisions is to calculate the mean free path of the large molecules in the expansion. To do so, we use a hard sphere model, which gives the usual equation:

$$\lambda(z) = \frac{1}{\sqrt{2}\pi\left(r_{large} + r_{Ar}\right)^2 n(z)}, \quad (5)$$

where $\lambda(z)$ is the mean free path as a function of distance from the expansion nozzle and r_{large} and r_{Ar} are the hard sphere radii for the large molecule and argon atoms, respectively. Because C_{60} is roughly a sphere, we can simply use the van der Waals radius of C_{60} for r_{large} in this equation, but the PAHs studied by us and Amirav et al. are far from spherical. To get a rough approximation of a hard sphere radius for these species, we used values for the minimum and maximum projected cross-sections of the molecules as given in the chemicalize.org database from ChemAxon [35]. To obtain a hard sphere radius, we averaged the minimum and maximum projected cross-sections for the PAHs and then calculated an effective radius based on the average cross section of the molecule. While this is certainly not exact, it should give a rough estimate of the relative size of the PAHs for computing the mean free path and seems to give reasonable results. The hard sphere radii which we used to compute the mean free path are listed in Table 4.

We can then calculate the average frequency of two-body collisions of the large molecule with Ar atoms in the expansion by dividing the average speed of the molecules by the mean free path. We assume that the translational temperature of the large molecules is thermalized with the translational temperature of the Ar atoms and calculate the average speed according to

$$s(z) = \sqrt{\frac{8k_B T(z)}{\pi\mu}}, \quad (6)$$

where μ is the reduced mass of the Ar and large molecule. Using the above equations, we can calculate the collision frequency at any point z along the centerline of the expansion. We calculated the collision frequency in steps of 1.5 μm from $z = 0$ to 6 mm along the expansion for all of the molecules and conditions listed in Table 3. We then calculated the number of collisions at each point by calculating the velocity of the expansion to determine how long the molecules were within each 1.5 μm section and then multiplying that time by the collision frequency. We then added together the number of collisions calculated for each of these 1.5 μm sections from $z = 0$ to 6 mm to give the total number collisions listed in Table 3. We use a maximum of 6 mm because that is where the expansion was probed in our work and in the work of Amirav et al. [14].

From Table 3, we can see that the PAHs were vibrationally cooled after undergoing an average of 360–620 collisions with Ar. In our attempted C_{60} spectroscopy, the C_{60} molecules underwent an average of 320, 1100, and 4000 collisions with

Table 5: Vibrational partition function, average vibrational energy (above zero-point energy) in cm^{-1}, frequency of the lowest energy vibrational mode, and energy to collision ratio for the molecules listed in Table 2 at the temperatures listed in that table. The calculated values for our D_2O measurements from Section 3.2 are also included for comparison.

Molecule	Q_{vib}	E_{vib} (cm^{-1})	ν_{min} (cm^{-1})	E_{vib} /collisions
C_{60} (att. 1)	1.3×10^{28}	56000	267	174
C_{60} (att. 2)	1.3×10^{28}	56000	267	50
C_{60} (att. 3)	3.0×10^{28}	57000	267	14
Pyrene	4.0×10^{3}	4000	99	7
Anthracene	1.5×10^{3}	3200	91	5
Tetracene	1.0×10^{6}	6400	56	18
Pentacene	2.5×10^{9}	10000	38	21
Ovalene	8.6×10^{13}	18000	61	29
D_2O	1.20	260	1178	0.8

Ar for attempts 1, 2, and 3 in Table 1, respectively. For attempts 1 and 2, the number of collisions is similar to the number of collisions for the PAH molecules, while the much higher backing pressure for attempt 3 increased the number of collisions by an order of magnitude compared to attempt 1. While the C_{60} molecules underwent a similar number of collisions as the PAHs, or significantly more for attempt 3, we have seen that this was insufficient to produce vibrationally cold C_{60}, which would have been observable with our spectrometer. To try to understand why this might be the case, we can compare the vibrational properties of these molecules.

Theoretical harmonic vibrational frequencies for all of the PAHs listed in Table 3 can be found in the PAH IR Spectral Database [36], which come from the original data of Langhoff [37]. We have used these vibrational frequencies to calculate the vibrational partition functions of the PAHs and C_{60} at high temperature before being cooled by supersonic expansion. Using the vibrational partition function, we can also calculate the amount of vibrational energy in an average molecule at high temperature. These values are presented in Table 5 for all of the molecules we have been considering. The first thing to notice is the incredibly large partition functions for these molecules at elevated temperatures, especially for C_{60} and ovalene. According to (3), this means that on average only 1 in 10^{28} molecules of C_{60} is in the ground vibrational state before the expansion. Table 5 also shows that these molecules have a large amount of vibrational energy (over 50000 cm^{-1} for C_{60}) that must be transferred into the supersonic expansion to cool them vibrationally. For the PAHs, we have seen that it is possible to transfer this energy in the hundreds of collisions that occur in the expansion. We can divide the vibrational energies in Table 5 by the collision numbers in Table 3 to calculate an energy to collision ratio to get an idea of how much energy would need to be removed in an average collision to cool the molecule. This ratio is listed in the last column of Table 5. For the vibrationally cold PAH molecules, an average collision carried away 5–30 cm^{-1} of energy. For our attempted C_{60} spectroscopy, the energy to collision ratio is significantly higher than this for attempt 1, slightly higher for attempt 2, and right in the range of the PAHs for attempt 3.

Looking at these values, it is somewhat surprising that C_{60} was not efficiently cooled using a supersonic expansion for attempts 2 and 3. Considering the previous work with PAHs, it appears that there should be enough collisions to carry away the vibrational energy for these attempts. One possible reason why C_{60} was not efficiently cooled is that the lowest energy vibrational mode for C_{60} is at 267 cm^{-1}, which is significantly higher than the lowest modes for the PAHs (see Table 5). To completely cool the molecule to the ground vibrational state, energy must be transferred from the lowest vibrational mode into translational energy. The efficiency of V-T transfer decreases as the energy gap increases, making it more difficult for modes with higher energy to be completely cooled. As an extreme example of this, we can consider the D_2O spectroscopy presented in Section 3.2. We have calculated the vibrational properties for D_2O following the same procedure as for C_{60} and the PAHs, using vibrational frequencies from [38]. The results are listed in Table 5 and show that the amount of vibrational energy for a small molecule at high temperature is much lower than the large molecules we have been considering. At a temperature of 875 K and a backing pressure of ~300 torr, the average number of hard sphere collisions for a D_2O molecule in the expansion is 310 (using a hard sphere radius of 1.6 Å), which gives an energy to collision ratio of 0.8. Even though this ratio is significantly lower than for all of the PAHs, we observed substantial population in the (010) state, indicating no cooling of this vibrational mode. This lack of cooling is a direct consequence of the fact that the lowest energy mode lies so high in energy.

Another possibility is that the extremely large size of C_{60} is causing a significant velocity slip effect to occur because of the large difference in mass between the C_{60} molecules and the Ar carrier gas [14]. While this does not seem to be a problem for the previous work on ovalene, C_{60} is about 2 times heavier than ovalene. This problem would be easily remedied by using a heavier carrier gas such as Kr or Xe, which would more closely match the mass of C_{60}. We did not try a heavier gas because of the increased cost of these gases compared to Ar, especially when used continuously, as in our experiment. For future attempts to observe C_{60}, it may be worth the extra expense to try the heavier rare gases to reduce the velocity slip effect.

Finally, it is worth noting that other molecules have been observed to have anomalously low cooling efficiency in supersonic expansions. In particular, Sulkes observed that benzene

displays a lack of collision-induced vibrational relaxation in He and Ar expansions, despite the fact that substituted benzene derivatives showed excellent cooling under similar conditions [39]. Sulkes attributed this to a lack of efficient cooling via orbiting resonances; it is conceivable that a similar effect is occurring with C_{60}.

3.4. Alternative Methods for Producing Gas-Phase C_{60}. It would be preferable to produce C_{60} vapor at a much lower temperature than is possible in our oven. Doing so would significantly decrease the vibrational partition function and vibrational energy of the molecules prior to the supersonic expansion. For example, if C_{60} vapor could be produced at a temperature similar to our pyrene work (430 K), then the vibrational partition function would be only 5×10^7 and an average molecule would only have 11000 cm^{-1} of vibrational energy, which would be quite similar to the PAHs that were observed by Amirav et al. This should make it much easier to cool the C_{60} molecules to the ground vibrational state.

We are aware of three possible methods for producing C_{60} vapor at lower temperatures: supercritical fluid expansion, laser desorption, and collisional cooling in the gas-phase. In the supercritical fluid expansion method the C_{60} sample would be dissolved in a supercritical fluid. It has been demonstrated that C_{60} can be dissolved in supercritical toluene, or to a lesser extent in supercritical carbon dioxide containing toluene as a co-solvent [40, 41]. Assuming a 1 : 1 volume ratio of CO_2 to toluene, the critical temperature is ~450 K. Decreasing the toluene content will lower the critical temperature, though this would be at the expense of solubility. It will be necessary to optimize the toluene content for our particular needs. We would likely employ an argon sheath-flow continuous expansion source, as in [42].

A laser desorption/supersonic expansion source has been successfully employed for resonant two-photon ionization measurements of C_{60} [43, 44], but the vibrational temperature of the vapor produced was not directly observed. Likewise, while it has been shown that laser desorption can volatilize large molecules with pre-expansion vibrational temperatures below what one would expect for thermal vaporization [45, 46], the temperatures achievable are molecule- and surface-dependent and as yet unknown for C_{60}. As such, the viability of a laser desorption source is difficult to assess without further experiments.

The final method to discuss for producing cold gas-phase C_{60} relies upon the modified use of a gas-phase aggregation cluster source [47] to collisionally cool isolated C_{60} molecules. In an aggregation source the hot vapor from the heated sample is entrained in a flow of noble gas that is cooled by collisions with the walls inside the source that are kept at 77 K using liquid nitrogen cooling [48, 49]. A collimated molecular beam of cold sample clusters is produced by passing the flow out of the source through a nozzle. While normally such sources are used to efficiently produce large clusters of molecules or atoms, it has been shown that cold isolated C_{60} molecules can be produced by keeping the gas-phase number density of C_{60} low through reduction of the temperature of the sample oven [47]. By operating the aggregation source in this way it was possible to collect two-photon resonant ionization spectra of C_{60} with an estimated vibrational temperature <80 K [47].

Although we expect all of the proposed methods to be superior to our current oven in terms of vibrational temperature, we also expect them to produce significantly lower number densities of gas-phase C_{60}. Based on reports of supercritical fluid extractions of C_{60} [40, 41], we anticipate that the number density produced by a supercritical fluid expansion would be two orders of magnitude lower than that of our current oven. Studies where laser desorption [43, 44] or collisional cooling [47] was used do not report gas-phase C_{60} number densities; however, the C_{60} number densities generated using these methods will be considerably lower than the number density produced using a supercritical fluid. Assuming that C_{60} can be efficiently cooled in a supercritical fluid expansion, we will need to implement high repetition rate CRDS [50] to account for the low C_{60} number density. Depending on the repetition rate achieved, doing so would improve S/N by a factor of 10–20. If C_{60} does not cool completely or the number density is lower than anticipated, noise-immune cavity-enhanced optical heterodyne molecular spectroscopy (NICE-OHMS) detection could be implemented instead, improving our signal-to-noise ratio by as much as three orders of magnitude [51]. This route would also significantly increase the technical complexity of our spectrometer.

4. Conclusions

Obtaining a high-resolution gas-phase spectrum of C_{60} represents a significant challenge for molecular spectroscopy. We have attempted to obtain such a spectrum using a highly sensitive cw-CRDS spectrometer but were unable to detect any absorption signal from C_{60}. We have shown that an absorption signal should be expected with our current experimental setup if we are able to vibrationally cool C_{60}. Our lack of signal is most likely due to the fact that we must heat our sample to >950 K to obtain sufficient vapor pressure for spectroscopy, which leads to an incredibly large vibrational partition function because of the large size of C_{60}. We have compared these results with previous work that has shown efficient vibrational cooling of large polycyclic aromatic hydrocarbons. To overcome this problem it will be necessary to produce gas-phase C_{60} at much lower temperatures so that the vibrational degrees of freedom can be cooled. While there may exist alternative methods that are capable of generating a cold gas-phase sample, these methods will result in low number densities of C_{60}. The low C_{60} number density will require the use of more sensitive and complex absorption spectroscopy techniques than cw-CRDS to enable collection of a rotationally resolved spectrum.

Conflict of Interests

The authors have no direct financial relations with the commercial identities named in this work.

Acknowledgments

The authors would like to thank the Gmachl group at Princeton for providing the quantum cascade lasers which have made this work possible. The authors also thank Gregory S. Girolami for useful discussions about decomposition of the C_{60} sample. Their efforts to observe the spectrum of C_{60} have been supported by the NASA Laboratory Astrophysics Program (APRA NNG05GE59G), a Camille and Henry Dreyfus New Faculty award, a Packard Foundation Fellowship, and the University of Illinois. Jacob T. Stewart has been supported by a Robert C. and Carolyn J. Springborn Fellowship from the University of Illinois.

References

[1] H. W. Kroto, J. R. Heath, S. C. O'Brien, R. F. Curl, and R. E. Smalley, "C_{60}: buckminsterfullerene," *Nature*, vol. 318, no. 6042, pp. 162–163, 1985.

[2] J. Cami, J. Bernard-Salas, E. Peeters, and S. E. Malek, "Detection of C_{60} and C_{70} in a young planetary nebula," *Science*, vol. 329, no. 5996, pp. 1180–1182, 2010.

[3] K. Sellgren, M. W. Werner, J. G. Ingalls, J. D. T. Smith, T. M. Carleton, and C. Joblin, "C_{60} in reflection nebulae," *The Astrophysical Journal Letters*, vol. 722, no. 1, pp. L54–L57, 2010.

[4] D. A. García-Hernández, A. Manchado, P. García-Lario et al., "Formation of fullerenes in H-containing planetary nebulae," *The Astrophysical Journal Letters*, vol. 724, no. 1, pp. L39–L43, 2010.

[5] D. A. García-Hernández, N. K. Rao, and D. L. Lambert, "Are C_{60} molecules detectable in circumstellar shells of R Coronae Borealis stars?" *The Astrophysical Journal*, vol. 729, no. 2, p. 126, 2011.

[6] D. A. García-Hernndez, S. Iglesias-Groth, J. A. Acosta-Pulido et al., "The formation of fullerenes: clues from new C_{60}, C_{70}, and (Possible) planar C_{24} detections in Magellanic cloud planetary nebulae," *The Astrophysical Journal Letters*, vol. 737, no. 2, article L30, 2011.

[7] O. Berné and A. G. G. M. Tielens, "Formation of buckminsterfullerene (C_{60}) in interstellar space," *Proceedings of the National Academy of Sciences of the United States of America*, vol. 109, no. 2, pp. 401–406, 2012.

[8] J. Bernard-Salas, J. Cami, E. Peeters, A. P. Jones, E. R. Micelotta, and M. A. T. Groenewegen, "On the excitation and formation of circumstellar fullerenes," *The Astrophysical Journal*, vol. 757, no. 1, p. 41, 2012.

[9] R. Saito, G. Dresselhaus, and M. S. Dresselhaus, "Hindered rotation of solid $^{12}C_{60}$ and $^{13}C_{60}$," *Physical Review B*, vol. 50, no. 8, pp. 5680–5688, 1994.

[10] N. Sogoshi, Y. Kato, T. Wakabayashi et al., "High-resolution infrared absorption spectroscopy of C_{60} molecules and clusters in parahydrogen solids," *Journal of Physical Chemistry A*, vol. 104, no. 16, pp. 3733–3742, 2000.

[11] C. Camy-Peyret, J.-M. Flaud, A. Mahmoudi, G. Guelachvili, and J. W. C. Johns, "Line positions and intensities in the ν_2 band of D_2O improvied pumped D_2O laser frequencies," *International Journal of Infrared and Millimeter Waves*, vol. 6, no. 3, pp. 199–233, 1985.

[12] R. A. Toth, "HDO and D_2O low pressure, long path spectra in the 600–3100 cm^{-1} region II. D_2O line positions and strengths," *Journal of Molecular Spectroscopy*, vol. 195, no. 1, pp. 98–122, 1999.

[13] B. E. Brumfield, J. T. Stewart, and B. J. McCall, "Extending the limits of rotationally resolved absorption spectroscopy: pyrene," *Journal of Physical Chemistry Letters*, vol. 3, pp. 1985–1988, 2012.

[14] A. Amirav, U. Even, and J. Jortner, "Cooling of large and heavy molecules in seeded supersonic beams," *Chemical Physics*, vol. 51, pp. 31–42, 1980.

[15] V. Piacente, G. Gigli, P. Scardala, A. Giustini, and D. Ferro, "Vapor pressure of C_{60} buckminsterfullerene," *The Journal of Physical Chemistry*, vol. 99, no. 38, pp. 14052–14057, 1995.

[16] J. Menendez and J. B. Page, *Light Scattering in Solids VIII: Fullerenes, Semiconductor Surfaces, Coherent Phonons*, Springer, Berlin, Germany, 2000.

[17] D. E. Weeks and W. G. Harter, "Rotation-vibration scalar coupling χ coefficients and spectroscopic band shapes of buckminsterfullerene," *Chemical Physics Letters*, vol. 176, no. 2, pp. 209–216, 1991.

[18] B. E. Brumfield, J. T. Stewart, S. L. Widicus Weaver et al., "A quantum cascade laser cw cavity ringdown spectrometer coupled to a supersonic expansion source," *Review of Scientific Instruments*, vol. 81, no. 6, Article ID 063102, 2010.

[19] B. E. Brumfield, J. T. Stewart, and B. J. McCall, "High-resolution spectroscopy of the ν_8 band of methylene bromide using a quantum cascade laser," *Journal of Molecular Spectroscopy*, vol. 266, no. 1, pp. 57–62, 2011.

[20] A. Amirav, U. Even, and J. Jortner, "Absorption spectroscopy of ultracold large molecules in planar supersonic expansions," *Chemical Physics Letters*, vol. 83, no. 1, pp. 1–4, 1981.

[21] C. I. Frum, R. Engleman Jr., H. G. Hedderich, P. F. Bernath, L. D. Lamb, and D. R. Huffman, "The infrared emission spectrum of gas-phase C_{60} (buckmisterfullerene)," *Chemical Physics Letters*, vol. 176, no. 6, pp. 504–508, 1991.

[22] L. Nemes, R. S. Ram, P. F. Bernath et al., "Gas-phase infrared emission spectra of C_{60} and C_{70}. Temperature-dependent studies," *Chemical Physics Letters*, vol. 218, no. 4, pp. 295–303, 1994.

[23] B. Chase, N. Herron, and E. Holler, "Vibrational spectroscopy of C_{60} and C_{70} temperature-dependent studies," *The Journal of Physical Chemistry*, vol. 96, no. 11, pp. 4262–4266, 1992.

[24] R. E. Haufler, J. Conceicao, L. P. F. Chibante et al., "Efficient production of C_{60} (buckminsterfullerene), $C_{60}H_{36}$, and the solvated buckide ion," *The Journal of Physical Chemistry*, vol. 94, no. 24, pp. 8634–8636, 1990.

[25] D. A. Dixon, B. E. Chase, G. Fitzgerald, and N. Matsuzawa, "Prediction of the fundamental vibrational frequencies for C_{60} by local density functional theory," *The Journal of Physical Chemistry*, vol. 99, no. 13, pp. 4486–4489, 1995.

[26] K. Busch and M. Busch, Eds., *Cavity-Ringdown Spectroscopy: An Ultratrace Absorption Measurement Technique*, American Chemical Society, Washington, DC, USA, 1999.

[27] O. F. Hagena, "Nucleation and growth of clusters in expanding nozzle flows," *Surface Science*, vol. 106, no. 1–3, pp. 101–116, 1981.

[28] B. E. Brumfield, *Development of a quantum cascade laser based spectrometer for high-resolution spectroscopy of gas phase C_{60} [Ph.D. thesis]*, University of Illinois at Urbana-Champaign, 2011.

[29] C. S. Sundar, A. Bharathi, Y. Hariharan, J. Janaki, V. Sankara Sastry, and T. S. Radhakrishnan, "Thermal decomposition of C_{60}," *Solid State Communications*, vol. 84, no. 8, pp. 823–826, 1992.

[30] A. Popović, G. Dražič, and J. Marsel, "Mass spectrometric investigations of fullerenes. I. vapour pressure over the C_{60}/C_{70} binary system," *Rapid Communications in Mass Spectrometry*, vol. 8, no. 12, pp. 985–990, 1994.

[31] E. Schönherr, K. Matsumoto, and M. Freiberg, "On the evaporation of C_{60} in vacuum and inert gases at temperatures between 830 K and 1050 K," *Fullerene Science and Technology*, vol. 7, no. 3, pp. 455–466, 1999.

[32] P. F. Coheur, M. Carleer, and R. Colin, "The absorption cross sections of C_{60} and C_{70} in the visible-UV region," *Journal of Physics B*, vol. 29, no. 21, pp. 4987–4995, 1996.

[33] M. E. Sanz, M. C. McCarthy, and P. Thaddeus, "Vibrational excitation and relaxation of five polyatomic molecules in an electrical discharge," *Journal of Chemical Physics*, vol. 122, no. 19, Article ID 194319, 2005.

[34] D. R. Miller, *Atomic and Molecular Beam Methods*, vol. 1, Oxford University Press, New York, NY, USA, 1988.

[35] "Chemicalize.org was used for geometry prediction of pyrene, anthracene, tetracene, pentacene, ovalene, and D_2O," April 2013, http://www.chemaxon.com/.

[36] C. W. Bauschlicher Jr., C. Boersma, A. Ricca et al., "The NASA Ames polycyclic aromatic hydrocarbon infrared spectroscopic database: the computed spectra," *The Astrophysical Journal Supplement Series*, vol. 189, no. 2, pp. 341–351, 2010.

[37] S. R. Langhoff, "Theoretical infrared spectra for polycyclic aromatic hydrocarbon neutrals, cations, and anions," *The Journal of Physical Chemistry*, vol. 100, no. 8, pp. 2819–2841, 1996.

[38] T. Shimanouchi, *Tables of Molecular Vibrational Frequencies Consolidated*, vol. 1 of *National Bureau of Standards*, Washington, DC, USA, 1972.

[39] M. Sulkes, "Anomalously small jet-cooling of benzene: absence of efficient low-energy collision-induced vibrational relaxation," *Chemical Physics Letters*, vol. 119, no. 5, pp. 426–430, 1985.

[40] K. Jinno and C. Kohrikawa, "Supercritical and subcritical fluid extraction of fullerenes from carbon soot," *Chimica Oggi*, vol. 16, no. 1-2, pp. 9–15, 1998.

[41] S. Saim, K. C. Kuo, and D. L. Stalling, "Supercritical fluid extraction of fullerenes C_{60} and C_{70} from carbon soot," *Separation Science and Technology*, vol. 28, no. 8, pp. 1509–1525, 1993.

[42] C. H. Sin, M. R. Linford, and S. R. Goates, "Supercritical fluid/supersonic jet spectroscopy with a sheath-flow nozzle," *Analytical Chemistry*, vol. 64, no. 2, pp. 233–238, 1992.

[43] R. E. Haufler, Y. Chai, L. P. F. Chibante et al., "Cold molecular beam electronic spectrum of C_{60} and C_{70}," *The Journal of Chemical Physics*, vol. 95, no. 3, pp. 2197–2199, 1991.

[44] R. E. Haufler, L.-S. Wang, L. P. F. Chibante et al., "Fullerene triplet state production and decay: R2PI probes of C_{60} and C_{70} in a supersonic beam," *Chemical Physics Letters*, vol. 179, no. 5-6, pp. 449–454, 1991.

[45] P. Voumard and R. Zenobi, "Laser-induced thermal desorption of aniline from silica surfaces," *The Journal of Chemical Physics*, vol. 103, no. 15, pp. 6795–6805, 1995.

[46] J.-Y. Zhang, D. S. Nagra, and L. Li, "Molecular cooling and supersonic jet formation in laser desorption," *Analytical Chemistry*, vol. 65, no. 20, pp. 2812–2818, 1993.

[47] K. Hansen, R. Müller, P. Brockhaus, E. E. B. Campbell, and I. V. Hertel, "Resonant two-photon ionisation spectroscopy of C_{60}," *Zeitschrift fur Physik D*, vol. 42, no. 3, pp. 153–155, 1997.

[48] U. Zimmermann, N. Malinowski, U. Näher, S. Frank, and T. P. Martin, "Producing and detecting very large clusters," *Zeitschrift für Physik D*, vol. 31, no. 1, pp. 85–93, 1994.

[49] C. Ellert, M. Schmidt, C. Schmitt, T. Reiners, and H. Haberland, "Temperature dependence of the optical response of small, open shell sodium clusters," *Physical Review Letters*, vol. 75, no. 9, pp. 1731–1734, 1995.

[50] R. Z. Martínez, M. Metsälä, O. Vaittinen, T. Lantta, and L. Halonen, "Laser-locked, high-repetition-rate cavity ringdown spectrometer," *Journal of the Optical Society of America B*, vol. 23, no. 4, pp. 727–740, 2006.

[51] M. S. Taubman, T. L. Myers, B. D. Cannon, and R. M. Williams, "Stabilization, injection and control of quantum cascade lasers, and their application to chemical sensing in the infrared," *Spectrochimica Acta A*, vol. 60, no. 14, pp. 3457–3468, 2004.

References

[1] H. W. Kroto, J. R. Heath, S. C. O'Brien, R. F. Curl, and R. E. Smalley, Nature **318**, 162 (1985)

[2] W. Kratschmer, L. D. Lamb, K. Fostiropoulos, and D. R. Huffman, Nature **347**, 354 (1990)

[3] P. Wurz and K. R. Lykke, J. Phys. Chem. **96** 10129 (1992)

[4] W. Kratschmer, K. Fostiropoulos, and D. R. Huffman, Chem. Phys. Lett. **170**, 167 (1990)

[5] J. Cami, J. Bernard-Salas, E. Peeters, and S. E. Malek, Science **329**, 1180 (2010)

[6] D. A. García-Hernández, A. Manchado, P. García-Lario, L. Stanghellini, E. Villaver, R. A. Shaw, R. Szczerba, and J. V. Perea-Calderón, Astrophys. J. Lett. **724**, L39 (2010)

[7] K. Sellgren, M. W. Werner, J. G. Ingalls, J. D. T. Smith, T. M. Carleton, and C. Joblin, Astrophys. J. Lett. **722**, L54 (2010)

[8] G. H. Herbig, Annu. Rev. Astro. Astrophys. **33**, 19 (1995)

[9] A. Leger, L. D'Hendecourt, L. Verstraete, and W. Schmidt, Astron. Astrophys. **203**, 145 (1988)

[10] E. K. Campbell, M. Holz, D. Gerlich, and J. P. Maier, Nature **523**, 922 (2015)

[11] B. E. Brumfield, J. T. Stewart, and B. J. McCall, J. Mol. Spectrosc. **266**, 57 (2011)

[12] B. E. Brumfield, J. T. Stewart, and B. J. McCall, J. Phys. Chem. Lett. **3**, 1985 (2012)

[13] J. T. Stewart, B. E. Brumfield, B. M. Gibson, and B. J. McCall, ISRN Phys. Chem. **2013**, 675138 (2013)

[14] R. E. Haufler, Y. Chai, L. P. F. Chibante, M. R. Fraelich, R. B. Weisman, R. F. Curl, and R. E. Smalley, J. Chem. Phys **95**, 2197 (1991)

[15] R. E. Haufler, L.-S. Wang, L. P. F. Chibante, C. Jin, J. Conceicao, Y. Chai, R. E. Smalley, Chem. Phys. Lett. **179**, 449 (1991)

[16] K. Hansen, R. Müller, P. Brockhaus, E. E. B. Campbell, and I. V. Hertel, Zeit. Phys. D, **42**, 153 (1997)

[17] C. H. Sin, M. R. Linford, and S. R. Goates, Anal. Chem. **64**, 233 (1992)

[18] K. Jinno and C. Kohrikawa, Chim. Oggi **16**, 9 (1998)

[19] S. Saim, K. C. Kuo, and D. L. Stalling, Sep. Sci. Tech. **28** 1509 (1993)

[20] H. Cottin, M-C. Gazeau, J-F. Doussin, F. Raulin, J. Photochem. Photobiol., A **135**, 53 (2000).

[21] H. Cottin, Y Bénilan, M-C. Gazeau, F. Raulin, Icarus **167**, 397 (2004).

[22] F. Goesmann, H. Rosenbauer, J. H. Bredehöft, M. Cabane, P. Ehrenfreund, T. Gautier, C. Giri, H. Krüger, L. Le Roy, A. J. MacDermott, S. McKenna-Lawlor, U. J. Meierhenrich, G. M. Muñoz Caro, F. Raulin, R. Roll, A. Steele, H. Steininger, R. Sternberg, C. Szopa, W. Thiemann, and S. Ulamc, Science **349**, aab0689 (2015)

[23] T. Oka, K. Tsuchiya, S. Iwata, Y. Morino, Bull. Chem. Soc. Jpn. **37**, 4 (1964).

[24] J. Bellet, J-M. Colmont, J. Lemaire, J. Mol. Spec. **34** 190 (1970).

[25] J-M. Colmont, J. Mol. Spec. **58** 220 (1975).

[26] J-M. Colmont, J. Mol. Struct. **62** 85 (1980).

[27] J-M. Colmont, J. Mol. Spec. **80** 166 (1980).

[28] J. Gadhi, G. Wlodarczak, D. Boucher, J. Demaison, J. Mol. Spec. **133**, 406 (1989).

[29] J-F. Henninot, H. Bolvin, J. Demaison, B. Lemoine, J. Mol. Spec. **152**, 62 (1992).

[30] B. Brumfield. Development of a quantum cascade laser based spectrometer for high-resolution spectroscopy of gas phase C_{60}. University of Illinois, 2011.

[31] B. M. Gibson, N. C. Koeppen, and B. J. McCall, J. Mol. Spectrosc. **317**, 47 (2015)

[32] M. Hercher, Appl. Opt. **8**, 1103 (1969).

[33] W. Demtröder, *Laser Spectroscopy* (Springer, 2008).

[34] R. L. Barger, M. S. Sorem, and J. L. Hall, Appl. Phys. Lett. **22**, 573 (1973).

[35] E. Hansis, T. Cubel, J.-H. Choi, J. R. Guest, and G. Raithel, Rev. Sci. Instrum. **76**, 033105 (2005)

[36] K. H. Ang, G. Chong, and Y. Li, IEEE Trans. Control Syst. Technol. **13**, 559 (2005).

[37] G. Wysocki, R. Lewicki, R. F. Curl, F. K. Tittel, L. Diehl, F. Capasso, M. Troccoli, G. Hofler, D. Bour, S. Corzine, R. Maulini, M. Giovannini, and J. Faist, Appl. Phys. B **92**, 305 (2008).

[38] C. M. Western, "PGOPHER, a program for simulating rotational structure," `http://pgopher.chm.bris.ac.uk`, accessed 4/1/15.

[39] B. E. Brumfield, J. T. Stewart, S. L. Widicus Weaver, M. D. Escarra, S. S. Howard, C. F. Gmachl, B. J. McCall, Rev. Sci. Instrum. **81**, 063102 (2010).

[40] B. E. Brumfield, J. T. Stewart, B. J. McCall, J. Mol. Spec. **266**, 57 (2011).

[41] B. M. Gibson, B. J. McCall, Opt. Lett. **40**, 2696 (2015).

[42] L. S. Rothman, I. E. Gordon, A. Barbe, D. Chris Benner, P. F. Bernath, M. Birk, V. Boudon, L. R. Brown, A. Campargue, J-P. Champion, K. Chance, L. H. Coudert, V. Dana, V. M. Devi, S. Fally, J-M. Flaud, R. R. Gamache, A. Goldman, D. Jacquemart, I. Kleiner, N. Lacome, W. J. Lafferty, J-Y. Mandin, S. T. Massie, S. N. Mikhailenko, C. E. Miller, N. Moazzen-Ahmadi, O. V. Naumenko, A. V. Nikitin, J. Orphal, V. I. Perevalov, A. Perrin, A. Predoi-Cross, C. P. Rinsland, M. Rotger, M. Šimečková, M. A. H. Smith, K. Sung, S. A. Tashkun, J. Tennyson, R. A. Toth, A. C. Vandaele, J. Vander Auwera, J. Quant. Spectrosc. Radiat. Transfer **110**, 533 (2009).

[43] M. Motamedi, N. Khademi, E Journal Chemistry **6(S1)**, S259 (2009).

[44] J. Ye, L. Ma, and J. Hall, Opt. Soc. Am. B **15**, 6 (1998)

[45] R. Z. Martínez, M. Metsälä, O. Vaittinen, T. Lantta, and L. Halonen, Opt. Soc. Am. B **23**, 727 (2006)

[46] R. W. P. Drever, J. L. Hall, F. V. Kowalski, J. Hough, G. M. Ford, A. J. Munley, and H. Ward, Appl. Phys. B **31**, 97 (1983)

[47] M. S. Taubman, T. L. Myers, B. D. Cannon, R. M. Williams, Spectrochim Acta A Mol. Biomol. Spectrosc. **60**, 3457 (2004)

[48] E. Hirschmann and T. E. Walsh, "Development of a 10.6-micron laser modulator." NASA Technical Note TN D-4049

[49] A. Hangauer, G. Spinner, M. Nikodem, and G. Wysocki, Opt. Express **22**, 23439 (2014)

[50] B. M. Hoeling, A. D. Fernandez, R. C. Haskell, and D. C. Petersen, Rev. Sci. Instrum **72**, 1630 (2001)

[51] H. L. Chao and T. E. Parker, "Tensile fracture strength of ST cut quartz." Raytheon Research Division, M-3938A